UNIVERSITÀ
degli STUDI
di CATANIA

Dipartimento
di Fisica
e Astronomia
"Ettore Majorana"

PhD programme in physics

Mahsa Farasat

Development of new approach for real-time activity quantification of radiopharmaceutical

PhD thesis

Supervisors:
Prof. G.A.P. Cirrone
Prof. D. Mostacci

Co-Supervisors:
Dr. L. Pompignoli
Prof. U. W Scherer

---

academic year 2022/2023

Contents

Introduction

Nuclear medicine is a specialized branch of medicine that focuses on diagnosing and treating diseases in the fields of oncology, cardiology, and neurology. It involves administering a compound labeled with a gamma-ray-emitting or positron-emitting radionuclide into the body to obtain diagnostic images. These radionuclides are also used for therapeutic purposes.

Two common nuclear medicine imaging modalities are Positron Emission Tomography (PET) and Single Photon Emission Computed Tomography (SPECT), which involve injecting a radio tracer into the patient to radiodetect specific diseases or conditions [1].PET imaging typically uses radiopharmaceuticals with short half-lives, which are preferably produced on site using cyclotron facilities and dedicated radiochemistry laboratories. However, the production process generates short-lived radioactive waste materials in the form of gas and liquid, which, if not controlled, can pose a threat to public health. Therefore, continuous monitoring of radioactive waste materials is essential for public safety[2].

As diagnostic imaging technologies and therapeutic perspectives continue to evolve and spread, and with the availability of increasingly targeted and effective radiopharmaceuticals, there is a growing need to ensure the safety of healthcare professionals and researchers who handle or administer radiopharmaceuticals on a daily basis. This has led to the development of systems that can synthesize, fractionate, or inject specific radiopharmaceuticals directly into patients in a completely automatic way, through a combined effort of engineering, physical, and medical-pharmaceutical knowledge. Some of these systems are fully automatic, while others are semi-automatic and operate inside shielded cells or are equipped with their own shielding. These sys-

tems minimize operator exposure to ionizing radiation and ensure high standards of precision, accuracy, and reproducibility in the handling processes of radiopharmaceuticals that are difficult to reach by manual operations.

This PhD program is an industrial project conducted in collaboration with Catania University, National Institute for Nuclear Physics (INFN-LNS), Tema Sinergie company, and Hochschule Mannheim University of Applied Science, with a main focus on the development and calibration of a Radiation Detector for Industrial and Medical Research Applications. The research activities are divided into two parts. The first part involves the development and characterization of a multichannel analyzer coupled with a NaI(Tl) scintillator as part of an international project called SPEKTRO, in continuous collaboration with the team at Georadis company based in Brno, Czech Republic, for waste radioactive material monitoring. The second part focuses on the development of a new activity measurement system for use in radiopharmaceutical automatic dispenser systems.

The first chapter of the thesis focuses on the theoretical background related to the research. The second chapter discusses the SPEKTRO project, which was conducted in Tema Sinergie company with the goal of developing a gamma detection system for use in radioactive waste management systems. In this project, the developed Multi Channel Analyzer (MCA) was tested in various environmental conditions, and the Energy and Efficiency calibration of the detection system was performed for all the geometries of radioactive waste management systems. The results of this study have been published in the Nuclear Science and Engineering journal[3]. The third chapter of the thesis pertains to the second phase of the PhD project, which involves the development of a real-time scintillation detector for use in an automatic dose dispenser.

Chapter 1

Theory

Nuclear medicine is a branch of medicine that focuses on the diagnosis and treatment of particular disorders, such as cancer, using specialized medications known as radiotracers or radiopharmaceuticals [4]. This chapter provides some basic nuclear medicine subjects which are of interest in this thesis.

1.1 Radioactivity

There are many nuclides that have a stable nucleus, while others have nuclei that are either unstable or radioactive. In the periodic table, all elements with an atomic number higher than bismuth (Z=83) are inherently unstable, and even some of the elements with atomic numbers lower than bismuth have at least one unstable isotope [5]. Radioactivity is the ability of some nuclei to undergo nuclear transition, and it is defined as that feature. The spontaneous fragmentation of a heavy nucleus into lighter nuclei is known as fission. The transition of a nucleus from an excited to a lower energy state is known as de-excitation. The transformation of a proton or neutron into another, which emits other fundamental particles and leads to the formation of a new nucleus, is another type of nuclear transformation (Beta decay under the influence of weak interaction). A radionuclide is a nuclide that is unstable and goes through the process of radioactive decay, which involves the emission of energy in the form of particles and radiation, the transformation of the nuclide into another nucleus, and the subsequent increase in the nucleus's level of stability. On the other hand, radioisotopes are a collection

of radionuclides that have the same number of protons but a variable number of neutrons [6].

1.1.1 Radioactive decay formula

Activity(A)is the amount of radioactive material measured by the quantity of radioactive atoms undergoing nuclear transition per unit of time(t). Mathematically speaking, activity is defined as the variation(dN) in the total number of radioactive atoms(N) over a specified time (dt), or:

$$A = -dN/dt \tag{1.1}$$

The reason of minus sign is decreases of the number of radioactive atoms with time. Units of curies have historically been used to express activity (Ci). The curie is called in honor of Marie Curie, a French chemist and physicist of Polish descent who received two Nobel prizes for her research on radioactive materials. One in physics (1903) for her work studying radioactivity with her husband Pierre Curie and Henri Becquerel, and one in chemistry (1911) for her discovery of the elements polonium and radium, the latter of which was named after her native Poland. Marie Curie first used the word "radioactivity" to describe the powerful radiation emissions from radium. One Ci is defined as 3.70×10^{10} disintegrations per second (dps), which is roughly equivalent to the rate at which 1g of radium-226 disintegrates (^{226}Ra) [7]. There is a lot of radioactivity in one curie. Nuclear medicine commonly uses radionuclides with activity between 0.1 and 30 mCi for imaging examinations and up to 300 mCi for iodine-131 therapy. The majority of scientific literature around the world utilizes the System International (SI) units, despite the fact that the curie is still the most often used radioactive measure in the United States. The SI unit for radioactivity is the becquerel (Bq), named after Henri Becquerel, who discovered radioactivity in 1896. The becquerel is defined as 1 dps. One millicurie (mCi) is equal to 37 megabecquerels (1 mCi = 37 MBq) [8].

1.1.2 Decay Constant

The process of radioactive decay is completely unpredictable. There is no way to know in advance which of the radioactive atoms present in a sample

will undergo decay from one instant to the next. Nevertheless, in order to determine the typical rate of nuclear transition, or decay, it is necessary to keep track of a large number of radioactive atoms over an extended period of time[8]. The number of atoms decaying per unit time (dN/dt) is proportional to the number of unstable atoms (N) that are present at any given time:

$$dN/dt \propto N \tag{1.2}$$

A proportionality can be transformed into an equality by introducing a constant. This constant is called the decay constant (λ).

$$-dN/dt = \lambda N \tag{1.3}$$

N is the number of radioactive nuclei that decay in the unit of time t, while λ is called the decay constant and is specific for each nucleus. By solving this equation we obtain:

$$N_t = N_0 e^{-\lambda t} \tag{1.4}$$

It is a continuous decreasing exponential function as indicated in Figure 1.1, which provides a statistical nature of the radioactive decay over time (N_t is the number of radionuclides at time t, N_0 is the number of radionuclides at t = 0).

1.1.3 Physical Half-Life

$T_{1/2}$ is known as the half-life and it defines the rate of radioactive decay. It is unique to each nucleus and correlates with the amount of time required for the number of unstable nuclides to half due to decay. The following expression relates the half-life and the decay constant [8]:

$$T_{1/2} = ln(2)/\lambda \tag{1.5}$$

τ is the average life of a radioactive nucleus and coincides with the average decay time, i.e. the period of time in which the radionuclide decays:

$$\tau = 1/\lambda \tag{1.6}$$

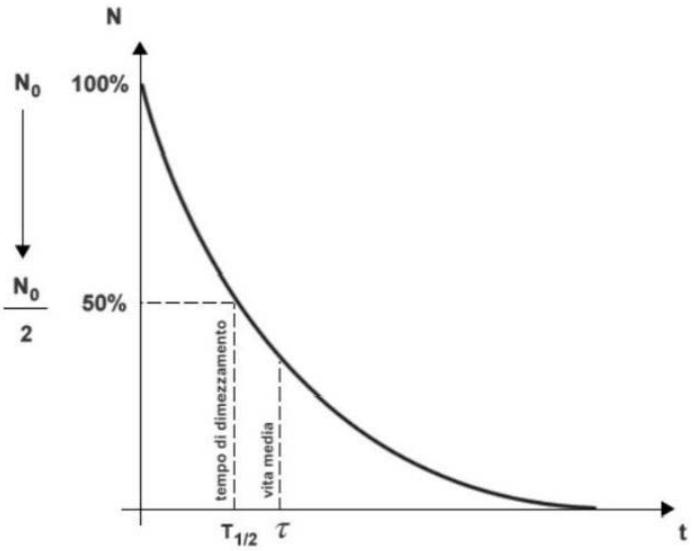

Figure 1.1: Exponential curve describing the radioactive decay [9]

1.2 Nuclear Transformation

Radiation is the result of an unstable atomic nucleus undergoing radioactive decay. This process is characterized by the emission of alpha particles (α decay), beta particles (β decay), gamma rays (γ decay), or electron capture. If the daughter nuclide produced is stable, the decay process stops. If not, the decay continues until a stable nuclide is formed. Beta decay is governed by the weak force, while alpha and gamma decay are controlled by the nuclear force and electromagnetism, respectively. Electron capture involves the unstable nucleus capturing an electron from one of its inner shells, causing a cascade of electrons to drop to lower shells and emit X-rays as a result[10].

1.2.1 α decay

Alpha decay is a form of radioactive decay that occurs spontaneously in heavy nuclides with atomic mass numbers greater than 150. During alpha decay, an alpha particle, which is identical to a helium nucleus containing two protons and two neutrons, is emitted. This decay process is often accompanied by the emission of gamma radiation. However, it is important to note

that photon emissions can also trigger opposing processes such as internal conversion and Auger electron emission. Alpha particles emitted from decay are considered the densest and weakest form of radiation, and they are not commonly used in medical imaging due to their limited ranges. Alpha particles have a range of about 1 cm/MeV in air and often less than 100 μm in tissue. This limited range makes it difficult for alpha particles to penetrate the skin's dead layer, and even the most powerful alpha particles are unable to do so. As a result, they are not suitable for medical imaging purposes.

1.2.2 β decay

The mechanism accountable for beta decay is the weak force. In three methods, beta decay occurs:

1.2.2.1 β-minus decay

Radionuclides with a neutron-to-proton ratio greater than one undergo beta-minus decay. During this transformation, a neutron is converted into a proton, emitting a beta-minus particle which equals to an electron and an electron antineutrino. The following equation can be used to explain beta-minus decay:

$$^{A}_{Z}\mathrm{X} \longrightarrow {}_{Z+1}{}^{A}\mathrm{Y} + \beta^{-} + \bar{\nu} + energy \tag{1.7}$$

1.2.2.2 β-plus decay

In beta-plus decay a proton transforms into a neutron, releasing a beta-plus particle which is the antimatter electron and an uncharged, nearly massless particle known as a neutrino. The daughter atom will have one fewer proton and one more neutron than the parent atom but the same mass number. The following equation can be used to explain beta-plus decay:

$$^{A}_{Z}\mathrm{X} \longrightarrow {}_{Z-1}{}^{A}\mathrm{Y} + \beta^{+} + \nu + energy \tag{1.8}$$

1.2.2.3 Electron Capture

Electron capture (ε) is an alternative to positron decay for neutron-deficient radionuclides. In this decay mechanism, the nucleus absorbs an orbital (often a K- or L-shell) electron, converting a proton into a neutron and emitting a neutrino at the same time. The following equation illustrates electron capture:

$$ {}^{A}_{Z}\mathrm{X} + e^{-} \longrightarrow {}_{Z-1}{}^{A}\mathrm{Y} + \beta^{+} + \nu + energy \tag{1.9} $$

1.2.3 γ Decay

Gamma decay is a fundamental process in nuclear physics that plays a key role in the understanding of nuclear structure and dynamics. It is a type of radioactive decay that occurs in atomic nuclei when a nucleus undergoes alpha or beta decay and leaves the daughter nucleus in an excited state. The excited nucleus can then release this excess energy by emitting gamma-ray photons. Gamma-rays are high-energy electromagnetic radiation with a wavelength shorter than that of X-rays. Gamma decay is unique in that it involves the emission of photons with extremely high energy and short wavelength. The gamma-ray photons carry no charge, but they have high energy and can penetrate dense materials, including lead and concrete. This makes gamma-rays useful in medical imaging and radiation therapy. The emission of a gamma-ray photon from an excited nucleus is a quantum mechanical process that causes the nucleus to transition to a lower energy state. This transition may occur via the emission of one or more gamma-rays until the nucleus reaches its ground state. Gamma decay is a statistical process that is characterized by a half-life, which is the time it takes for half of the excited nuclei to decay. Gamma decay has many important applications in various fields, including nuclear physics, astrophysics, medicine, and industry. For example, gamma-ray spectroscopy is a powerful tool used to study nuclear structure and dynamics, while gamma-ray imaging is used for medical diagnosis and treatment of diseases such as cancer. Gamma decay is also used in the detection of radioactive materials and in the sterilization of medical equipment. In conclusion, gamma decay is a crucial process in nuclear physics that involves the emission of high-energy gamma-ray photons from excited atomic nuclei. The understanding of gamma decay and its applications is essential in the fields of nuclear physics, astrophysics, medicine, and industry.

1.3 Radiation Interactions Through Matter

The performance of a radiation detector is heavily dependent on the interaction of the radiation being detected with the detector material. Understanding how different types of radiation interact with matter and lose energy is crucial in comprehending the operation of radiation detectors. Radiation can be classified as charged particles (such as heavy charged particles and fast electrons) and uncharged particles (such as neutrons, X-rays, and gamma rays). Charged particles interact continuously with the electrons present in any medium they travel through via the Coulomb force. On the other hand, uncharged particles must first undergo a "catastrophic" interaction that profoundly modifies their properties in a single encounter. In practical scenarios, this interaction results in the complete or partial transfer of the incident radiation's energy to the electrons or nuclei of constituent atoms, or to charged particle byproducts of nuclear processes. However, if this interaction does not occur within the detector, uncharged particles such as neutrons or gamma rays can pass through the detector without leaving any trace[11][10]. In this thesis, our main focus is on understanding the physics of gamma interactions with matter, which plays a critical role in the operation of gamma radiation detectors.

1.3.1 Gamma-Ray Interactions

Gamma ray interactions with materials can take place in a wide variety of ways; however, only three main categories are crucial for radiation measurements[12]:

1.3.1.1 Photoelectric Absorption

A photon interacts with an absorber atom in the photoelectric absorption process, and the photon entirely disappears. Instead, the atom ejects an energetic photo electron from one of its bonded shells, with energy E_{e^-} supplied by:

$$E_e- = h\nu - E_b \tag{1.10}$$

where $h\nu = E_\gamma$ is the photon energy and E_b is the binding energy of the photoelectron in its original shell. The empty spot in the electron shell left

by the photoelectron emission is immediately filled by a reorganization of the electrons in the shell. The binding energy is dissipated as either a recognizable X-ray or an Auger electron. Photoelectric interactions with the outer electron shells of the absorber atoms can cause the identifying X-rays to be reabsorbed after a fair distance of travel. In this way, photoelectric absorption releases a photoelectron, which absorbs and transports the vast majority of the gamma ray's energy, as well as one or more low-energy electrons. Lower energy gamma rays (or X-rays) interact mostly through the photoelectric process.Materials with a high atomic number Z also experience improvements due to the procedure. The probability of photoelectric absorption by a single atom does not have a unique analytic equation that holds true across all values of E_γ and Z, but a fair estimate is as follows:

$$\sigma_P h \propto \frac{Z^n}{E_\gamma^{3.5}} \tag{1.11}$$

where the exponent n varies between 4 and 5 over the gamma-ray energy region. Photoelectric absorption is an ideal process for measuring the original gamma-ray energy as, if all the liberated electrons can be collected, the sum of all their kinetic energies, is equal to the energy of the gamma-ray photon.

1.3.1.2 Compton Scattering

Compton scattering involves the interaction of a gamma-ray photon with an electron in the absorber material. The entering gamma-ray photon is scattered away from its initial path by an angle equal to θ. Recoiling electrons are created when a photon imparts some of its energy to an originally bound electron. Given an interaction, energy and momentum conservation lead to an expression for the relationship between the transferred energy and the scattering angle, which is:

$$h\nu' = \frac{h\nu}{1 + \frac{h\nu}{m_e c^2}(1 - \cos\theta)} \tag{1.12}$$

where $m_e c^2$ is the rest-mass energy of the electron (0.511 MeV). The kinetic energy of the recoil electron is therefore:

$$E_e- = h\nu - h\nu' = h\nu(\frac{(\frac{h\nu}{m_ec^2})(1-\cos\theta)}{1+(\frac{h\nu}{m_ec^2})(1-\cos\theta)}) \tag{1.13}$$

E_e- can take any value between 0 and $h\nu(\frac{2h\nu/m_ec^2}{1+2h\nu/m_ec^2})$ which is related to $\theta = 0, \pi$ respectively.

The difference between the maximum compton recoil energy and the incident gamma ray energy is:

$$E_{gap} = h\nu - E_e^{max}- = \frac{h\nu}{1+2h\nu/m_ec^2} \tag{1.14}$$

If the incident gamma ray energy is very large (i.e. $h\nu \gg \frac{m_ec^2}{2}$), the gap energy tends toward the constant value equal to 0.256 MeV.

The probability of Compton scattering per atom of the absorber depends on the number of electrons available as scattering targets and therefore increases linearly with Z. The angular distribution of scattered gamma rays is predicted by the Klein-Nishina formula for the differential scattering cross section $d\sigma_{KN}/d\Omega$:

$$\frac{d\sigma_{KN}}{d\Omega} = Zr_0^2(\frac{1}{1+\alpha(1-\cos\theta)})^2(\frac{1+\cos^2\theta}{2})(1+\frac{\alpha^2(1-\cos\theta)^2}{(1+\cos^2\theta)[1+\alpha(1-\cos\theta)]}) \tag{1.15}$$

Where $\alpha \equiv h\nu/m_ec^2$ and r_0 is the classical electron radius.

1.3.1.3 Pair Production

Pair production is energetically feasible if the gamma-ray energy is greater than 1.02 MeV, which is double the electron's rest mass energy. The gamma ray photon is destroyed in the interaction and is replaced with an electron-positron pair, which can only occur within the nucleus' Coulomb field. All the excess energy carried in by the photon above the 1.02 MeV, required to create the pair, goes into kinetic energy shared by the positron and the electron. The chance of pair production per nucleus cannot be expressed simply, but it changes roughly with the square of the atomic number Z of the absorber material [13] [11].

1.4 Ionizing Radiation Detectors

In general, ionizing radiation causes matter to ionize and/or get excited, which releases energy into the material. Chemical alterations, visible light, or ultraviolet (UV) radiation emissions can result from excitation and ionization. The interaction of ionizing radiation with matter is the basis for the operation of all ionizing radiation detectors. They produce an electrical signal after each particle or photon interaction. The generated signal needs to go through a number of electronic circuits for signal amplification, signal processing, and data storage in order to be processed. The two basic techniques for processing signals are pulse mode and current mode. In pulse mode, each interaction's signal is handled separately. In current mode, an average of all the electrical signals from the interactions is used to make a net current signal. Depending on how they detect radiations, there are several sorts of detectors. Three types of detectors are discussed in the sections that follow [11][14].

1.4.1 Ionization Chambers

One of the most common forms of radiation detectors is an ionization chamber. There are several different types of gas-filled detectors, and one of them, called an ion chamber, consists of a gas volume and two electrodes. Ion chambers are the most basic gas-filled detectors in theory. The standard operation relies on capturing all the charges produced by direct ionization within the gas by the application of an electric field. The ensuing positive ion and free electron from ionizing a neutral molecule is known as an ion pair, and it serves as the basic ingredient of the electrical signal produced by the ion chamber. Ions can be created directly by interacting with the incident particle, or indirectly by transferring some of the particle energy to an energetic electron or "delta ray". Regardless of the specific mechanisms at work, the practical quantity of importance is the total number of ion pairs produced along the radiation's path. Ion chambers are typically employed in current mode as direct-current (dc) devices [11]. Figure 1.2 shows the ionization chamber device.

Figure 1.2: Ionization Chamber

1.4.2 Scintillation Detectors

The detection of ionizing radiation using the scintillation light that particular materials release was one of the earliest techniques known to science. Scintillation materials are substances that emit ultraviolet and/or visible light in response to ionizing radiation. One of the greatest methods for spectroscopy and radiation detection is still the scintillation process. There are two types of scintillation material: organic and inorganic. Both their chemical composition and how they produce light differ. Inorganic scintillators are crystalline solids that emit light due to their distinctive crystal structure. In their crystalline structure, they can only emit light. Inorganic scintillators, such as NaI crystal, can glow in their pure state at liquid nitrogen temperatures. Most crystals need impurities to alter their crystalline structure, which is responsible for scintillation. A small amount of thallium impurity, for example, is required for NaI crystal to scintillate light efficiently at room temperature. The principle of scintillation light production in an inorganic scintillator is based on the fact that when ionizing radiation passes through an inorganic scintillator, the energy absorbed creates an electron-hole pair and raises the electron to the conduction band, leaving a hole with a positive charge in the valence band. The electron will eventually return to the valence band and recombine

with the hole. The item emits photons. In contrast to inorganic scintillators, the fluorescence process in organic scintillators is a molecular characteristic. This indicates that the scintillator can emit light regardless of its physical conditions. Organic scintillators can exist as organic crystals, such as naphthalene, stilbene, and anthracene, as well as plastics and liquids. Plastic and liquid scintillators are the most popular organic scintillators because they are readily available in a variety of sizes and shapes. The mechanism of scintillation in organic scintillators is essentially the excitation of an atom within the molecule. While de-excitation happens, it emits scintillation photons. Generally, scintillating light cannot be used for analysis until it is transformed into an electrical signal. So, a photodetector which transforms light into electrical impulses is used in scintillation detectors. The next sections will address the advantages and disadvantages of these technology[11]. Figure 1.3 depicts some scintillation materials.

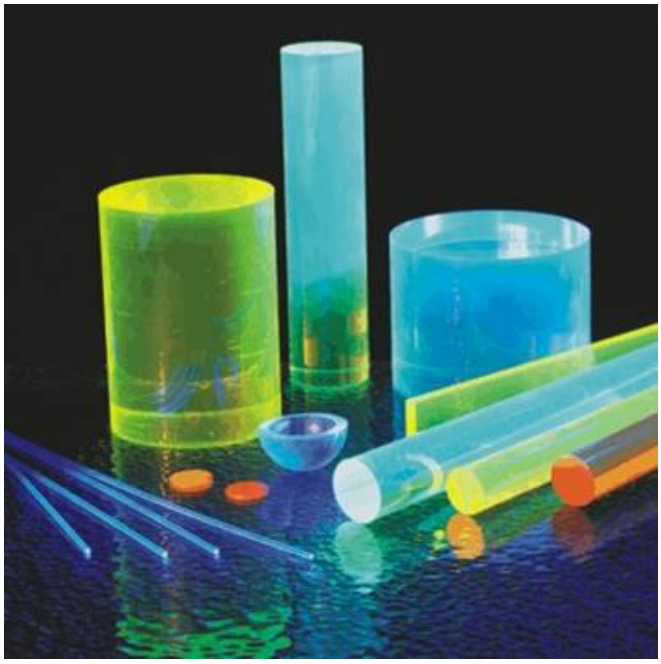

Figure 1.3: Scintillation Materials

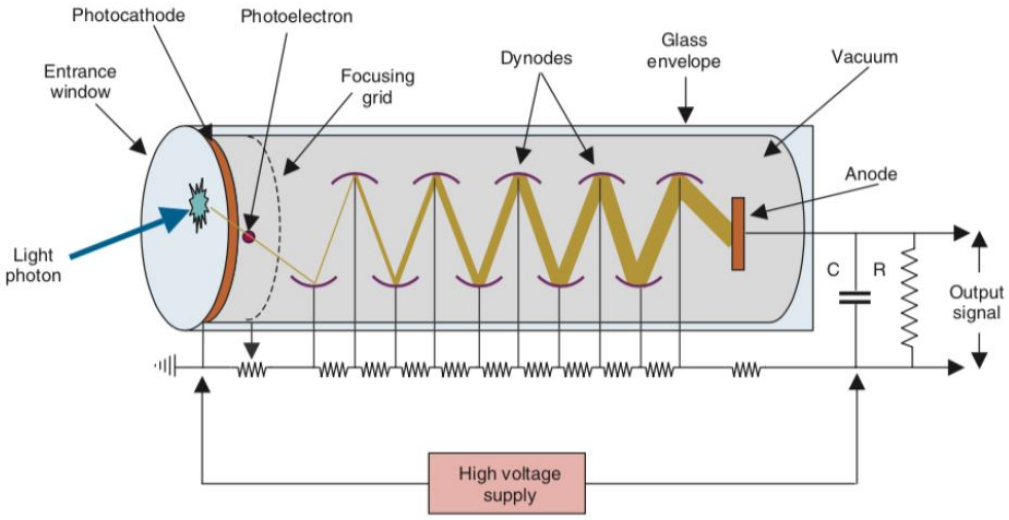

Figure 1.4: Slicing a photomultiplier tube in half lengthwise reveals its inner workings [6].

1.4.2.1 Photo Multiplier Tube

Devices called photomultiplier tubes (PMTs) can convert light into a large number of electrons. A PMT usually has a photocathode, a number of electrodes (dynodes), and electronics for the anode or readout that are hidden inside a vacuum tube. Photons enter the PMT through a transparent window and strike the photocathode at the window's inner layer. The photoelectric effect converts each photon into an electron. The potential difference between dynodes accelerates electrons toward the dynode located behind the photocathode. Each dynode is more positive than the preceding one. Dynodes are nickel- or steel-based metallic structures. The dynode emits more electrons, which are then driven toward another dynode that emits more electrons. This procedure is ongoing until electrons reach the anode. Anode electrons are converted to output current, which is monitored by readout circuitry.Figure 1.4 shows the PMT's components [6].

Major benefits of PMTs include their high sensitivity to light (UV, visible, and infrared), quick temporal response, and strong signal-to-noise (SNR) ratio. The drawbacks of PMTs are their low quantum efficiency, large size, high voltage operation, and sensitivity to magnetic fields. One of the most crucial

factors to consider when selecting a photodetector for the suggested detector system is size. This is especially valid when using small scintillators.

1.4.2.2 Silicon Photo Multiplier

SiPMs are made by doping Silicon wafers to create a p-n junction type of diode. The avalanche mechanism works best with silicon that has only a small amount of doping. SiPMs are made up of discrete pixels that are both electrically and optically isolated from one another. Each pixel, also known as a micro-cell, is equipped with its own quenching resistor, which puts an end to the discharge. When all of the signals from the microcells are added together, the resulting signal is proportional to the number of microcells that have been activated. An electron-hole pair is produced whenever a photon is absorbed into a system. Electrons and holes are both sped up by the electric field, and the resulting increase in energy is sufficient to produce additional electron-hole pairs and initiate a discharge. A process known as "impact ionization" is what happens when a sufficiently high electric field is generated within the depletion region of the silicon (greater than 5×10^5 V/cm). This causes a charge carrier that is created in this region to be accelerated to a point where it carries sufficient kinetic energy to create secondary charge pairs. In this approach, a single photon can set off a cascade of ionization that is self-sustaining and will extend across the entirety of the silicon volume that is being affected by the field. The silicon diode will eventually fail and turn conductive, essentially turning the initial photoelectrons into a significant flow of current at the macroscopic scale. The term "Geiger discharge" refers to this phenomenon since it is similar to the ionization discharge that may be seen in a Geiger-Müller tube. A geiger mode operation is performed on each individual pixel, whereas an avalanche mode operation is carried out when many pixels are combined. It is possible that the charge carrier that sets off the avalanche was formed by a process of photon absorption or thermal excitation (thermal noise), or it could have been liberated from a flaw in the silicon lattice (after-pulse). All three of these scenarios are possible [11]. Figure 1.5 shows the SiPM structure.

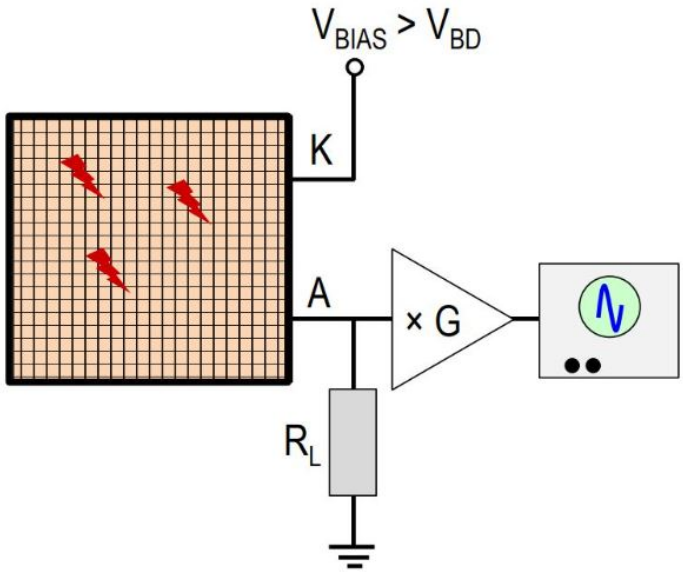

Figure 1.5: SiPM structure

1.4.3 Semiconductor Detectors

Semiconductor detectors have become a crucial tool in the field of radiation detection, finding applications in medical imaging, environmental monitoring, and nuclear physics research. These devices are capable of detecting ionizing radiation by measuring the electrical current produced when the radiation interacts with a semiconductor material. The basic structure of a semiconductor detector consists of a thin slice of semiconductor material, such as silicon or germanium, with electrodes on either side. When ionizing radiation passes through the detector, it generates electron-hole pairs in the semiconductor material. These charges are then collected by the electrodes, producing a measurable electrical signal. One of the advantages of using a solid detecting medium, such as semiconductor detectors, is that they have densities roughly 1000 times greater than those for gases, allowing for substantially smaller detector dimensions for the observation of high-energy electrons or gamma rays. There are several types of semiconductor detectors, including p-n junction detectors, silicon strip detectors, and high-purity germanium detectors, each with their own set of advantages and disadvantages depending on the specific application. In recent years, semiconductor detec-

tors have made significant contributions to the fields of particle physics and nuclear astrophysics. In particular, high-purity germanium detectors have proven to be an invaluable tool for the study of rare nuclear decays and dark matter. Additionally, semiconductor detectors are increasingly being used in medical imaging, where they offer high sensitivity and spatial resolution. Overall, semiconductor detectors have proven to be a versatile and reliable tool for radiation detection, with wide-ranging applications across many different fields. Further research in this area holds great promise for improving the sensitivity, resolution, and capabilities of these devices, and for expanding their use to new areas of scientific inquiry [11][15].

1.5 Gamma Spectroscopy

Gamma-ray spectroscopy is the quantitative analysis of the energy spectra of gamma-ray sources. Gamma rays, which come in a wide range of energy and intensities, are emitted by the vast majority of radioactive sources. A gamma-ray energy spectrum can be created by using a spectroscopic instrument to identify and examine these emissions[16].

Nuclear spectrometry now has a wide range of alternatives and advantages that were not previously possible with traditional analog technology. In several fields of nuclear instrumentation, digital technology is gradually taking the place of analog technology. Analog pulse processing has been replaced by digital pulse processing (DPP), which enhances spectroscopic performance and reliability. The devices' light weight, small size, and low power further enhance data quality and reliability for research-based nuclear spectroscopy systems. Primary components of a gamma spectrometer are the energy-sensitive radiation detector, such as a scintillation or semiconductor detector, and the electronic equipment that evaluates the detector's output signals, such as the Single Channel Analyzer (SCA) and Multi-Channel Analyzer (MCA).

A single channel analyzer (SCA) is an electronic device that counts or detects events that fall within a specific energy range. It works by setting a lower and upper energy threshold for incoming signals and only counting or detecting signals that fall within this range. The output of an SCA is usually a pulse or a logical signal indicating the detection of an event within the specified energy range. SCAs are commonly used in nuclear physics

experiments and radiation detection systems.

A multi-channel analyzer (MCA) is an electronic device that measures and analyzes the energy spectrum of incoming signals. It works by digitizing the incoming analog signal from a detector and sorting the resulting digital values into channels based on their energy level. Each channel represents a specific energy range, and the number of counts in each channel is proportional to the intensity of the corresponding energy range. The output of an MCA is usually a histogram which represents a pulse-height spectrum of the gamma-ray interactions in the detector. This needs to be calibrated into the energy spectrum of the gamma-rays, which shows the distribution of energy levels in the incoming signal. The working principle of an MCA can be summarized in four steps:

1. The incoming analog signal is amplified and digitized by an ADC.
2. The resulting digital values are sorted into channels based on their energy level using a multi-channel scaler (MCS).
3. The number of counts in each channel is accumulated over a period of time to create a histogram.
4. The histogram is analyzed to determine the energy spectrum of the incoming signal.

The spectrum provides intensity at each energy level, and the radiation identifies the peaks. Variations in temperature and other factors like noise sources may further affect performance of the whole radiation detection system. so the implementation of the different algorithms to compensate these effects is necessary [17].

Figure 1.6 shows a typical gamma spectrum which is composed of:

1. a first continuum due to the single Compton scatterings;
2. a second continuum due to the Multiple Compton scatterings;
3. a Double Escape Peak superimposed on the first continuum, due to the pair production where both the annihilation photons escape from the detector without interacting, situated at the energy value: $h\nu - 2m_e c^2$;

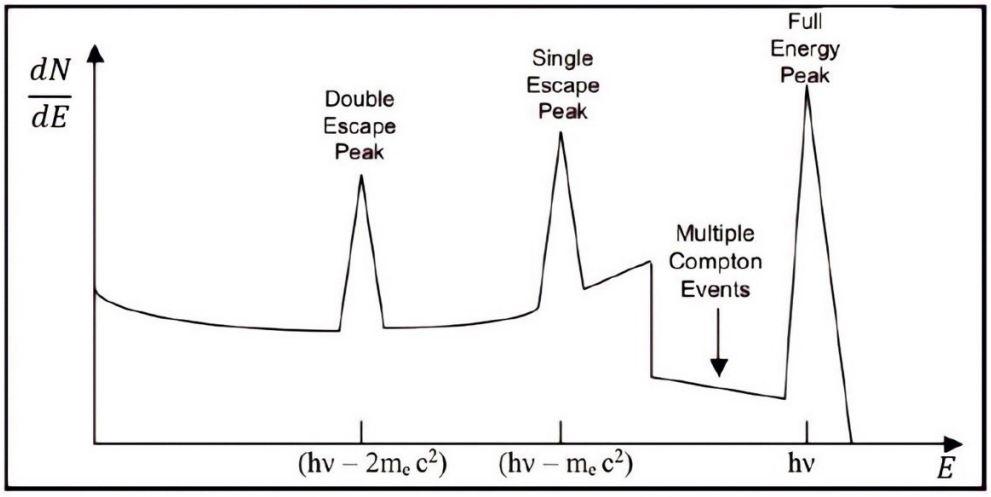

Figure 1.6: NaI(Tl) typical gamma ray spectrum

4. a Single Escape Peak superimposed on the first continuum, due to the pair production where one of the annihilation photons escapes from the detector without interacting, situated at the energy value: $h\nu - m_e c^2$;

5. a Full Energy Peak, situated at the energy value $h\nu$, due to the events in which all the primary gamma-ray photon energy has been deposited in the detector active volume. Along with the full energy peak, the single escape peak, and the double escape peak, there is a continuous range of possibilities for the pair production process in which the annihilation photons partially release their energy in the detector medium before escaping. These events accumulate in a broad continuum, filling the region of the pulse height spectrum between the double and single escape peaks.

   Beside this, other complications in the aspect of the pulse height spectrum arises from other causes, the main ones being:

6. Secondary electron escape: A significant portion of these electrons may escape from the detector surface, and their energy will not be fully captured if the detector is too small in comparison to normal secondary electron ranges. The response function is distorted as a result.

7. Bremsstrahlung escape: The emission of bremsstrahlung photons is one way that secondary electrons might lose energy. There is a chance that some bremsstrahlung photons will escape without being reabsorbed, even if the electron is completely stopped inside the detector. The result is a deformation of the response function, similar to the secondary electron escape.

8. As we saw, when a gamma-ray photon is subjected to photoelectric absorption, an X-ray is released in order to liberate the binding energy. This X-ray is typically reabsorbed close to the site of the initial contact. The X-ray might, however, escape if the photoelectric absorption takes place close to the surface of the detector. Consequently, a new peak in the response function will emerge below the photopeak at a distance equal to the energy of the characteristic X-ray.

1.6 Radionuclide Production

Although there are numerous naturally occurring radioactive nuclides, all of those supplied to patients in nuclear medicine are synthesized. The majority of radionuclides employed in nuclear medicine are generated by particle accelerators (e.g., cyclotrons), nuclear reactors, or radionuclide generators. Cyclotrons and radionuclide generators will be explained below.

1.6.1 Cyclotron

Radionuclides used in medicine can be produced through various methods, including the use of cyclotrons and other particle accelerators. These devices accelerate charged particles, which are then directed to bombard stable nuclei with high-energy. While cyclotrons are commonly employed for this purpose, it is important to note that they are not the sole method of radionuclide production for clinical use.

In cyclotrons, which consist of a vacuum chamber positioned between the poles of an electromagnet, the acceleration process takes place. Inside the vacuum chamber, a pair of semicircular electrodes known as "dees" are situated. These dees, resembling the letter "D," are separated by a small gap. A

high radiofrequency (RF) field is applied between the electrodes. When positive ions are introduced into the center of the cyclotron, they are attracted to the negatively charged dee and propelled towards it. The static magnetic field causes the ions to travel in a circular path, with the radius of the circle expanding as the ions gain kinetic energy. When the ions reach the space between the dees, the polarity of the electrical field between the two dees flips, resulting in the acceleration of the ions towards the negative dee. This cycle is repeated continuously, with each passage through the gap providing a boost in momentum and leading to the creation of increasingly larger arcs of kinetic energy. The time interval between accelerations remains constant, while the distance between subsequent accelerations grows, causing the particle's speed to increase. This cyclical nature of the process gives rise to the term "cyclotron." The specific type of particle (e.g., protons, deuterons) being accelerated, the diameter of the dees, and the strength of the static magnetic field all influence the final kinetic energy attained by the particles. As the ions approach the edge of the dees, a negatively charged deflector plate (for positive ions) or an electron stripping foil (for negative hydrogen ions) is used to divert them from their circular path. This diversion allows the ions to pass through a window and impact the target material. The energy of the incident particles can range from a few million electron volts (MeV) to several hundred MeV, depending on the specific cyclotron configuration. When the accelerated ions collide with the target nuclei, nuclear reactions occur. The energy of the incident particle can be transferred to the target nucleus, or the incident particle may be fully absorbed. The exact reaction depends on factors such as the type, energy, and composition of the incident particle and the properties of the target. The target nuclei are left in an excited state, and their energy is subsequently released as electromagnetic radiation (gamma rays) and particle radiation (protons and neutrons). Cyclotrons employ the acceleration of both positive and negative ions, which are subsequently converted to positive ions at the end of the acceleration process. It is important to note that negative ions themselves do not directly contribute to the activation process. Instead, the technology of cyclotrons allows for the acceleration of both positive and negative ions, and it is the positive ions that play a key role in the activation of target nuclei. In a cyclotron, when ions (whether positive or negative) are introduced into the center of the device, they are drawn towards the negatively charged dee and propelled towards it. The

static magnetic field causes the ions to travel in a circular path, with the radius of the circle increasing as the ions gain kinetic energy. When the ions reach the space between the dees, the polarity of the electrical field between them flips, causing the ions to be accelerated towards the negative dee. During this process, negative ions can be converted to positive ions. For instance, in the case of accelerating negative hydrogen ions (H^-), a carbon stripping foil is employed. This foil removes the excess electrons from the negatively charged ions, resulting in the production of positively charged hydrogen ions (H^+). The change in polarity for each particle's charge then allows the magnetic field forces to act in the opposite direction, facilitating the extraction of the beam from the cyclotron. Therefore, while negative ions are utilized during the acceleration phase, it is the subsequent conversion to positive ions that enables the ions to participate in the activation process when they collide with target nuclei. The introduction of both positive and negative ions in cyclotrons provides flexibility in the choice of particles to be accelerated and allows for the production of various radionuclides used in medical applications.

For the production of positron-emitting radionuclides, particularly those utilized in positron emission tomography (PET), various cyclotrons are employed. These cyclotrons are utilized by both commercial producers and hospitals for radionuclide production. The energy range at which these cyclotrons operate can vary depending on the intended scale of production and distribution.

To meet the demand for localized production or short-range distribution, especially for PET radionuclides, smaller specialized cyclotrons have been developed and deployed in commercial radiopharmacies serving urban regions or hospitals. These cyclotrons typically accelerate negative hydrogen ions (H^-) at lower energies, typically ranging from approximately 10 to 20 MeV. In contrast, large-scale production and wide-range commercial distribution of radionuclides involve the utilization of cyclotrons operating at higher energies, typically ranging from 30 to 70 MeV. These cyclotrons cater to the broader demand for radionuclides and are capable of supplying a wider geographical region with various radiopharmaceuticals[8][18][19]. Figure 1.8 depicts the schematic of a cyclotron.

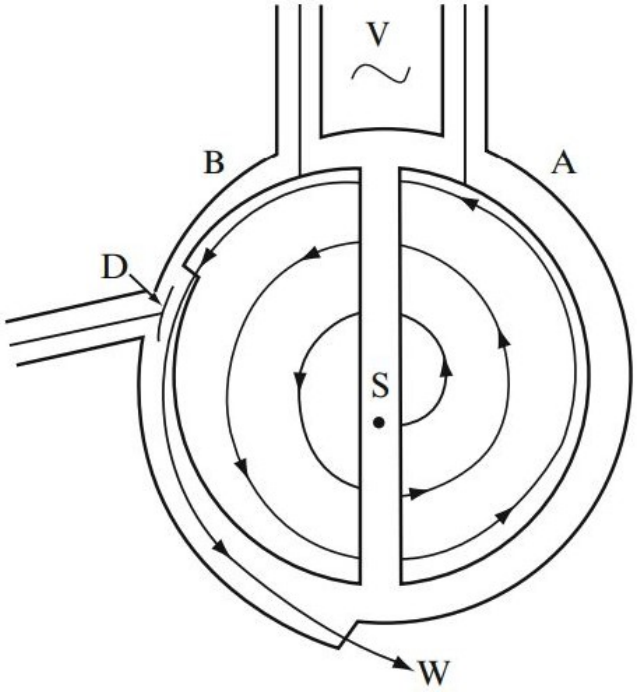

Figure 1.7: Schematic of a cycltron, V alternating voltage, S ion source, A and B dees with vacuum, D deflector, W window [20].

1.6.2 Radionuclide Generators

Radionuclide generators are widely used in nuclear medicine for producing short-lived medicinal radionuclides. The production process is based on the radioactive decay of a non-medical, long-lived parent radionuclide into a useful daughter radionuclide. Two fundamental concepts that govern the production process are secular equilibrium and transient equilibrium. Secular equilibrium refers to a state in which the rate of production of the daughter radionuclide is equal to its rate of decay. In other words, the parent and daughter radionuclides are in a state of equilibrium, and their activities remain constant over an extended period. The equilibrium is achieved when the half-life of the parent radionuclide is significantly longer than that of the daughter radionuclide. In radionuclide generators, the parent radionuclide is immobilized on a column, and the daughter radionuclide is continuously produced as long as the parent radionuclide is available. The separation of daughter from parent can be achieved by elution, and the daughter can be

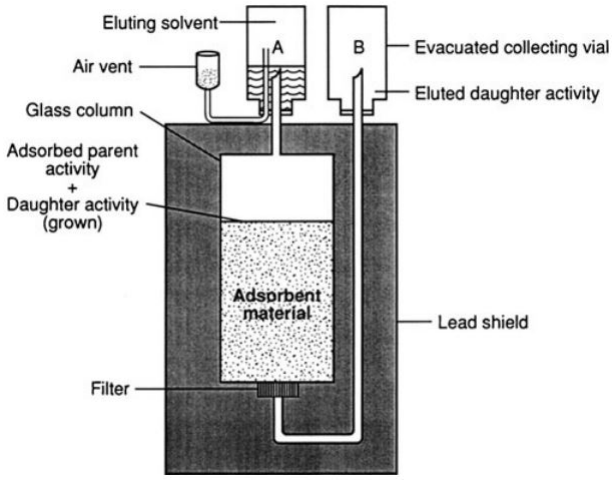

Figure 1.8: Typical generator system[20].

further processed for medical use. Transient equilibrium, on the other hand, refers to a state in which the production rate of the daughter radionuclide is much higher than its rate of decay. This state is typically achieved when the half-life of the parent radionuclide is comparable to or shorter than that of the daughter radionuclide. In this case, the parent and daughter radionuclides are not in equilibrium, and their activities change rapidly over time. Transient equilibrium is often utilized in nuclear research and in certain therapeutic applications where the daughter radionuclide is required in large quantities and short-lived. In conclusion, the concepts of secular and transient equilibrium play a crucial role in the production of short-lived medicinal radionuclides using radionuclide generators. The appropriate choice of parent and daughter radionuclides, as well as the design of the generator, are critical factors in achieving the desired equilibrium state for optimal production of the daughter radionuclide[8].

1.7 Radionuclides for Medicine

The clinical application of radionuclides depends on the nature of the radiation released during their radioactive decay. Therefore, radionuclides are broadly classified into two groups: those used for diagnosis and those used

for treatment. Diagnostic radionuclides are recognized by a significant photon emission, preferably in the form of gamma radiation. In order to employ radionuclides for diagnostic purposes, they must either decay by nuclear deexcitation or by emitting positrons (β^+), which lead to an annihilation process and, ultimately, the production of annihilation photons. Since gamma radiations are composed of massless, high-energy photons, using them provides the benefit of reducing the dose absorbed by the patient. Since γ photons can travel great distances before losing all of their energy, they are able to reach the detectors of diagnostic devices with enough energy to give a signal that can be used. This means that γ photons have a very low probability of interacting with biological tissues. Contrarily, the radionuclides most frequently utilized for therapeutic reasons are distinguished by the emission of particles with masses like α and β, given that the likelihood that these particles would interact with biological tissues rises with increasing mass. The objective is to make sure that these particles collect specifically in pathogenic tissues, where they will deposit a high enough dose of radioactivity to cause the death of diseased cells. The lethal dose delivered to biological tissue by an alpha emitting radionuclide is substantially larger than that supplied from a beta emitter. This is primarily attributed to the fact that alpha particles have a much greater mass than beta particles for the same contact period between the radionuclide and the target cells. However, it is important to note that the concept of LET (Linear Energy Transfer) is a crucial factor in understanding this difference. Alpha particles consist of two protons and two neutrons, forming helium nuclei. Due to their larger mass and charge, alpha particles have a higher LET compared to beta particles. LET refers to the amount of energy transferred per unit length traveled by a particle in a material. When an alpha particle interacts with biological tissue, it deposits its energy over a very short distance, typically a few micrometers. This short-range nature of alpha particles causes them to deposit a significant amount of energy within a small volume of tissue, leading to a higher likelihood of causing damage to nearby cells. Consequently, alpha emitters are more harmful to biological tissue as they can cause more severe localized damage. On the other hand, beta particles, which are high-energy electrons or positrons, have a smaller mass and charge compared to alpha particles. They have a lower LET and can travel further before depositing their energy. Beta particles can penetrate deeper into tissues and may cause damage to a larger volume of cells along

their path. However, the larger mass of alpha particles, coupled with their higher LET, results in a more concentrated energy deposition within a smaller area, leading to a higher potential for damage in the immediate vicinity of the radioactive source. Therefore, while the mass of the particles does play a role in the difference between the lethal doses delivered by alpha and beta emitters, it is the higher LET of alpha particles that significantly contributes to their increased potential for causing damage to biological tissue. The half-life, the time required to prepare the related radiopharmaceutical, the pharmacokinetic features, the mode of image capture, and other important factors must also be considered when identifying radionuclides for medical applications. Contrarily, a long half-life between a few days and tens of hours is preferred for radionuclides with greater therapeutic potential, as this allows the radionuclide to deposit a lethal dose of radioactivity for a long time in the diseased tissue, favoring a more efficient destruction of the target cells.

The characteristics of some of the most interesting radionuclides for medical applications are briefly described below:

- ^{18}F:

^{18}F is a radioactive isotope of fluorine which decays in 97% of cases by emitting a β^+ positron, or in the remaining 3% by electron capture. The half-life is equal to 109.77 minutes and is produced in cyclotrons for medical use (10-18 MeV). The energy of β^+ positrons is relatively low (0.836 MeV) and they travel an average distance of 2.3 mm before triggering annihilation. These characteristics, together with the fact that its half-life makes it compatible with the kinetics and bio-distribution of many biological molecules, make it the best radioisotope for PET diagnostics. Its growing demand has stimulated research activities and the development of ever more efficient production systems. The most widely used nuclear reaction for its production is ^{18}O(p,n)^{18}F, which leads to the production of fluorine-18 in the form of $[^{18}F]F^-$ in aqueous solution.

- ^{99m}Tc:

^{99m}Tc is a radioactive metastable nuclear isomer of ^{99}Tc, widely used in the synthesis of radiopharmaceuticals for SPECT diagnostics. It is easily avail-

able through the $^{99}Mo/^{99m}Tc$ generator, under controlled sterility and non-pyrogenic conditions by means of a simple elution. It has excellent physical properties such as a half-life of 6.02h, a gamma energy emission of 142 keV and low tissue attenuation. These characteristics make it perfect for diagnostic gamma camera detection. Furthermore, this radioisotope can produce a wide range of radiopharmaceuticals due to the chemical adaptability of ^{99m}Tc in terms of the width of the range of oxidation states.

- ^{11}C:

^{11}C decays by emitting β^+ positrons into ^{11}B (stable) and has a half-life of 20.4 minutes. These properties together with the fact that by replacing a stable ^{12}C atom with one of ^{11}C within a molecule, the metabolic fate is practically indistinguishable from the natural compound in many cases make it very attractive for medical applications. The short half-life of ^{11}C not only necessitates its use right at the source, but also places restrictions on diagnostic imaging by requiring consideration of the time required for the radiotracer to enter the circulation and accumulate in the body area of interest with a sufficient signal-to-noise ratio after administration.However, in contrast to ^{18}F, the short half-life ensures that both the patient and the medical staff engaged will be exposed to a lower radiation dose. One other thing to keep in mind is that ^{11}C, in comparison to ^{18}F, has a more energetic β^+ emission, which translates to a degradation of the spatial resolution in the acquisition of diagnostic PET images. The two most popular and intriguing nuclear reactions for producing ^{11}C are ^{10}B(d,n)^{11}C and ^{14}N(p,α)^{11}C.

- ^{68}Ga:

^{68}Ga is a radionuclide that derives from the decay of ^{68}Ge and which in turn undergoes in 88.91% of cases a radioactive decay with β^+ positron emission leading to stable zinc-68, while in the remaining 11.09% of cases decay via electron capture.It has a half-life of 67.71 minutes and is compatible with the pharmacokinetics of low molecular weight molecules such as peptides, antibody fragments, aptamers and oligonucleotides. The energy associated with the emitted positrons is clearly higher than those emitted by Fluorine-18 and carbon-11, however the loss of spatial resolution in diagnostic imaging

is not so marked because it is counterbalanced by a high receptor specificity and by a low noise, characteristic of the most well-known radiopharmaceuticals labeled with gallium-68.It is currently obtained in solid-phase generators, which are capable of eluting Gallium-68 in ionic form ($[^{68}Ga]Ga^{3+}$) and therefore suitable for radiolabelling a wide range of organic molecules.

- ^{13}N:

^{13}N is a positron emitter with a very short half life of 9.97 minutes, therefore requiring an on-site cyclotron for its production, through the nuclear reaction: ^{16}O (p,α)^{13}N.

1.8 Definition of Radiopharmaceutical and Radioactive Labelling

Radiopharmaceuticals are pharmaceutical products that contain a radionuclide, which is a radioactive isotope of an element. These radiopharmaceuticals are specifically designed to provide a valuable source of ionizing radiation for diagnostic and therapeutic purposes in medicine. Because they are mostly delivered intravenously, sterility, apyrogenity, and other quality control factors must be rigorously confirmed. Radiopharmaceuticals radiolabeled with ^{18}F have the most potential for use in clinical diagnostics. In the following we will discuss some of the radiopharmaceuticals based on ^{18}F:

- ^{18}F-FDG

When it comes to PET imaging for oncological diagnosis and therapy evaluation, ^{18}F-fluorodeoxyglucose is by far the most utilized radiopharmaceutical. By competing with glucose for entrance into cells, it provides a biomarker of metabolic activity in a wide range of tissues and malignancies. Because of its polar nature, ^{18}F-FDG cannot be metabolized after it enters the cell and instead becomes locked there once it is phosphorylated. Malignant tissues, which have an accelerated or uncontrolled metabolism, reveal a greater number of glucose membrane transporters, leading to a higher rate of glucose entry into cells and subsequent phosphorylation compared to healthy tissues.

Because of tumor cells' increased and accelerated glucose uptake, ^{18}F-FDG is a highly sensitive tumor marker for the detection of many different types of cancer, including those of the lung, breast, colorectal, and gastrointestinal tracts.

- ^{18}F-NaF

Metastatic disease is highly prevalent in various solid tumors, with a significant risk of skeletal metastases. To target the skeletal system, osteotropic radiopharmaceuticals are utilized. These agents have an affinity for bone tissue and are commonly employed in clinical practice. Sodium-18 fluoride (^{18}F-NaF) is one of the most extensively used radiopharmaceuticals, particularly in PET imaging. It is important to note that radiopharmaceuticals themselves do not possess osteoblastic activity. Instead, they exhibit bone-seeking properties, enabling the detection of skeletal abnormalities associated with metastatic diseases. Among PET radiopharmaceuticals, ^{18}F-NaF holds a prominent position in clinical use for bone imaging applications[21].

- ^{18}F-CHOLINE

Fluorocholine is an imaging radiotracer composed of methylcholine tagged with the positron-emitting radioisotope fluorine ^{18}F (^{18}F-FMCH). Choline is a substrate for the production of phosphatidylcholine, the most essential phospholipid in the cell membrane. Choline absorption is mediated by choline kinase, which functions as a specialized transporter and whose expression is more prominent in prostate cells with prostate cancer. Due to the high incidence of prostate cancer and the low efficacy of ^{18}F-FDG in the research of this illness, fluorocholine is envisioned as a possible alternative, despite the lack of sufficient evidence to support its use in diagnosis or therapeutic management [22].

- ^{18}F-PSMA

^{18}F-PSMA (Prostate-Specific Membrane Antigen) is a radiopharmaceutical used in the imaging of prostate cancer. Prostate cancer is one of the most common cancers in men, and accurate imaging is crucial for diagnosis, staging, and treatment planning. The PSMA molecule is highly expressed in

prostate cancer cells, including both primary tumors and metastatic lesions. This characteristic makes PSMA an excellent target for molecular imaging using positron emission tomography (PET). ^{18}F-PSMA is a PET radiotracer that consists of a PSMA-targeting molecule linked to the radioactive isotope ^{18}F. The combination of the PSMA-targeting molecule and ^{18}F allows for the specific binding of the radiotracer to PSMA-expressing prostate cancer cells. ^{18}F-PSMA PET/CT has shown promising results in various clinical scenarios, including initial staging, restaging after treatment, and evaluating the response to therapy. It has the potential to detect small lesions, including lymph node and bone metastases, which may not be adequately visualized by conventional imaging modalities.

1.9 Automatic Radiopharmaceutical Dose Dispenser

As we discussed previously, Radiopharmaceuticals labeled with radionuclides like ^{99m}Tc, ^{18}F, ^{11}C, ^{68}Ga are commonly used in diagnostic nuclear medicine to image and/or assess the global or localized function of an organ or tumor [23][24]. Finding a suitable balance between the administered activity and the image quality required for a proper diagnosis is a major challenge in diagnostic nuclear medicine [25][26][23]. quantitation in imaging is another important issue in nuclear medicine which refers to the accurate measurement and quantification of the radiotracer distribution in the patient's body during imaging studies. It involves determining the activity concentration of the radiotracer in specific regions of interest or organs. quantitation plays a crucial role in obtaining reliable and meaningful diagnostic information. It allows for the assessment of various parameters such as organ function, blood flow, metabolic activity, and receptor expression levels. Quantitative measurements help in distinguishing between normal and abnormal tissue uptake, evaluating treatment response, and monitoring disease progression. Accurate quantitation requires precise measurement of the administered activity of the radiotracer, as well as calibration of the imaging equipment to account for factors such as attenuation and scatter of radiation. It is essential to achieve a suitable balance between the administered activity and the desired image quality to ensure accurate quantitation. Failure to accurately measure and dose the radiopharmaceutical can lead to incorrect or unreliable quantitative results. If the administered activity is too high, it can

result in excessive radiation exposure for the patient. Conversely, if the activity is too low, it can lead to poor image quality and compromised diagnostic accuracy. Staff radiation safety is another important consideration in nuclear medicine [27][26].

Syringe shields [28] and dose-dispensing systems are just a few examples of the many devices developed to reduce radiation exposure to the hand. Manual injectors available on the market are made to limit the amount of time fingers are exposed to radioactive substances during the injection process. In the last decade, industries have been researching possible solutions to reduce the subjectivity and inaccuracies associated with the manual approach, while optimizing radiation protection. Recent advancements in industrial automation and control engineering have sparked fresh interest in the use of automatic syringe/vial calibration methods and other automatic dose-dispensing systems in nuclear medicine, particularly for positron emission tomography (PET) [23].

Programmable Logic Controllers (PLCs) are the heart of an automated system. They have the ability to process digital and analog input signals before delivering output signals to and from the linked device, with the option of being configured to function in response to a feedback signal (for instance, the stroke end signal of a syringe). The PLC structure is created in accordance with the process that will be automated; it is physically located outside the cell and connected there by signal cables. It typically has tiny, compact dimensions, and it may operate in hot, humid environments. The PLC, if properly programmed, can direct a sequence of operations involving certain components of the device connected to it, all according to a chosen timing and with the possibility of being able to interrupt the sequence at any time, by intervening in remote-controlled mode. An automatic module is a device capable of automatically carrying out a very precise sequence of physicochemical operations and movements, necessary for the preparation and / or dispensing of a radiopharmaceutical preparation. In each of them two components can always be distinguished: one mechanical and one chemical. The mechanical part includes electrical and / or pneumatic elements, linear and / or circular actuators, power supplies, pumps, cooling / heating systems, sensors for monitoring various parameters (such as temperature, pressure, range, flow, radioactivity) and any other physical devices not in direct contact with chemicals. The chemical component, on the other hand, consists of

an interconnected network of containers, tubes, syringes, valves and filters, through which the solid, liquid or gaseous reagents can be handled, mixed, collected or transformed in order to obtain the desired final product to be dispensed. The contact between the physical and chemical part can be permanent or temporary. Clearly, each component that comes into contact with the reagents must be chemically inert and not release impurities during its entire use. The same module can be suitable for carrying out the synthesis / dispensing of different radiopharmaceuticals, thanks to the creation of different paths for the passage of fluids and to a sufficient number of valves and reactors. Each automatic module is associated with a control system aimed at governing and regulating its operation, equipped with a graphical interface in order to allow the operator to interact with the module itself and monitor the progress of the process in real time. A special software governs the control system and is usually provided by the module manufacturer, in a form that cannot be altered by the operator who will use the device. The software is usually module-specific but not necessarily process-specific, and is able to start the execution of a list of instructions (process-specific sequence, not modifiable by the operator) in order to implement all the steps necessary for the preparation / dispensing of a radiopharmaceutical. All the most important process parameters and data are stored on the hard disk and then used for the creation of a final report, containing all the details of the procedure carried out. The software is designed in such a way as to minimize the intervention of the operators, thereby minimizing the risk of errors, and to carry out the processes in compliance with the pharmaceutical conditions required by the legislation. Figure 1.9 and Figure 1.10 illustrate two types of radiopharmaceutical fractionators in vial and syringe respectively.

Figure 1.9: CRP-Compact: An automatic dose dispenser in vials made by Tema sinergie

Figure 1.10: KARL100: An automatic dose dispenser in syringes made by Tema sinergie

Chapter 2

Multichannel Analyzer Characterization for Radioisotope Monitoring

2.1 State of the Art

Positron Emission Tomography (PET) is a molecular imaging technology that in the last 25 years has gained an increasing role in diagnosis of a variety of pathological conditions, especially in oncology[2]. The radionuclides used for PET imaging have extremely short half-lives and are produced ideally on-site using cyclotron accelerators with specialized radiochemistry laboratories. In most cases, radioactive effluent materials in the form of gas and liquid can be produced as a result of various reactions during the production cycle [29]. One factor that poses a concern to the public's health is the release of radioactive waste into the environment. Therefore, in accordance with international technical reports, recommendations, and rules, they must be reduced to pre-determined standard level [30]. Several methods, including the use of filters, containment and storage tanks, and delay lines, have been employed in this context over time [31]. However, these techniques do not provide a means to gather either quantitative or qualitative data. It is important to note that while filters or containment systems alone do not serve as radiation meters, they can be considered "quantitative" if they enable the complete removal of effluent. Some of these systems may include a radiation

measuring instrument, such as containment systems, which can be used to trigger the operation of the system. It is advisable to measure the potential presence of radioactivity in effluents and demonstrate compliance with regulations, as required. Hence, continuous monitoring systems are needed for the waste material analysis, radioisotopes recognition and activity evaluation of contaminated liquids (for waste management systems) and potentially contaminated air coming from building ventilation systems. Several strategies, including gamma spectroscopy with HPGe and NaI(Tl) detectors, Geiger-Müller (GM), proportional counters, plastic scintillation detectors and etc have been used for continuous radionuclide monitoring over the years. HPGe (High Purity Germanium) and NaI(Tl) detectors have been commonly used for continuous radionuclide monitoring. Each of these detector types has its own benefits and drawbacks. In recent years, HPGe detectors have gained recognition as the gold standard for radionuclide identification and activity quantitation due to their superior energy resolution compared to NaI(Tl) detectors. However, because of their high price, the requirement to cool the detector to liquid nitrogen temperatures, and their fragility, HPGe detectors have been utilized less frequently. These systems with germanium detectors are typically deployed in remote locations and connect to a sampling system that facilitate sampling and measurement polling between different work areas and the point of release. It should be noted that these systems are not truly continuous meters. When comparing NaI(Tl) to HPGe for radioisotope monitoring applications, the efficiency of the detectors themselves may be the most crucial factor. For a given detector size, NaI(Tl) is more efficient overall and absorbs more gamma rays than HPGe because of its higher effective Z [32]. Therefore, a NaI(Tl) scintillation detector working in tandem with a Multi-Channel Analyzer (MCA) typically plays a key role [33][34][35]. In reality, Multi-Channel Analyzers (MCAs) for radioisotopes are frequently employed in laboratories and on the market to analyze sources and samples with a lengthy analytical window. The MCA system comprises of an Analog to Digital Converter (ADC), a Graphical User Interface(GUI) module, and a data acquisition, processing, and storage unit. In order to identify the nuclide in a nuclear spectroscopy system, MCA scans the entire energy range of radionuclides, counts the number of pulses for each energy, and stores the data at a designated location.

In this approach, Tema sinergie company has developed different prod-

ucts for gas and liquid radioactive waste monitoring all equipped with a NaI(Tl) scintillation detector coupled with a MCA called ORTEC Digibase. In the following we introduce these systems:

E-STACK M System

E-STACK M stand for Environmental Stack Monitoring. In this system the whole probe positioned in the air extraction ducts of laboratories [36]: such sensors detect the concentration of radioactive isotopes in the air before it is extracted to the outside. Figure 2.1 shows one of the system's installation on top roof of a nuclear medicine center.

E-RAS M System

E-RAS-M stand for Environmental Room Air Sample Monitoring for contaminated air coming from the building ventilation systems. In this approach the probe placed in a Marinelli beaker as indicated in Figure 2.2. Contaminated air from different rooms are flown to a Marinelli beaker and the activity of presented radioisotopes is measured.

Waste Management System

Aqueous wastes containing short lived beta/gamma activity are kept in storage. After decay to exclusion limit, they have been checked using a NaI(Tl) scintillation detector coupled with a Multi-Channel Analyzer (MCA). This detector system is usually installed in the monitoring systems based on Marinelli beaker geometry as shown in Figure 2.3. If these wastes meet the regulatory requirements on chemical and biological hazards they can be safely discharged into the environment. Aqueous wastes that have higher radioactivity content and/or long lived radionuclides may be treated using ion exchange/sorption, chemical precipitation, and/or evaporation, reverses osmosis, filtration and solvent extraction.

The main issue with this approach is that the probe itself, which is designed to stay in a controlled LAB room temperature, is affected by changing environmental parameters such as temperature and relative humidity; additionally, the analysis software provided with the MCB typically does not take these particular conditions into account, which could jeopardize the probe's calibration setup with the result of losing the possibility to recognize isotopes,

Figure 2.1: Installation of E-STACK-M system for airborn radioactive waste monitoring.

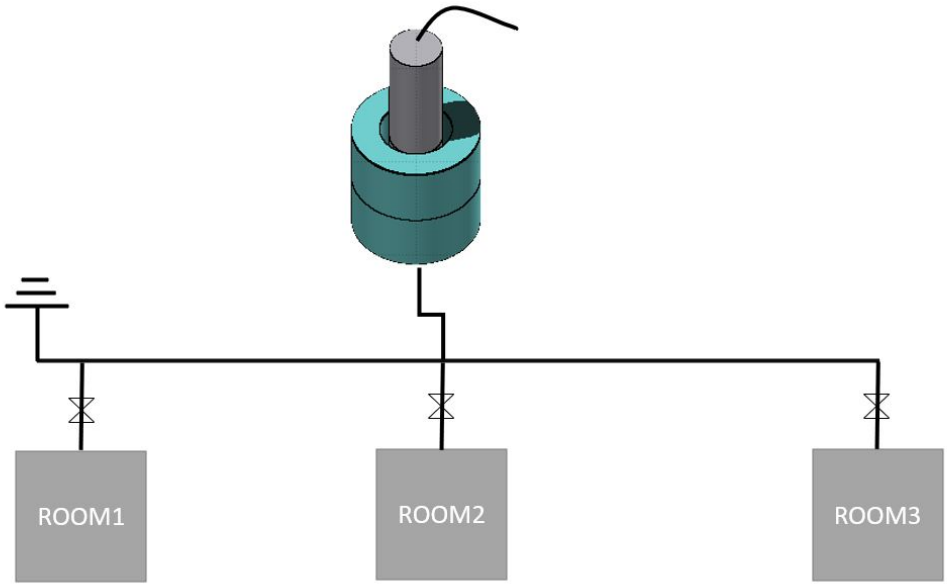

Figure 2.2: E-RAS-M

even if recently calibrated. This is known as "channel drifting," and it is really problematic. Therefore, having an MCA capable of monitoring radioisotopes via a self-stabilization strategy could fix the problem. On the other hand, the activity of radioactive material as an essential parameter can be investigated following an appropriate calculation procedure of calibration factors corresponding to each radionuclide by extrapolating the detection efficiencies of the monitoring systems[29][37]. This is a problematic issue in case of airborne radioactive material since the efficiency calibration of these monitoring systems can be affected by a large number of uncertainties, or in some cases, due to the source-detector geometry, the efficiency calibration of the system is difficult and inefficient experimentally[38]. Monte Carlo (MC) simulations are nowadays widely employed for such problems to extract a proper estimate of the detection efficiency before installing novel devices with innovative designs in the real environment[39]. Since the introduction of different systematic deviations also originate from the intrinsic efficiency of the sensitive material used in the probe or the signal processing in the electronics which cannot be simulated by the applied MC models, a cross-calibration of the monitoring system using a suitable radioactive air sample inside a controlled

Figure 2.3: Installation of waste management system for liquid radioactive waste monitoring.

chamber like a Marinelli beaker can make the calibration more reliable.

2.2 Project Goals

Our goal in the first section of this thesis is the final characterization and calibration of the MCA designed by Georadis company (Brno, Czech Republic) in close collaboration with Tema Sinergie company (Faenza, Italy) in the context of SPEKTRO project. The MCA is coupled with a 2″ ×2″ NaI(Tl)detector which can be adopted as a substitute in MCA-based systems which explained in the previous section. First and foremost, we must assess the dependability and stability of the SPEKTRO probe under a variety of temperature and relative humidity conditions, and compare it to the ORTEC probe. In this scenario, we can be certain of the developed auto-stabilization method, and if the SPEKTRO probe works well, we must carry out efficiency calibration for the SPEKTRO probe in various geometries for the aforementioned applications and compare with Monte Carlo simulations.

2.3 Instrument Description

In this project we have considered two NaI(Tl) scintillation detector with two different multichannel analyzer (MCA):

1. A Scionix-Saint Gobain 2″ ×2″ NaI(Tl) scintillation crystal, 14-Pin PMT coupled with an MCB AMETEK-ORTEC DigiBase for the purpose of gamma Spectroscopy as shown in Figure 2.4. Digibase unit contains a miniaturized preamplifier, detector high voltage (0 to +1200 V bias) with powerful digital signal processing, multichannel analyzer, and special features for fine time resolution measurements all contained in a low-power (<500 mA) socket. Gamma vision software (ORTEC) was used for data acquisition. This probe was considered as a reference probe for the purpose of comparison[40].

Figure 2.4: Ortec probe: NaI(Tl) detector coupled with a multichannel analyzer(MCA).

2. A Scionix-Saint Gobain 2″ × 2″ cylindrical NaI(Tl) crystal, 14-Pin PMT from ORTEC, coupled with a gamma spectrometer called SPEKTRO shown in Figure 2.5 having a resolution of 8.5% at 661 keV was used in this study. The corresponding software GeoMon was used for data acquisition. The MCA and its dedicated software were developed in a close collaboration of Georadis Company and Tema Sinergie Company.

2.4 Developed MCA Description

In the following we discuss different functionalities of the developed gamma spectrometer called SPEKTRO. The entire gamma detector is connected to the PC via ethernet cable and the output can be seen through a graphical user interface called GEOMON software. The gamma spectrometer consists of two parts: 1) Field Programmable Gate Array (FPGA) based spectrometer. 2) CPU board. All the signal processing, including pulse shaping, peak-detection, and pile-up rejection, are performed on the FPGA part. The CPU takes care of spectrum evaluation, stabilization processing and communication tasks. Detector high voltage is between 400V-1000V, and gain is between 0.5-2.0. Below we will discuss different modules implemented inside SPEKTRO for

Figure 2.5: SPEKTRO probe: NaI(Tl) detector coupled with a multichannel analyzer(MCA) contained in the red unit.

radioisotope recognition and activity evaluation.

2.4.1 Radioisotope Identification

The peak search algorithm is based on finding any potential of local peak through first and second derivative method and saving them as a preliminary location of the peaks in the measured spectra. Each inflection point is then observed from left and right to identify foots of a potential peak and nonlinear background. All the preliminary values are then used as input parameters for fitting procedure of a gaussian function. A fitted gaussian curve is then checked for resolution and other criteria to eliminate any spikes and accept only true peaks. Finally, there is the table of found peaks, their position in the energy scale and their amplitude. On the other hand, there is a nuclide library implemented inside the spectrometer with a maximum of 200

nuclides. So, the method consists in going through the nuclide library and try to get a match between any combination of nuclide in the library against the table of found peaks. As a results we get: name of the nuclide, amplitude of each peak and net area.

2.4.2 Radioactivity Evaluation

There are two methods for evaluation of the radionuclide's activities in SPEKTRO unit.

2.4.2.1 Estimative Method

The estimative method is the classical determination of activities from area of peaks and known peak efficiency curve and a yield of identified nuclide. This way of activity evaluation is very common but problem arises when we deal with low activities, because in this case it is tricky to compute the nonlinear background below a peak correctly. So, for SPEKTRO probe applications, this method is only used as complementary and for estimation.

2.4.2.2 Assay Method

The assay method is the second mode of activity evaluation and it is based on calibration of the detector chain (detector, beaker and shielding) for known specific elements and on using the least square interpolation of measured spectra to known spectra of standards. SPEKTRO allows to specify nine predefined methods for assay calibration, each with different nuclides, activity units, calibrations, measurement time etc. This is the most sensitive and accurate method.

2.4.3 Stabilization Algorithm

The gain of the NaI detector, which determines the energy-to-channel conversion, can be stabilized using the gamma rays emitted by naturally occurring radioisotopes. There is an auto gain stabilization algorithm implemented inside SPEKTRO. This algorithm uses ^{40}K (1461 keV), ^{214}Bi (1764 keV), ^{208}Tl (2614 kev) and ^{137}Cs (661.7 Kev) to adjust the fine and course gain. There is

a backstage spectrum acquisition which usually takes for 20s or 30s to evaluate the presence of the peaks. So if no peaks are found, the measurement is extended for other 30s as long as it gets the list of the peaks in any position. The ratio of positions of two peaks in the gamma spectrum is a fixed ratio regardless of the actual gain. So, a matrix of all the peaks and their ratios is created. According to this matrix, the position of found peaks can be refined by changing the fine and course gain.

2.5 Energy Calibration

Energy calibration was performed for both ORTEC and SPEKTRO probes to find a relation between the energies and the channel numbers. In case of the ORTEC probe, several radioisotopes such as ^{241}Am, ^{137}Cs and ^{60}Co were placed in front of the detector inside a 6 cm lead shielding. The gamma spectra were acquired for 10 minutes using Gamma Vision software as can be seen in the following Figure 2.6, Figure 2.7, Figure 2.8. The results of energy calibration are plotted in Figure 2.9.

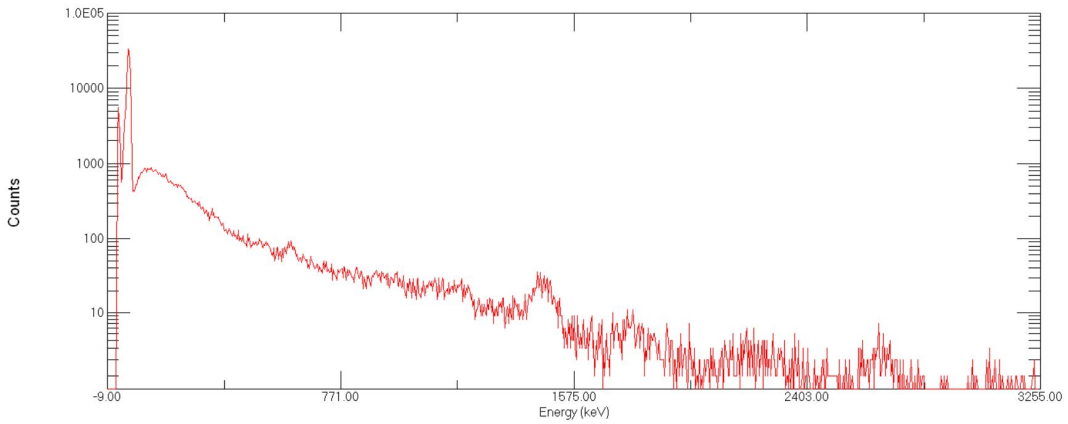

Figure 2.6: ^{241}Am gamma spectrum for energy calibration

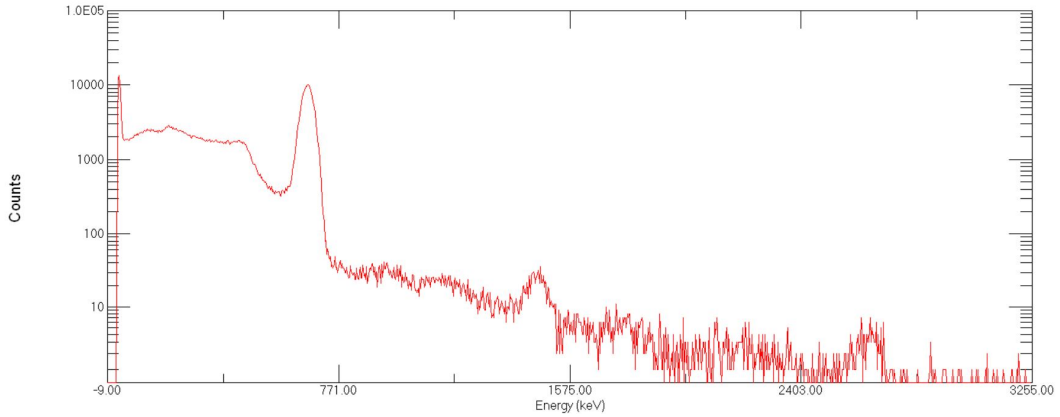

Figure 2.7: ^{137}Cs gamma spectrum for energy calibration

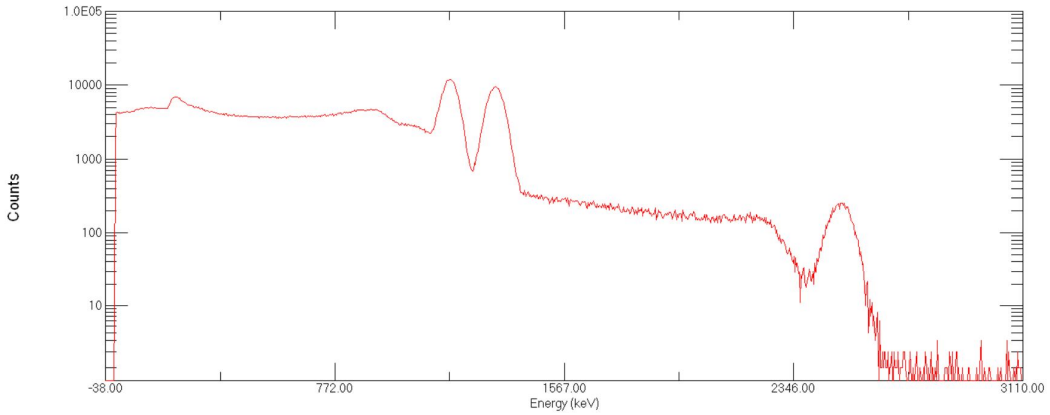

Figure 2.8: ^{60}Co gamma spectrum for energy calibration

Energy linearization of the SPEKTRO probe was done by accessing to the gppcon software installed on the Unix computer coupled with the spectrometer. The sources used for energy linearization (listed in Table 2.1) were placed in front of the detector inside a 6cm lead shielding and their gamma spectra were acquired for 10 minutes.

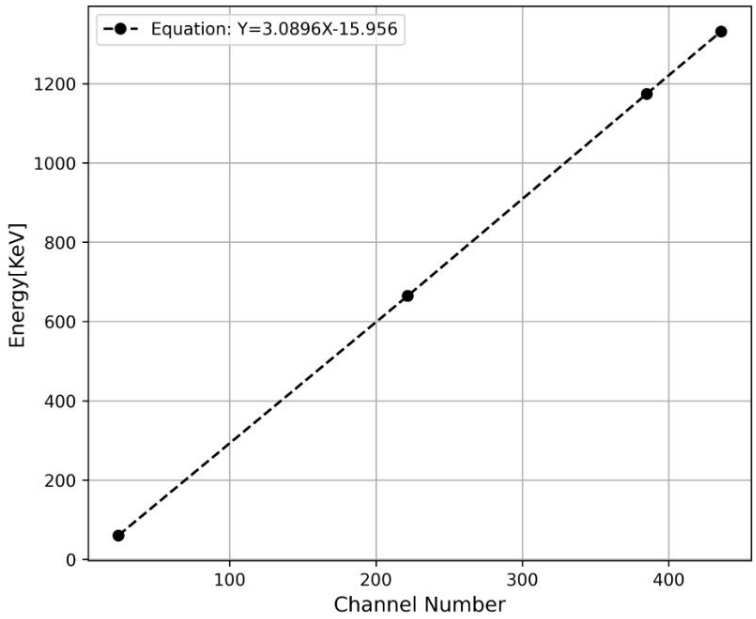

Figure 2.9: Energy calibration of ORTEC probe: Y(=energy[keV]) versus X(=channels)

Table 2.1: radioisotopes used for energy calibration of SPEKTRO probe

Source	Half life [Y]	Energy [keV]
^{241}Am	432.2	59
^{133}Ba	10.51	356
^{137}Cs	30.07	662
^{60}Co	5.2714	1174
^{60}Co	5.2714	1332
^{232}Th	1.405E10	2614

The acquired spectra are presented in the following figures Figure 2.10, Figure 2.11, Figure 2.12. The results are plotted in Figure 2.13. From this calibration the consequent relation obtained to convert channels in energy in keV:

$$Y = 2.9998X + 0.0326 \tag{2.1}$$

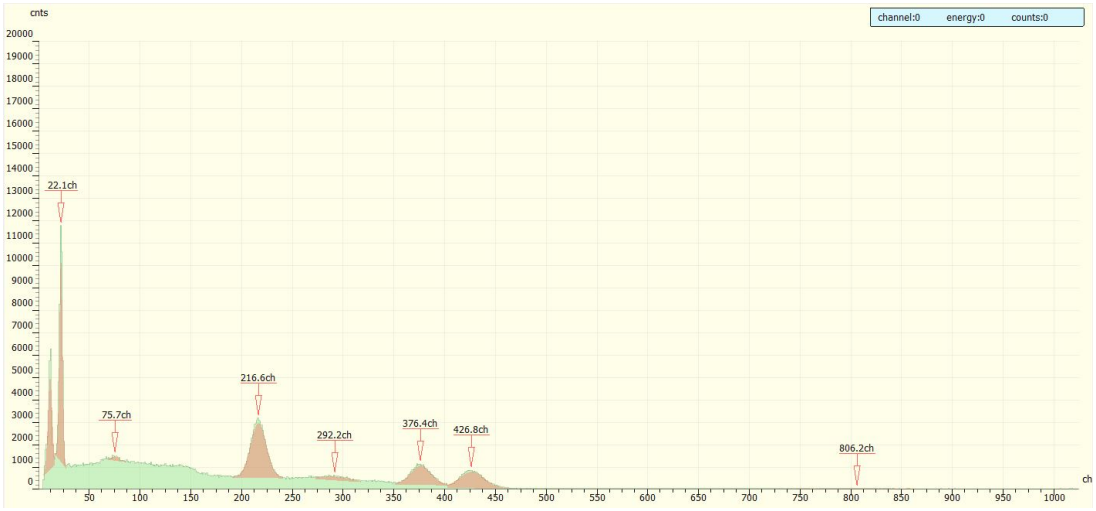

Figure 2.10: ^{241}Am + ^{137}Cs + ^{60}Co gamma spectrum for energy linearization

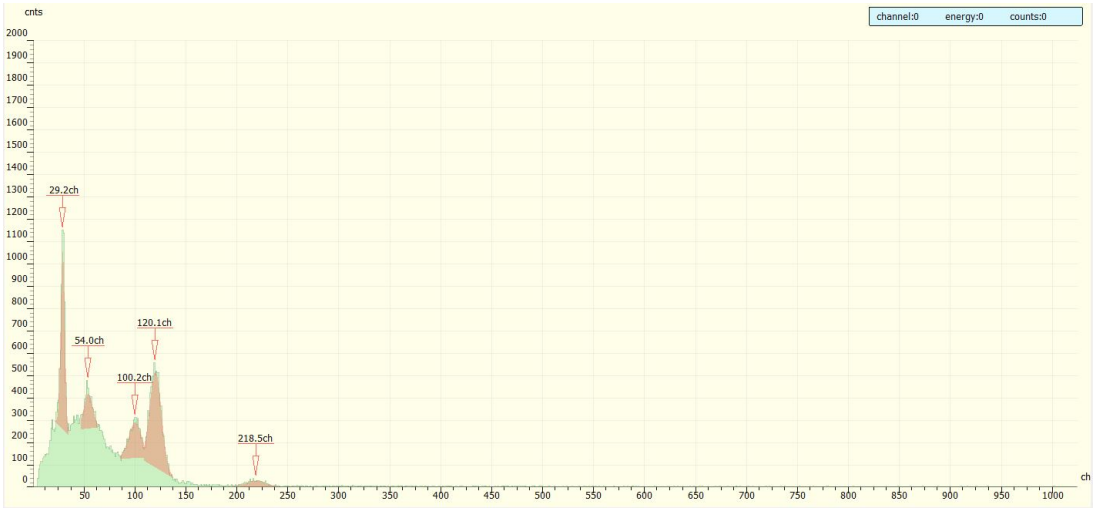

Figure 2.11: ^{133}Ba gamma spectrum for energy linearization

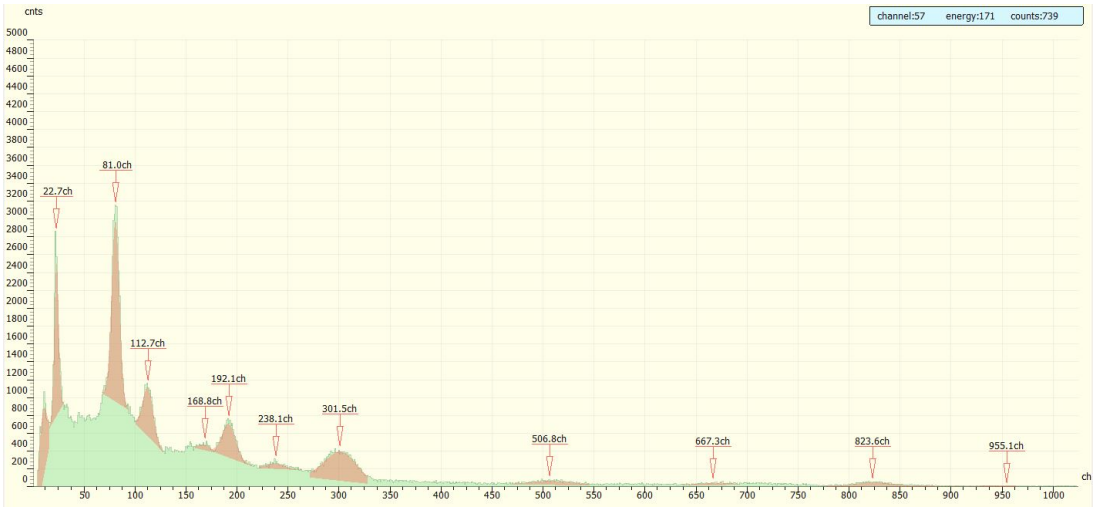

Figure 2.12: ^{232}Th gamma spectrum for energy linearization

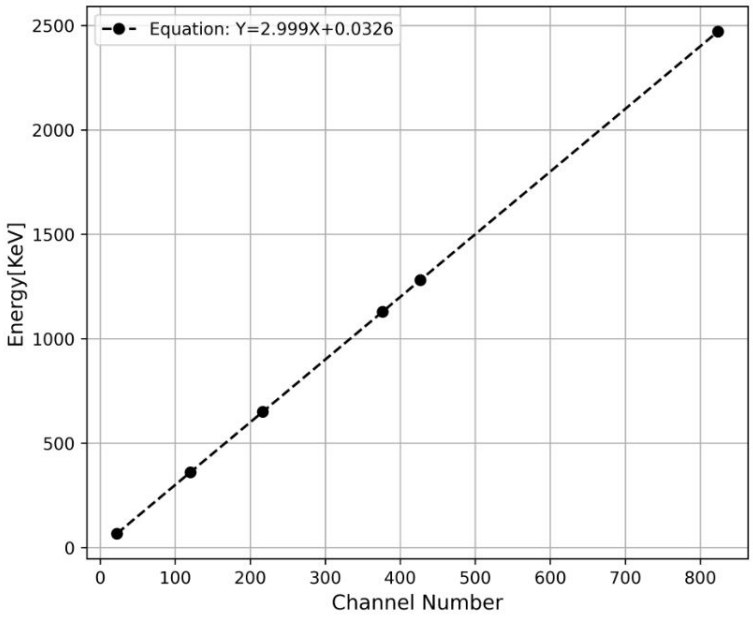

Figure 2.13: Energy calibration of SPEKTRO probe: Y(=energy[keV] versus X(=channels)

2.6 Efficiency Calibration

The efficiency of a detector quantifies its capability of detecting particles. It is composed of two separate parts:

1) Geometrical efficiency is the fraction of the source radiation which is geometrically intercepted by the detector and thus it depends entirely on the geometrical configuration of the source-detector system. Ω represents the solid angle (in steradian) by the detector at the source position:

$$\epsilon_{geom} = \frac{eventsimpingingondetector}{eventsemittedbythesource} = \frac{\Omega}{4\pi} \tag{2.2}$$

$$\Omega = \int_A \frac{\cos(\alpha)}{r^2} dA \tag{2.3}$$

in which A is the detector surface that faces the source, dA is the surface element, α is the angle between the normal to the surface element dA and the source direction and r is the distance between the source and the surface element dA.

2) Intrinsic efficiency depends on the interaction cross section of the incident radiation on the detector medium, and it is thus a function of the type of radiation, its energy and the detector material.

$$\epsilon_{int} = \frac{eventsregistered}{eventsimpingingondetector} \tag{2.4}$$

Total efficiency is given by:

$$\epsilon_{tot} = \epsilon_{geom}.\epsilon_{int} = \frac{eventsregistered}{eventsemittedbythesource} \tag{2.5}$$

To obtain the total efficiency in this study is to integrate the counts in the full energy peak of each gamma line (within $H_0 \pm 3\sigma$), and this represents the number of events registered, and then divide this value for the number of photons emitted by the corresponding source in the run live-time, which can be calculated from its certified activity and date of production.

$$\epsilon = \frac{N(E)}{t \times P(E) \times A} \Pi C_i \tag{2.6}$$

Where N(E), t, P(E), A, and C_i are the number of counts in the full energy peak supplied by the software, the measuring time, the photon emission probability at energy E, the activity, and the applied correction factors C_i for deadtime and radioactive decay, respectively. Two decay correction factors were considered for the peak efficiency evaluation; one is related to the source decay from the reference time to the run time, the other is related to the decay during the acquisition procedure. Equation 2.7 shows the decay correction where λ is the decay constant, t is the detector live time, Δt is the time interval between reference time and run time.

$$C_d = \frac{\lambda t}{1 - e^{-\lambda t}} \times e^{\lambda t} \tag{2.7}$$

The uncertainty in the full energy peak was evaluated by Equation 2.8 :

$$\sigma_\epsilon = \epsilon.((\partial\epsilon/\partial A)^2.\sigma_A^2 + (\partial\epsilon/\partial P)^2.\sigma_P^2 + (\partial\epsilon/\partial N)^2.\sigma_N^2)^{1/2} \tag{2.8}$$

Where σ_A, σ_P, σ_N are the uncertainties of the associated A, P(E), and N, respectively.

Therefore, for the activity evaluation, the detector efficiency calibration must be performed for each geometry. As we mentioned earlier, SPEKTRO probe is supposed to be used for building stack monitoring for radioactive waste gas monitoring and in radioactive waste management systems for radioactive waste liquid monitoring.

2.7 Environmental Effects on Detector

As previously stated, the purpose of this research is to develop a stable gamma detection system for use in radioactive waste management systems, which are typically situated on the top roofs of nuclear reactors or underground, where ambient temperature and relative humidity vary significantly. So, in this investigation, we looked at how the SPEKTRO and ORTEC probes behaved at different temperatures and relative humidity levels. The tests were conducted in a well-shielded climate room, which provided optimum circumstances and a measuring environment.The chamber temperature and relative humidity varied from 5 to 50 °C with steps of 5 °C and 30% to 90% with the steps of 10%, respectively. A thermometer was also used to double check the chamber condition as shown in Figure 2.14. To ensure proper

thermal equilibrium, all measurements at a given temperature and relative humidity were done after 2 hours of holding time. The results were collected using a ^{137}Cs radioactive source that emits gamma rays at 662 keV. Both detectors were energy calibrated at 25 °C as room temperature, with Cs photopeak position serving as the control. The experiment was repeated three times in the same circumstances to test the results validity, and the standard deviation was calculated.

Figure 2.14: Climatic chamber

2.7.1 Temperature Effect on the ORTEC probe

Figure 2.15 illustrates the ^{137}Cs gamma spectrum acquired by ORTEC probe in different temperatures and Figure 2.16 shows the photopeak position of ^{137}Cs versus temperature. As can be observed, increasing the temperature from 25°C up to 50°C moves the ^{137}Cs photopeak position to the left, decreasing the temperature from 25°C to 15 °C shifts the photopeak position to

the right and from 15°C to 5 °C the trend appears flat.

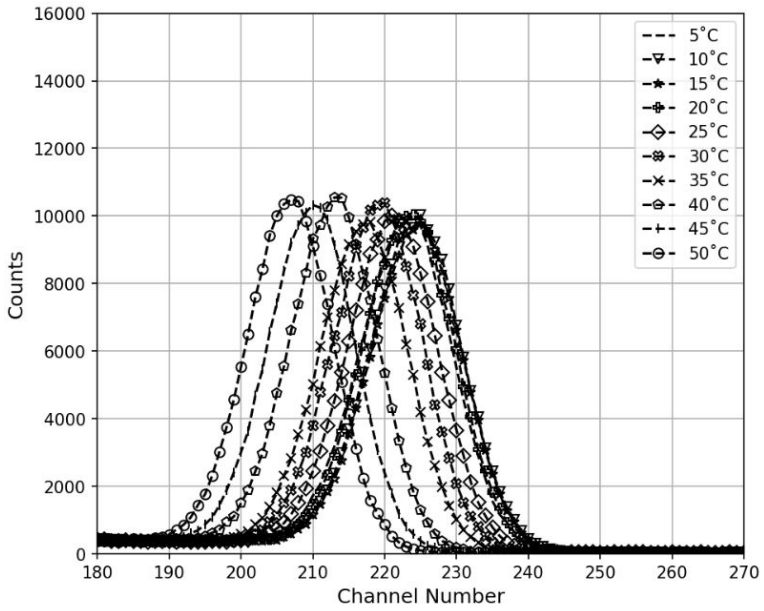

Figure 2.15: ^{137}Cs gamma spectrum acquired by ORTEC probe in different temperatures: Y(=Counts) versus X(=Channel number)

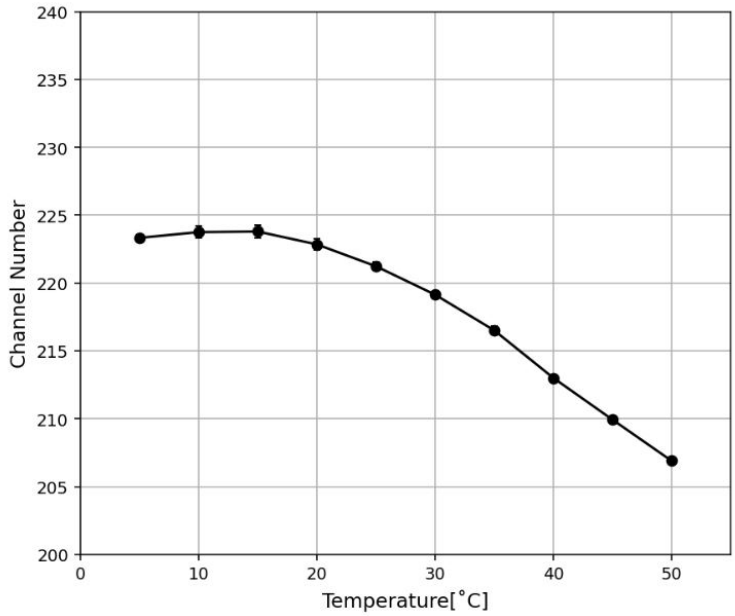

Figure 2.16: Effect of temperature on ^{137}Cs photopeak position obtained by ORTEC probe: Y(=Channel number) versus X(=Temperature [°C])

Table 2.2: ^{137}Cs photopeak position at different temperature obtained by ORTEC probe

Temperature [°C]	Channel number (1)	Channel number (2)	Channel number (3)	Average	SD
5	223.08	223.62	223.29	223.33	0.22
10	223.49	223.38	224.39	223.75	0.45
15	223.29	223.72	224.39	223.80	0.45
20	222.54	222.60	223.42	222.85	0.40
25	220.94	221.13	221.65	221.24	0.30
30	219.10	218.97	219.37	219.15	0.17
35	216.38	216.96	216.21	216.52	0.32
40	212.97	212.87	213.19	213.01	0.13
45	209.87	209.88	210.05	209.93	0.08
50	206.93	206.91	206.85	206.90	0.03

2.7.2 Temperature Effect on the SPEKTRO probe

Figure 2.17 illustrates the ^{137}Cs gamma spectrum acquired by SPEKTRO probe in different temperatures and Figure 2.18 shows the photopeak position of ^{137}Cs versus temperature. As can be seen, a negligible deviation of the channel numbers from the calibrated peak position versus temperature was observed, with an uncertainty of around one channel for the probe. This experiment shows that the stabilization algorithm implemented inside the SPEKTRO probe works correct and effective. This advantage of the SPEKTRO probe makes it suitable for radioactive waste management systems.

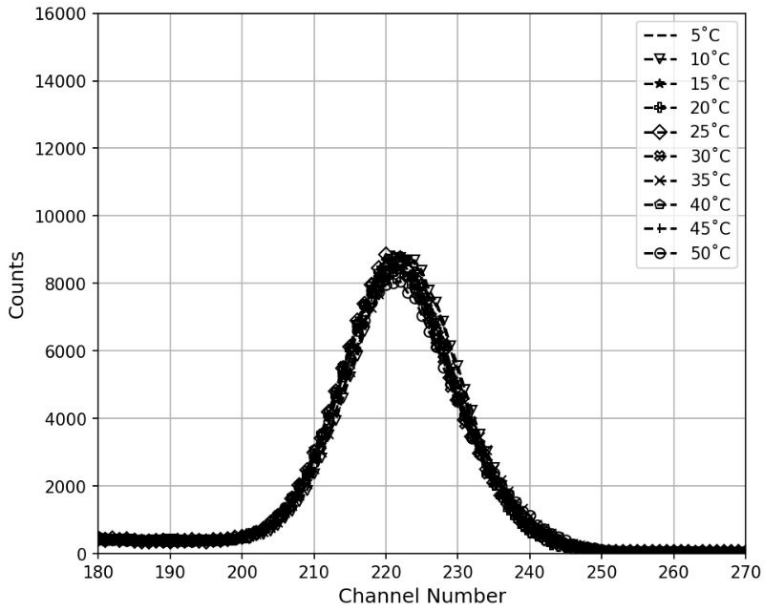

Figure 2.17: ^{137}Cs gamma spectrum acquired by SPEKTRO probe in different temperatures: Y(=Counts) versus X(=Channel number)

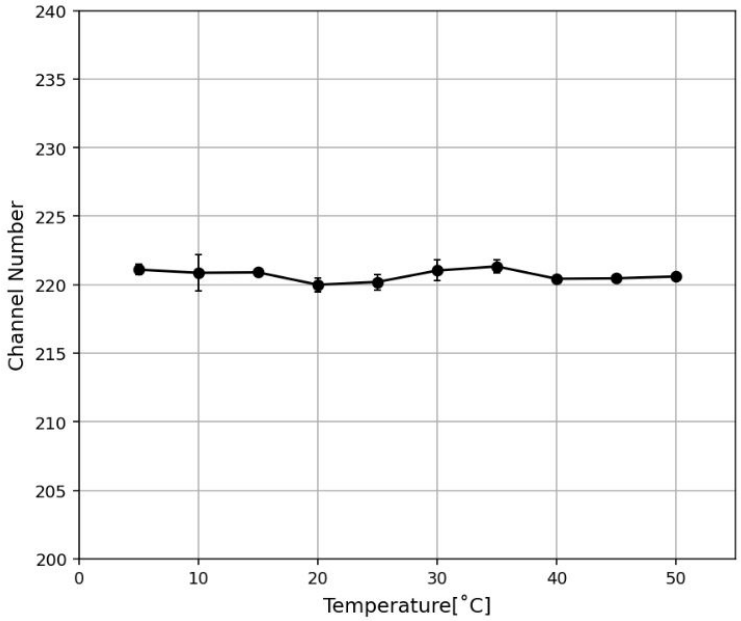

Figure 2.18: Effect of temperature on ^{137}Cs photopeak position obtained by SPEKTRO probe: Y(=Channel number) versus X(=Temperature [°C])

Table 2.3: ^{137}Cs photopeak position at different temperature obtained by SPEKTRO probe

Temperature [°C]	Channel number (1)	Channel number (2)	Channel number (3)	Average	SD
5	220.70	221.00	221.60	221.10	0.37
10	219.00	221.80	221.80	220.87	1.32
15	221.20	220.90	220.60	220.90	0.24
20	220.20	219.30	220.50	220.00	0.51
25	219.40	220.70	220.50	220.20	0.57
30	222.10	220.50	220.50	221.03	0.75
35	221.50	221.80	220.70	221.33	0.46
40	220.20	220.50	220.60	220.43	0.17
45	220.60	220.60	220.20	220.47	0.19
50	220.50	220.60	220.70	220.60	0.08

2.7.3 Relative Humidity Effect on SPEKTRO and ORTEC Probes

The effect of relative humidity on the behavior of both detectors was also investigated. Figure 2.19 and Figure 2.20 show the impact of the relative humidity changes from 30-90% on the gamma spectrum of ^{137}Cs obtained by the DigiBase and SPEKTRO probe, respectively. As can be seen, changing the relative humidity does not significantly affect the photopeak position of Cesium.

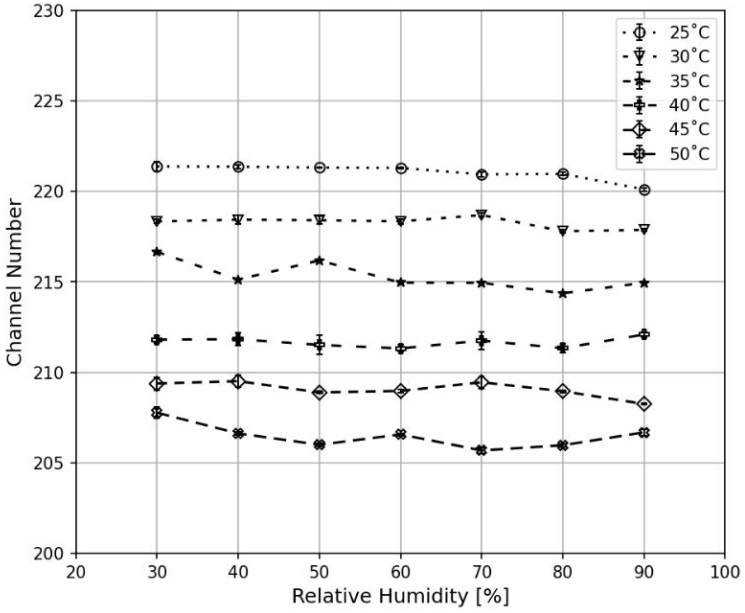

Figure 2.19: Effect of relative humidity on ^{137}Cs photopeak position obtained by ORTEC probe: Y(=Channel number) versus X(=relative humidity [%])

2.8 Monte Carlo Simulation

One of the primary goals of this thesis work has been to conduct a study dedicated to improving the efficiency calibration of NaI(Tl) detectors used for air density radioactive materials monitoring in geometries where experimental calibration is difficult or inefficient. The Monte Carlo (MC) method is a mathematical approach to modeling nature by directly simulating the essential dynamics of a given system. The Monte Carlo method is used in the scope

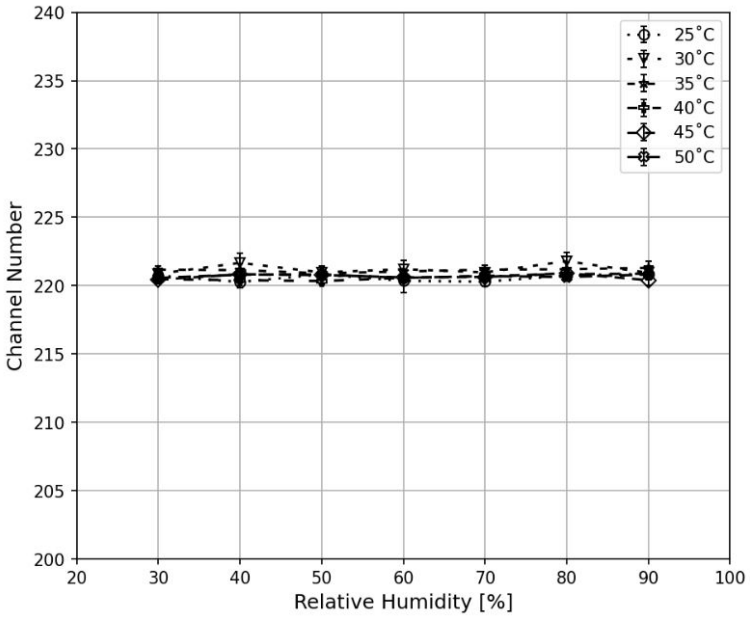

Figure 2.20: Effect of relative humidity on ^{137}Cs photopeak position obtained by SPEKTRO probe: Y(=Channel number versus X(=relative humidity [%])

of physics process studies, for example, to simulate a macroscopic system by simulating its microscopic components. The term Monte Carlo was coined in 1947, at the dawn of the computer age, by the scientists J.Von Neumann and S. Ulam, based on the production of random numbers and belonging to the so-called family of statistic and non-parametric methods[41][42].

To obtain a solution using the Monte Carlo method, three fundamental steps must be taken[43].

1. The production of a series of random numbers and the identification of the input variable based on the probability distribution that was selected;

2. The output parameter computation;

3. The loop on prior points and the comparison of the outcomes to determine the minimal value of the associated variance.

The randomness of the produced numbers is essential for the dependability of any Monte Carlo outcome. A calculator-generated number series is described as pseudo-random since there is a pre-established relationship between a sampled number and the previous one. The entire sequence is determined by the first number in the chain, known as the seed. Many simulation programs based on the Monte Carlo technique have been created and are used in a wide range of application sectors. A relevant class of them have been developed and widely disseminated expressly to allow simulation of particle interaction and propagation through matter. Table 2.4 lists some of the most common Monte Carlo algorithms, the particles they can handle, and the computer language used to create them.

Table 2.4: A list of the most often used Monte Carlo codes for particle tracking.

Code Name	Particle	Language
ETRAN/ITS	Protons, Electrons	Fortran
MCNP6	All paticles	Fortran
PENELOPE	Photons, Electrons	Fortran
PHITS	All paticles	Fortran
FLUKA	All particles	Fortran
GEANT4	All particles	C++

FLUKA is a well-validated Monte Carlo code with the main purpose of particle transport calculations and its possible interactions with matter. This code has been developed in FORTRAN by CERN (European Organization for Nuclear Research) and INFN (Italian National Institute for Nuclear Physics)[44]. Fluka reads user input from an ASCII file with the extension .inp. The input is made up of a variable number of "commands" (also known as "options"), each of which consists of one or more "lines" (sometimes known as "cards" for historical reasons).

A Fluka input file typically has the following structure:

✓ Titles and notes for documentation (optional, but recommended)

- ✓ A description of the problem's geometry (regions of space are divided into solid bodies and surfaces) (mandatory)
- ✓ The materials definition (mandatory unless pre-defined materials are used)
- ✓ Material responsibilities (correspondence material–region, mandatory)
- ✓ Description of particle sources (mandatory)
- ✓ Definition of the requested "detectors". The user needs to determine the anticipated value of a physical quantity, such as dosage, fluence, etc., for each of these phase space domains (regions of space, particle direction, and energy). There are several detector types that correspond to different quantities and the various estimators (algorithms) used to estimate them. Although detectors are optional, at least one is required, at least throughout the production stage.
- ✓ Definition of biasing schemes (optional)
- ✓ Definition of problem settings, such as energy cut-offs, step size, and physical effects that are not by default simulated, as well as particles that are not to be transported, etc (optional)
- ✓ Initializing of the random number sequence is necessary in order to estimate the statistical error.
- ✓ Start of signal and the quantity of histories requested (mandatory)

A Graphical User Interface called FLAIR has been developed to ease the editing of FLUKA input files, implement the code, and visualize the output files.

2.9 Efficiency Calibration of SPEKTRO Probe For Air Monitoring Systems: Marinelli Beaker

The evaluation of radiological conditions in areas that may potentially be contaminated with airborne radioactivity, such as hot laboratories, treatment

rooms for radionuclide therapies, and radioactive waste storage areas, is a critical aspect of the internal dose assessment program in nuclear medicine laboratories [45]. Airborne particulate samples collected using air pumping systems can be analyzed to determine their activity by measuring the sample's radioactivity within a Marinelli beaker geometry and determining the calibration parameters for each radionuclide. In nuclear medicine facilities, scintillating detectors housed inside Marinelli beakers are commonly used to measure the radioactive solutions in waste management systems. The activity of these solutions can be determined by counting the number of photoelectric interactions that occur in the detector during a set amount of time in the presence of monochromatic gamma rays that originate from the decay of gamma emitters or from the positron annihilation of β^+ emitters. Calibration of these devices is achieved by using reference water solutions with a known activity. However, accurate calibration for solutions containing several gamma emitters requires multiple precise calibrations because the interaction cross-section in the system components varies with the photon energy.

The calibration constants acquired with liquid solutions cannot be directly used to the measurement of the activity of gaseous samples because the substitution of a radioactive gas for the liquid solution creates a variation in the mass thickness of the sample. Monte Carlo simulation has been used successfully to compute the variance in detector efficiency in water and gas density samples.

2.9.1 Experimental Method

The radioactive standard sources with known activity have been prepared using ^{99m}Tc, ^{131}I, ^{137}Cs, ^{68}Ga, ^{60}Co radioisotopes in 1000 cm^3 water based Marinelli beaker geometry. The SPEKTRO probe was inserted in the center of the beaker. The system was surrounded by a lead shield as shown in Figure 2.21. The NaI(Tl) peak efficiency was calculated based on Equation 2.6 for full peak efficiency curve construction within the 140-1332.5 keV energy range.

Figure 2.21: Experimental setup for liquid waste management system calibration

2.9.2 MC Simulation Method

In this study, the FLUKA 4-2.0 CERN version and the FLAIR software version 3. 1-15.1 were used in the Ubuntu 20.04 LTS. A 2″ × 2″ cylindrical NaI(Tl) crystal, housed in Al was modeled. A SiO_2 layer is present at the end of the NaI(Tl) crystal for the contact with the photomultiplier tube to provide the real experimental conditions precisely. The above mentioned radioisotopes were distributed isotropically in Marinelli beaker with the same dimensions of the one used in the experiment (shown in Figure 2.22) once with water density and once with air density. The NaI(Tl) detector was simulated to detect the number of counts coming from the Marinelli Beaker source. To re-

duce statistical errors below 1%, 10^8 primary particles were run in six cycles. This simulation lasted for around 2 hours in a normal PC. The set of defaults called EM-CASCA was used for the simulation. Radioactive sources were defined as isotropic source in the BEAM card. The results were obtained by the DETECT card, enabling to score the energy deposition on an event-by-event basis. The DETECT card output gives a signal (event) spectrum, distributed over a fixed number of 1024 channels in the standard version. So, the correction coefficients to be applied to the measurement of radioactivity in air with Marinelli beaker for both gamma and beta+ emitters were investigated.

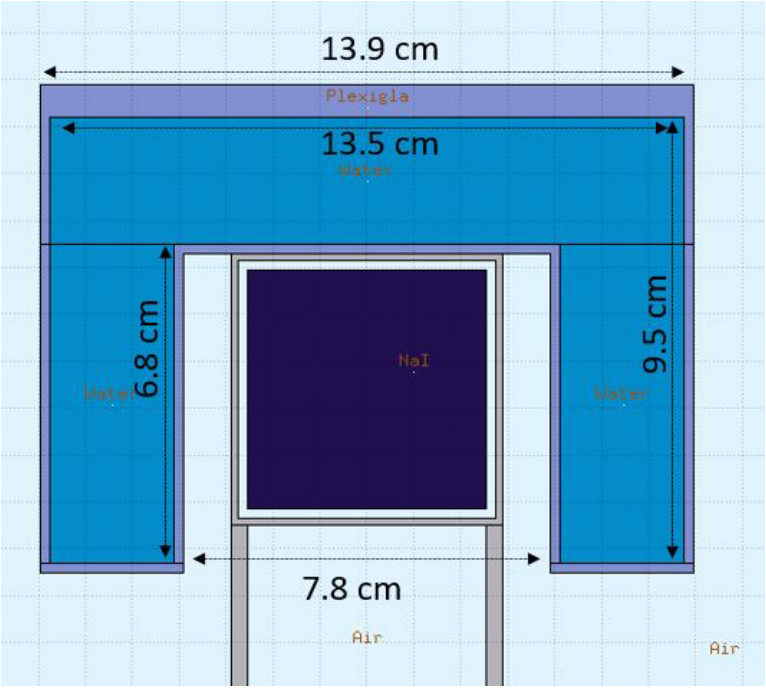

Figure 2.22: Marinelli beaker filled with water

2.9.3 Results

Table 2.5 illustrates the NaI(Tl) detector efficiency for each radioisotope in the form of gas and water density. The ratio of the efficiencies ($\epsilon_{airdensity}/\epsilon_{waterdensity}$) for each energy was applied to the experimentally determined detector efficiency. According to the data, it can be concluded that substituting air for water as the medium will boost photon interaction and detector efficiency.

Figure 2.23 depicts the full peak efficiency calibration results obtained from the experiment and simulations. When comparing the evaluated efficiency in water density, the difference between experiment and simulation is greater at low photon energies than at high photon energies. The reason for this is that it is impossible to model all of the features of the detector geometry as they are in reality, and the uncertainty in the final results can be more noticeable at low energies. As a correction factor, the ratio of detector efficiencies obtained in simulation for air and water density samples was applied to the experimental values. Finally, Equation 2.9 was used to find the best fitting function for the detector efficiency in case of air based Marinelli beaker source geometry. The coefficients were obtained using the least-squares fitting method.

$$ln\epsilon(E) = \Sigma_{i=0}^{n} a_i.(lnE)^i \tag{2.9}$$

Table 2.5: Relation of NaI(Tl) detector efficiency to the source density: ϵ_{av1} represents the detector efficiency for air density radioisotope in 1000 cm^3 Marinelli beaker and ϵ_{lv1} represents the detector efficiency for liquid density radioisotope in 1000 cm^3 Marinelli beaker

Radioisotope	ϵ_{av1}	ϵ_{lv1}	$\epsilon_{av1}/\epsilon_{lv1}$
^{99m}Tc (140 keV)	0.06272	0.0492	1.27
^{131}I (364 keV)	0.0353	0.029	1.21
^{137}Cs (662 keV)	0.018	0.015	1.2
^{68}Ga (1077 keV)	0.0119	0.0104	1.14
^{60}Co (1174 keV)	0.0094	0.0083	1.133
^{60}Co (1332 keV)	0.00817	0.0073	1.119

2.10 A New Approach: SPEKTRO Probe Efficiency Evaluation For ^{41}Ar

^{41}Ar(T1/2=109.34 m) which is mainly produced during the production of PET nuclides inside medical cyclotron facilities by the activation of air due to neutron flux based on the ^{40}Ar(n,γ)^{41}Ar reaction is an essential gaseous

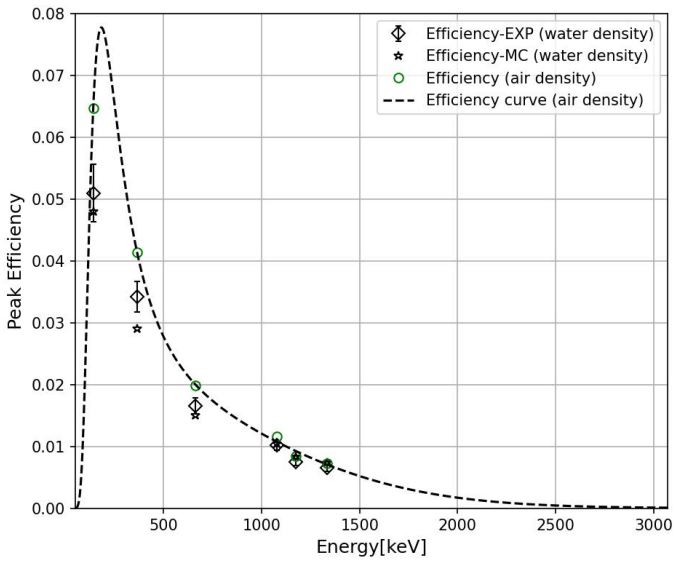

Figure 2.23: Full peak efficiency curve for liquid waste management system (1 Liter Marinelli beaker)

radionuclide that must be monitored regularly[46][47][48]. But the efficiency calibration of the stack monitoring system which is usually based on NaI(Tl) detectors is always problematic due to the source detector geometry which is either Marinelli beaker or duct shape. Monte Carlo (MC) simulations are nowadays widely employed for such problems to extract a proper estimate of the detection efficiency before installing novel devices with innovative designs in the real environment. On the other hand, since the introduction of different systematic deviations also originate from the intrinsic efficiency of the sensitive material used in the probe or the signal processing in the electronics which cannot be simulated by the applied MC models, a cross-calibration of the monitoring system using a suitable radioactive air sample inside a controlled chamber like a Marinelli beaker can make the calibration more reliable. In this investigation, the FLUKA code was used for simulating radioactivity monitoring systems based on a NaI(T1) detector regarding two different cases with the duct and the Marinelli beaker geometries. It must also be noted that these efficiencies for both systems were evaluated by

using ^{41}Ar radioactive gas. Moreover, an experimental efficiency calibration of SPEKTRO probe was performed by producing a ^{41}Ar calibration source in Marinelli beaker geometry with a given activity evaluated using a previously calibrated HPGe detector in the S. Orsola Malpighi cyclotron facility in Bologna, Italy. The evaluated peak efficiencies in experiment and simulation for Marinelli beaker geometry were compared. The ratio was considered a scaling factor for the final efficiency calibration of duct geometry for ^{41}Ar energy (1293.5 keV). Furthermore, Calibration factor (K) which correlates the number of CPS to the activity concentration (Bq/cm^3) by CPS/ Bq/cm^3 was evaluated for duct and Marinelli beaker geometries. The minimum detectable activity (MDA) value was estimated using the Currie method considering an acquisition time of 800 seconds according to Equation 2.10.

$$(2.71 + 4.65 \times \sqrt{B}) / (t \times k) \tag{2.10}$$

where B is the background counts for the specific energy and t and K are the time and calibration factor respectively.

2.10.1 Monte Carlo Method

The NaI(Tl) as explained in section 2.9.2 was simulated using FLUKA code. The NaI(Tl) detector was simulated to detect the number of counts coming from the duct and Marinelli Beaker source geometry, respectively. The set of defaults called EM-CASCA was used for the simulation. In both geometries, radioactive sources were defined as isotropic source in the BEAM card. The USERBIN card was used to see the distribution of radioactive source in both geometries. Results were obtained by the DETECT card, enabling to score the energy deposition on an event-by-event basis. The DETECT card output gives a signal (event) spectrum, distributed over a fixed number of 1024 channels in the standard version.

2.10.1.1 Duct Model

First, the stack monitoring system based on duct geometry designed by Tema Sinergie was simulated, as illustrated in Figure 2.25. The simulated shape in which the NaI(Tl) probe was put inside a cylindrical carbon fiber holder with 0.15 cm thickness and 40 cm height is shown in Figure 2.25. To decrease

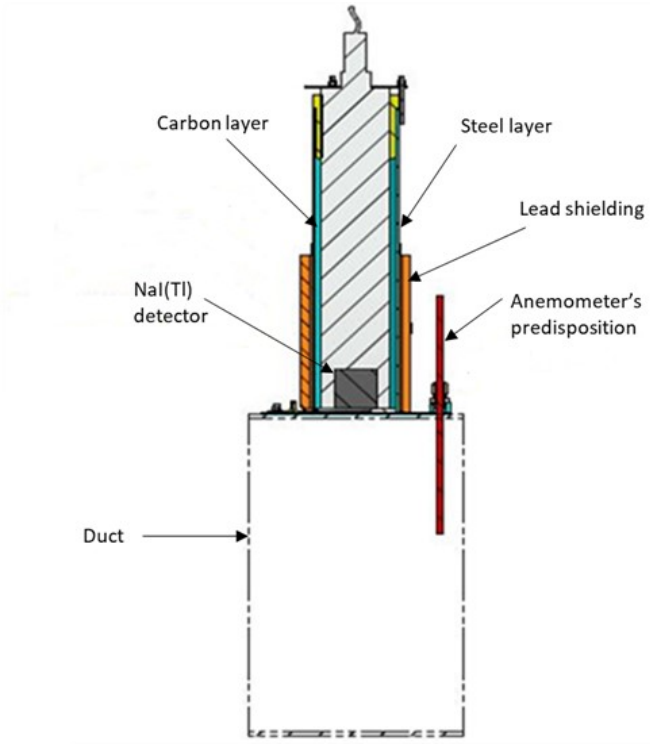

Figure 2.24: Schematic of stack monitoring system based on duct geometry. NaI(Tl) detector placed inside a holder made of two layers of Carbon and steel. A layer of lead was considered as shielding. The detector was mounted at half-height of the duct's outer surface.

background radiation, a 0.35 cm thick steel layer encircled the holder, and a 1 cm cylindrical lead shield was used. As an insulator, the area between the detector and the carbon holder was filled with neoprene material, which protected the probe from temperature changes. Finally, the probe was positioned halfway up the duct's outer surface. For the chimney, a simulated domain with dimensions of 40.64, 45.72, and 200 cm^3 and a thickness of 0.05 cm was examined. The effect of duct length on the calibration factor of the system was investigated at different duct lengths (50, 100, 200, 300, 400, 500, 600, 700, 800, and 900 cm).

USRBIN card was used as one of the scoring cards in FLUKA in order to show the ^{41}Ar photon flux distribution inside the duct chamber. As shown in Figure 2.26 , ^{41}Ar photon flux is distributed isotropically inside the cham-

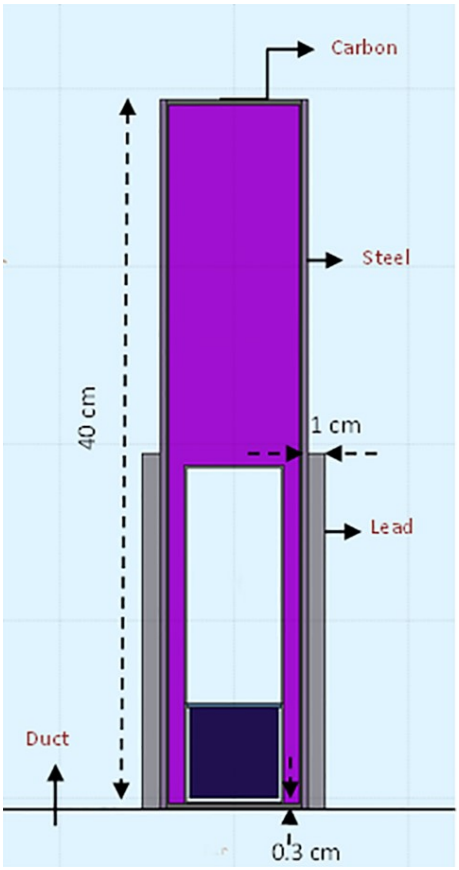

Figure 2.25: simulated stack monitoring system based on duct geometry. NaI(Tl) crystal covered with Al was placed inside a holder made of Carbon covered with a steel layer. The space between crystal and holder was filled with neoprene material as insulator. The lead layer was considered as shielding. The whole setup was fixed at half-height of the duct's outer surface. ^{41}Ar radioisotope was simulated isotopically inside the duct.

ber with air density. Figure 2.27 illustrates the number of counts generated inside the NaI(Tl) crystal depending on the energy, all the outputs in FLUKA are normalized to the number of primary particles. FLUKA code does not consider the physical processes needed for modelling the energy resolution. For our purpose it is enough to only consider the number of events detected at full energy peak. Based on the DETECT card results, the NaI(Tl) peak efficiency was calculated based on Equation 2.6. One of the uncertainties in

Monte Carlo simulations for peak efficiency is due to the statistical uncertainty of the number of counts per second in the full energy peak, which was calculated in this study. Finally, the NaI(Tl) detector peak efficiency for ^{41}Ar energy was calculated as $(1.15 \pm 0.01) \times 10^{-4}$.

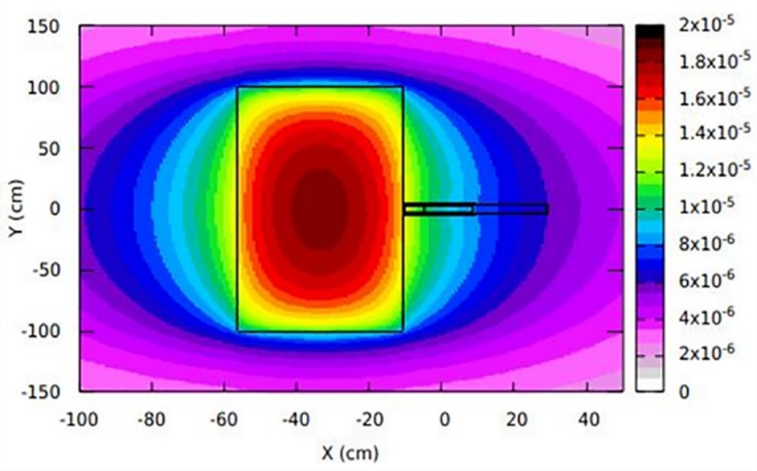

Figure 2.26: ^{41}Ar photon flux distribution inside the duct obtained by FLUKA. Photon flux distributed isotopically in duct.

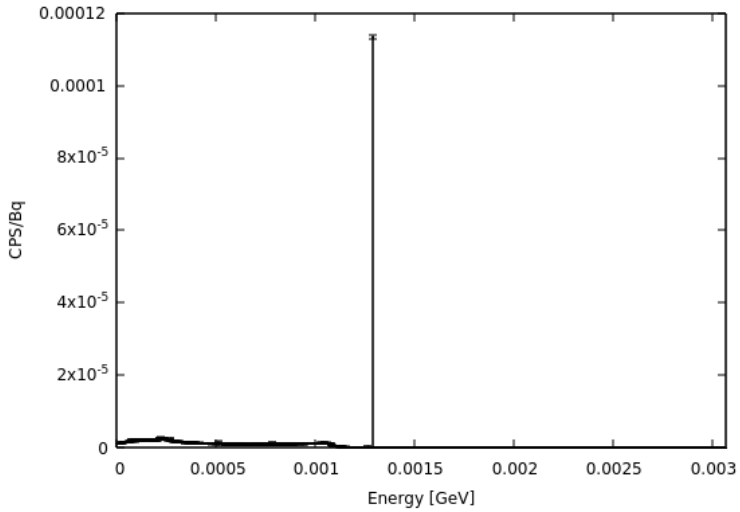

Figure 2.27: ^{41}Ar photopeak (1293.5 keV) obtained for duct geometry by FLUKA.

Moreover, the detector's detection efficiency (ϵ) and corresponding calibration factor (K) were evaluated for the ^{41}Ar gamma peak as a function of duct length with the constant square section and illustrated in Figure 2.28a and Figure 2.28b. Calibration factor (K) correlates the number of CPS to the activity concentration (Bq/cm^3) by CPS/ Bq/cm^3 which is usually of interest in radionuclide monitoring systems when dealing with activity concentration like exhaust monitoring systems. The error bars are small as points and cannot be seen from the graph. For the evaluation of the ϵ and K in this study, only the deposited counts under the ^{41}Ar full energy peak were considered. According to the plots, it is interesting to mention that after 300 cm, the calibration factor trend is approximately flat. This is because the detector efficiency for detecting the radioactive isotopes far from the detector surface is low. So, the effect of these nuclides on the evaluation of the calibration factors can be neglected compared to the nuclides decaying in the vicinity of the detector.

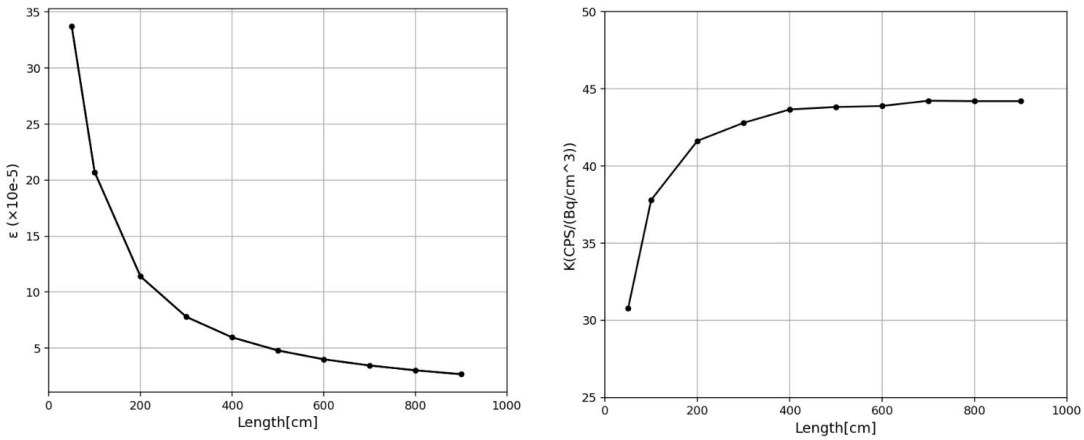

(a) Detection efficiency (b) Calibration factor

Figure 2.28: (a) ^{41}Ar photopeak efficiency for different duct length.(b) Calibration factor of stack monitoring system for different duct lengths.

2.10.1.2 Marinelli Beaker Model

In the next stage, a stack monitoring system based on Marinelli beaker geometry was modeled in which the same NaI(Tl) crystal covered with Al as duct geometry was placed inside the Marinelli beaker with the dedicated di-

mension indicated in Figure 2.29b. The space between the crystal and the Al cover was filled with 0.2 cm air. The SiO_2 material with the 0.3 cm thickness was considered to connect the crystal and Photo Multiplier Tube (PMT). The mentioned dimension of the system is related to the method used for the experimental efficiency calibration. The gamma peak efficiency of the NaI(Tl) detector was evaluated for the ^{41}Ar radionuclide in the Marinelli beaker geometry using FLUKA code. The photon flux is distributed isotropically inside the Marinelli beaker, as shown in Figure 2.30 . The number of the deposited gamma counts with 1293.5 keV energy in the sensitive part of the detector was registered using DETECT card. Figure 2.31 indicates the number of generated counts normalized to the number of primary particles per second. The photopeak efficiency was evaluated using Equation 2.6. and the results with the corresponding uncertainty is equal to $(7.6 \pm 0.028) \times 10^{-3}$.

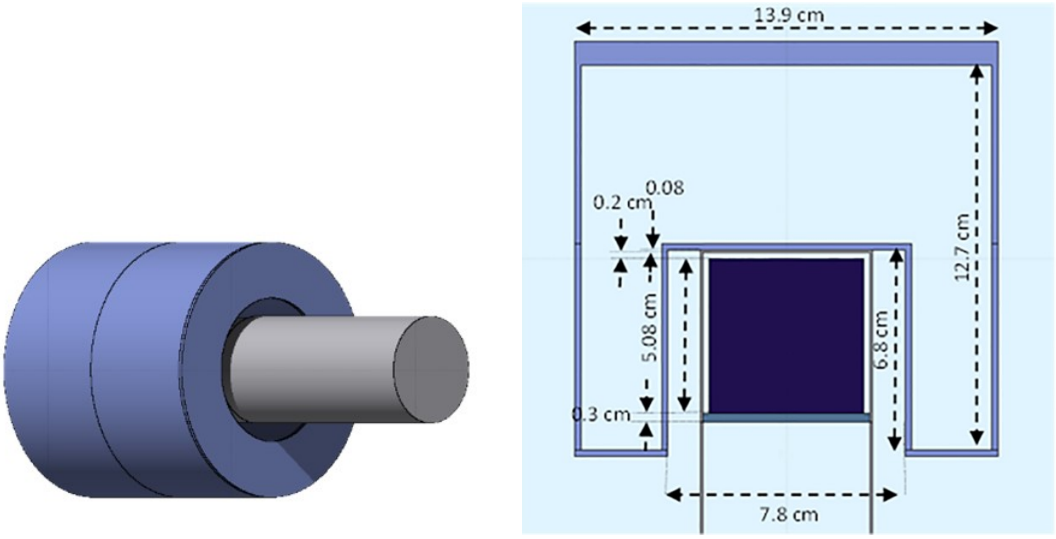

(a) 3D Schematic of stack monitoring system based on Marinelli beaker geometry

(b) 2D Schematic of stack monitoring system based on Marinelli beaker geometry

Figure 2.29: NaI(Tl) crystal covered with Al placed inside the Marinelli beaker.

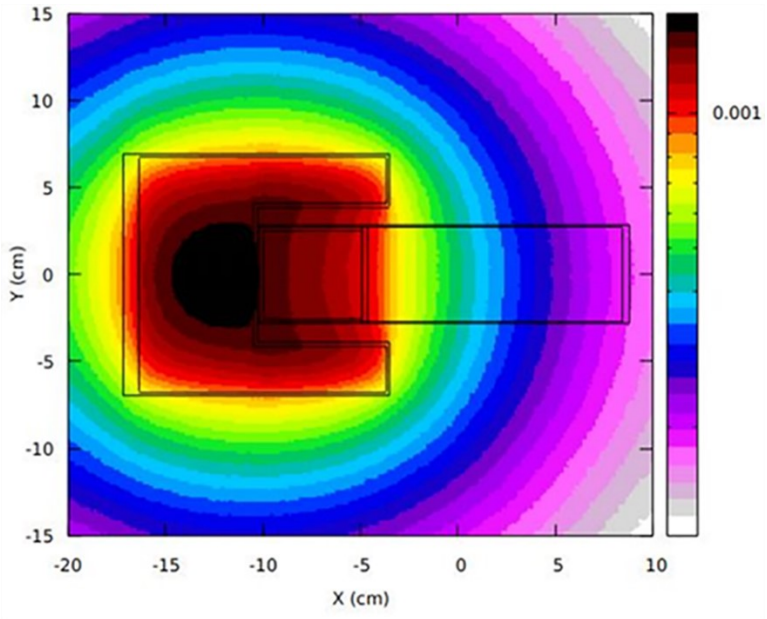

Figure 2.30: ^{41}Ar photon flux distribution inside the Marinelli beaker obtained by FLUKA. Photon flux distributed isotopically in Marinelli beaker.

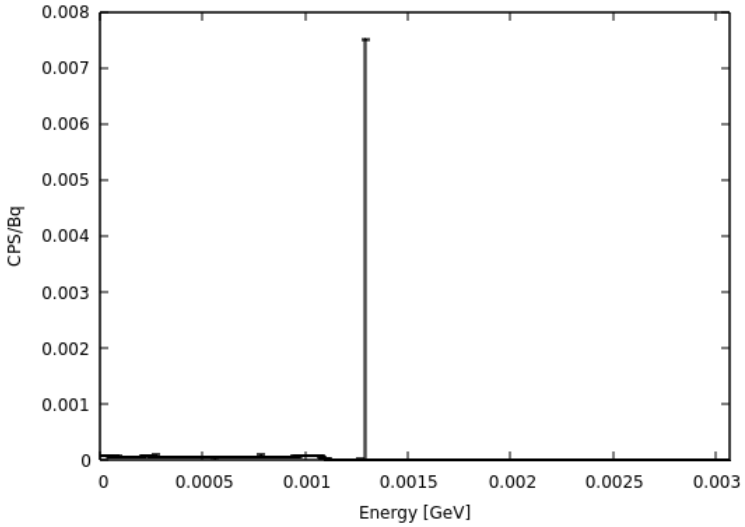

Figure 2.31: ^{41}Ar photopeak (1293.5 keV) obtained for Marinelli beaker geometry by FLUKA.

2.10.2 Experimental Method

The PET cyclotron facility in S. Orsola University Hospital in Bologna, Italy, was used to produce the ^{41}Ar radioactive standard source with specific activity based on neutron bombardment inside the dedicated Marinelli beaker. The activity of the produced ^{41}Ar was evaluated using an HPGe n-type detector. Therefore, the peak efficiency of the SPEKTRO probe for the ^{41}Ar calibration source was investigated experimentally.

2.10.2.1 PET Cyclotron Facility

The PETtrace (GE Medical System) cyclotron facility used for the purpose of ^{41}Ar production is shown in Figure 2.32. This is a compact cyclotron with a vertical acceleration plane that accelerates negative hydrogen and deuterium ions up to the energy levels of 16.5 and 8.4 MeV respectively. This particle accelerator is placed inside a bunker with dimensions of 650×535×350 cm with walls of 200 cm thickness. It is currently under operation at S. Orsola-Malpighi Hospital for the daily production of PET radionuclides

2.10.2.2 Production and Activity Measurement of ^{41}Ar using HPGe Detector

One of the most commonly used PET radionuclides is ^{18}F, which is manufactured on a daily basis at the S. Orsola Malpighi hospital cyclotron facility in Bologna. The target system is a [General Electric (GE) Medical System] assembly consisting of a niobium (Nb) chamber filled with [^{18}O]-water to generate ^{18}F via the (p,n) reaction. The fast neutrons are released from the target and start scattering and colliding with the bunker walls, resulting in thermal neutrons that are involved in the production of ^{41}Ar with a half-life of 109.34 minutes, according to the ^{40}Ar(n,γ)^{41}Ar reaction with the cross section of 673 mbarn [49]. Figure 2.33 illustrates the cross section of the ^{40}Ar(n,γ)^{41}Ar reaction as a function of incident neutron energy[46]. The Marinelli beaker of 1415.094 cm^3 volume shown in Figure 2.34 was filled with neutral argon and placed on top of a 1 meter stand inside the PET cyclotron bunker during the daily production of PET radioisotopes. After a specified decay time at the end of irradiation, the Marinelli beaker was transferred to the gamma spectrometry lab and the ^{41}Ar spectrum was acquired for 600 seconds using

Figure 2.32: PET cyclotron

a gamma spectroscopy system equipped with an HpGe n-type detector with a 30% relative efficiency and a resolution of 1.8 keV at 1332 keV. The spectrometry system was independently calibrated in the 59–1836 keV range by means of a multi-gamma certified reference solution, obtained from AREVA CERCA LEA, France in the shape of 1000 cm^3 Marinelli beaker. The calibration process was performed according to IEC 61452 standard using the Genie-2000 software [50]. A dual logarithmic polynomial efficiency curve was used. Finally, ^{41}Ar activity was evaluated for a reference time with the relative uncertainty of 7% at 1σ. Since the calibrated source was in liquid density and detector efficiency depends on sample density, FLUKA simulation was used to evaluate the difference in detection efficiencies between air and liquid density material for a series of radioisotopes in a wide energy range. The results of simulation can be seen in Table 2.6. According to the results the correspondent efficiency curve was evaluated and a correction factor for

efficiency, for the 1294 keV peak, was calculated and applied to water solution based efficiency calibration in the analysis of the experimental measurements.

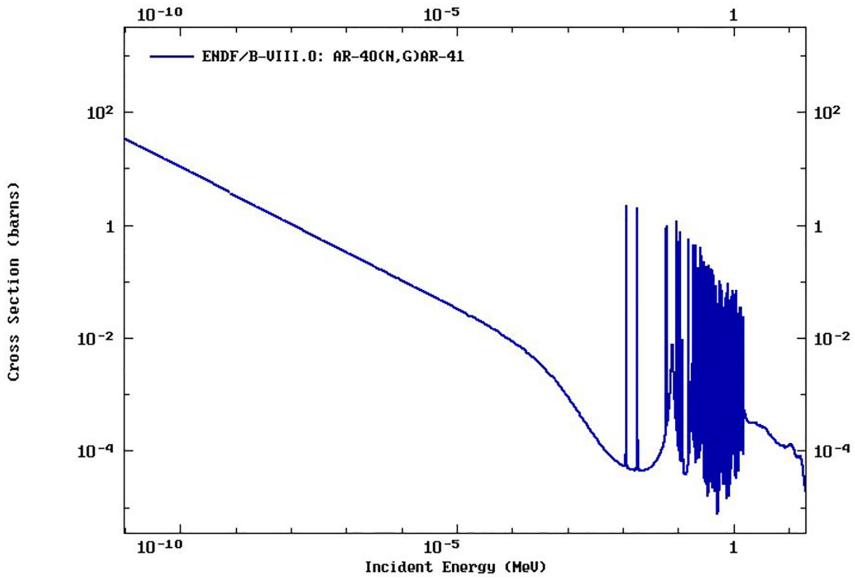

Figure 2.33: $^{40}Ar(n,\gamma)^{41}Ar$ reaction cross section[46]

Table 2.6: Relation of NaI(Tl) detector efficiency to the source volume and density: ϵ_{av1} represents the detector efficiency for air density radioisotope in 1000 cm^3 Marinelli beaker, ϵ_{av2} represents the detector efficiency for air density radioisotope in 1415.094 cm^3 Marinelli beaker and ϵ_{lv1} represents the detector efficiency for liquid density radioisotope in 1000 cm^3 Marinelli beaker

Radioisotope	ϵ_{av1}	ϵ_{av2}	ϵ_{lv1}	$\epsilon_{av2}/\epsilon_{lv1}$
^{99m}Tc (140 keV)	0.063±0.0003	0.054±0.0002	0.049±0.0002	1.10±0.007
^{131}I (364 keV)	0.035±0.0002	0.031±0.0002	0.029±0.0002	1.05±0.008
^{137}Cs (662 keV)	0.018±0.0001	0.015±0.0001	0.015±0.0001	1±0.01
^{60}Co (1174 keV)	0.009±0.0001	0.008±0.00009	0.008±0.00009	0.98±0.01
^{60}Co (1332 keV)	0.008±0.00009	0.0071±0.00008	0.0073±0.00008	0.97±0.01

Figure 2.34: stand for ^{41}Ar production inside cyclotron bunker with a Marinelli beaker mounted on top.

2.10.2.3 Efficiency Evaluation

Figure 2.35 shows the ^{41}Ar gamma spectrum with a photopeak at 1293.5 keV acquired by the SPEKTRO probe. The presence of a peak at 511 keV is most probably due to the production of a positron emitter radionuclide by activating the walls or the metal part of the beaker. For data analysis and evaluating the net area below the ^{41}Ar photopeak, a gaussian model developed using the macro language of CERN ROOT toolkit which is a framework for data processing developed at CERN was used. The nonlinear background was subtracted from the photopeak using a step function. Table 2.7 compares simulation and experiment in Marinelli beaker geometry which shows excellent agreement. The ratio between experiment and simulation was used as a scaling factor for the final efficiency calibration of the detector in the duct ge-

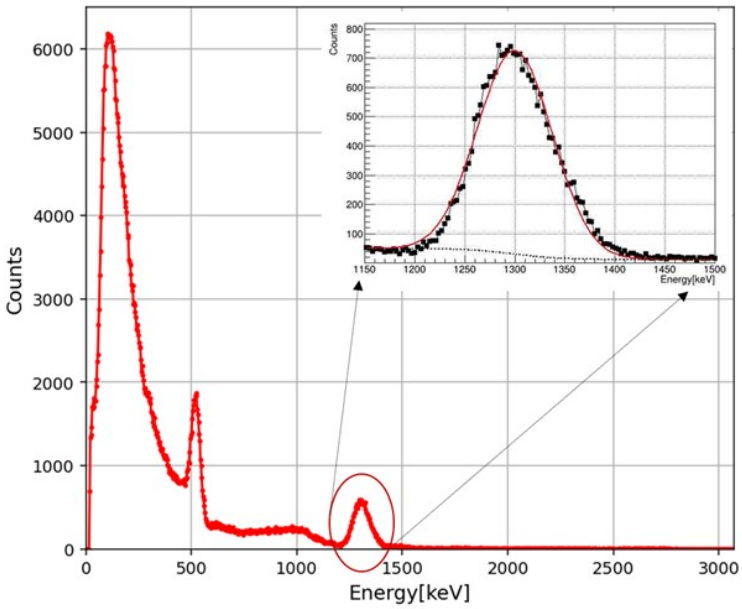

Figure 2.35: ^{41}Ar gamma spectrum obtained by SPEKTRO probe.

ometry and the final detector efficiency was evaluated as $(1.14 \pm 0.01)\times10^{-4}$. Table 2.8 shows the evaluated calibration factors and MDA for both duct and Marinelli beaker geometries.

Table 2.7: Efficiency Comparison Between Experiment and Simulation

Radioisotope	ϵ(Experiment)	ϵ(Simulation)	Ratio (Experiment/Simulation)
^{41}Ar (140 keV)	$(7.5\pm0.55)\times10^{-3}$	$(7.6\pm0.028)\times10^{-3}$	0.99 ± 0.07

Table 2.8: Evaluated calibration factor and MDA for duct and Marinelli beaker geometries

Radioisotope	Geometry	Energy range (KeV)	K (CPS/ Bq/cm^3)	Uncertainty	MDA(Bq/cm^3)
^{41}Ar	Marinelli beaker	1221-1425	10.75	0.04	0.014
^{41}Ar	Duct	1221-1425	41.63	2.08	0.0037

2.11 Efficiency Calibration of SPEKTRO Probe For Air Monitoring Systems: Ion Exchange Method

In this section a new method for producing a standard radioactive source with known activity in gas density was studied. In this approach a standard made of ^{241}Am, ^{137}Cs, ^{60}Co radioactive sources which are distributed in a Marinelli beaker with gas density, has been constructed using ion exchange technique. In this way, firstly, radionuclides with known activities were prepared in the liquid solution. Chemical materials called ion exchange resins (AMBERJET 1000 Na) were used to separate the radioisotopes from the solution (The assumption in this part is that the entire activity will be absorbed by the ion exchange resins). Consequently, these resins were adhered to fabric and placed in a Marinelli beaker leaving room for air as shown in Figure 2.36.

Figure 2.36: radioactive standard with gas density in Marinelli beaker geometry

Figure 2.37 illustrates the gamma spectrum acquired using the SPEKTRO probe. Detector efficiency was calculated for each energy and indicated in Figure 2.38. The same geometry was simulated using FLUKA code and the results was shown in the same graph. According to the results it is obvious that in low energies the deviation between experiment and simulation is higher compared to high energies, because at low energies the geometrical details play an important role in simulation and we can not simulate all the details.

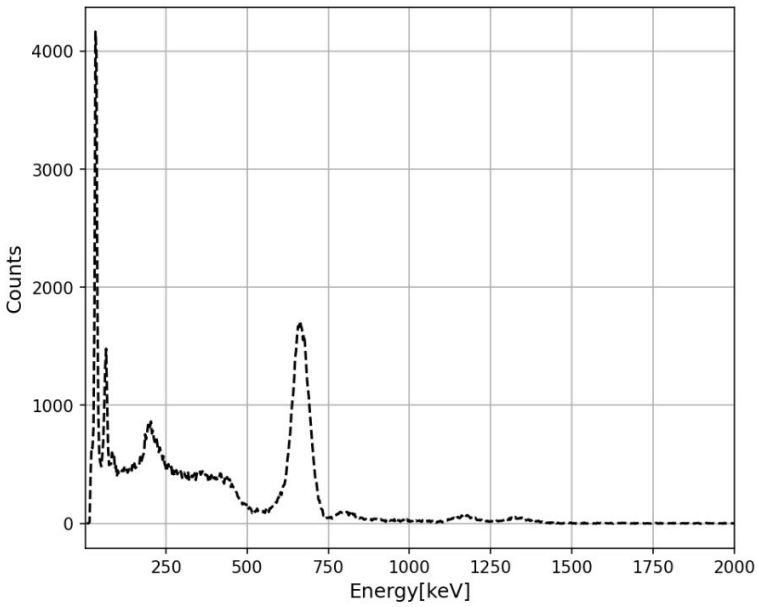

Figure 2.37: Gamma spectrum

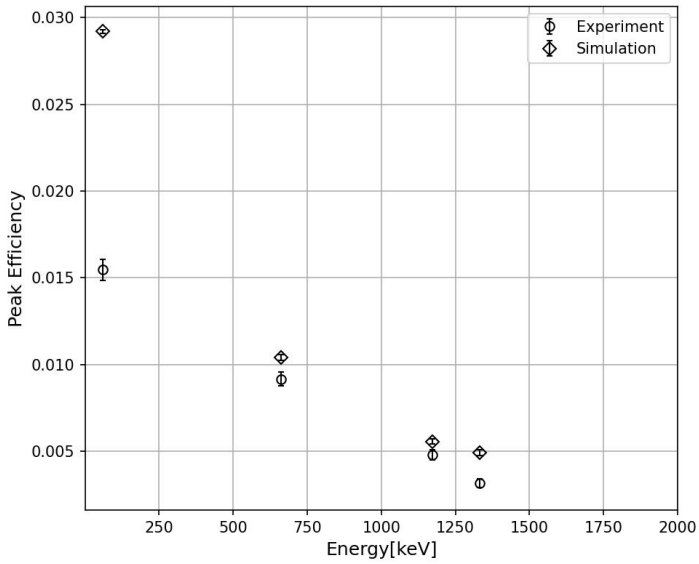

Figure 2.38: Efficiency calibration curve

2.12 Efficiency Calibration of SPEKTRO Probe For Waste management systems

The radioactive standard sources with known activity have been prepared using ^{99m}Tc, ^{131}I, ^{68}Ga radioisotopes in 2000 cm^3 Marinelli beaker which is the geometry used for waste management systems. The SPEKTRO probe was inserted in the center of the beaker. The system was surrounded by a lead shielding. The NaI(Tl) peak efficiency was calculated based on Equation 2.6 for full peak efficiency curve construction. The same geometry was simulated using FLUKA as shown in Figure 2.39, and the results were compared with the experiment. The full peak efficiency curve was evaluated within 140-1077 keV energy range and shown in Figure 2.40. Equation 2.9 was used to find the best fitting between the experimental and simulation points. The coefficients were obtained using the least-squares fitting method. According to the graph, a good agreement between experiment and simulation was obtained.

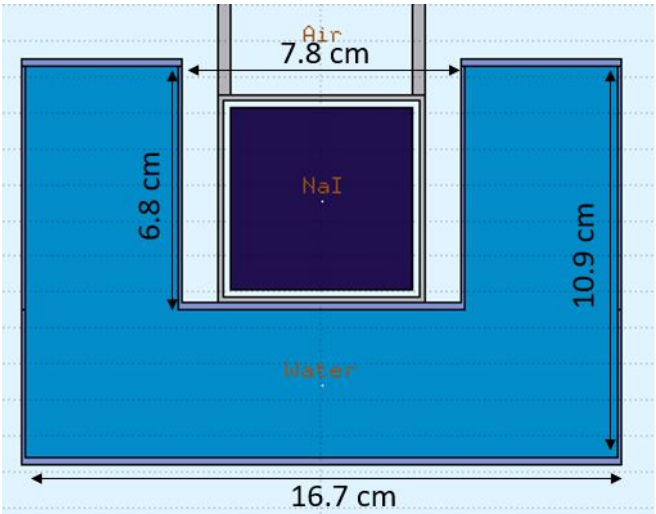

Figure 2.39: two liter Marinelli beaker filled with water

2.13 Radioactivity measurement

There are two methods for radioactivity measurement in SPEKTRO probe as discussed in 2.4.2. The calibration was performed by both methods and

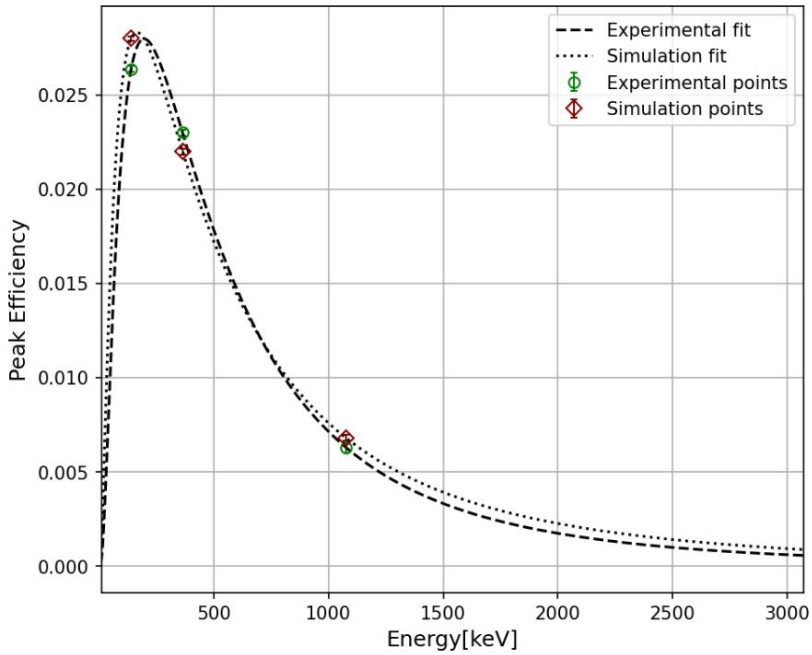

Figure 2.40: Full peak efficiency curve for liquid waste management system

the ^{131}I activity distributed in one liter water in Marinelli beaker geometry was evaluated. The evaluated activity using SPEKTRO probe was compared with the one obtained from HPGe detector and reported in Table 2.9. The measurements were repeated five times in different times. All the data were decay corrected for a reference time and the standard deviation from the average was calculated.

Table 2.9: ^{131}I activity measurement using two methods

Method	Activity [Bq]	Deviation(%)
HPGe	26244.62±1967.79	
Assay method	26837.07±75.47	-2.25
Estimative method	31244.024±2499.52	-19.05

As can be seen from the results of this measurements, assay method is more precise than estimative method and it is an advantage of the new MCA which can measure low activities with good precision.

2.14 Conclusion

NaI(Tl) detectors coupled with Multichannel Analyzer (MCA) are commonly used in radioactive waste management systems to measure the radioactivity of different types of radioactive waste. The calibration of these detectors is an essential step to ensure accurate and reliable measurements. In this chapter we have discussed the development and characterization of a MCA suitable to be used in radioactive waste management systems in nuclear medicine facilities. The MCA was coupled with a NaI(Tl) detector called SPEKTRO probe. The stability of the SPEKTRO probe was investigated in different temperatures and relative humidity conditions. To calibrate a NaI(Tl) detector, it is necessary to determine its response to known sources of radiation. This can be done by using a standard source of known activity, such as a calibrated radioactive source, and measuring the counts per second (cps) produced by the detector. The calibration process for these detectors typically involves the following steps:

1. Source preparation: A gamma-ray source with known activity and energy is selected for calibration.

2. Detector preparation: The detector is then shielded from external sources of radiation, and the detector electronics are set up to interface with the MCA.

3. Energy calibration: The gamma-ray source is placed in front of the NaI(Tl) detector, and the MCA is used to acquire the gamma-ray spectrum. The spectrum shows the number of gamma-ray counts versus energy. The peaks in the spectrum correspond to the gamma-ray energies emitted by the isotopes in the source. The energy calibration is performed by fitting a calibration curve to the gamma-ray peaks in the spectrum.

4. Efficiency calibration: The efficiency of the NaI(Tl) detector is dependent on the gamma-ray energy and the geometry of the source and detector. To calibrate the efficiency, a reference standard containing a known activity of the radioactive isotopes is used. The reference standard is placed in front of the detector, and the MCA is used to acquire the gamma-ray spectrum. The number of gamma-ray counts in the

spectrum is compared to the known activity of the reference standard, and the efficiency of the detector is determined for each gamma-ray energy.

Yet, in some instances, such as gas density radioactive waste monitoring systems, the calibration technique is challenging or fraught with a great deal of uncertainty. Various methodologies were utilized to calibrate the SPEKTRO probe's efficiency for activity measurements of gaseous radionuclides in geometries where direct experimental efficiency calibration is not achievable. In addition, a novel approach for evaluating the calibration factor for stack monitoring systems was proposed, which used MC simulation and a cross check with an experiment. The results demonstrate that the MC simulation is a useful tool for determining detector efficiency in complex geometries.

Chapter 3

Detector Development for an Automatic Dose Dispenser

3.1 State of the Art

The field of nuclear medicine has made extensive use of radioactive materials. In the past, nuclear medicine staff manually dispensed and diluted the radiopharmaceutical, which resulted in poor dispensing accuracy and reduced radiation protection[51]. Nowadays automatic injectors meet the needs in radiation protection and efficiency during preparation and injection of radiopharmaceuticals to the patients. $KARl_{100}$ is an automatic radioactive dose[1] dispenser employed to provide patients with exact fluorodeoxyglucose (FDG) doses for PET imaging. The machine is self-shielded by multiple tungsten panels differentiated according to working areas and activities. The maximum shielding, equivalent to 60 mm of lead, is above the volume which contains the daily activity. The $KARl_{100}$ system is designed to guarantee dispensing cycles in an aseptic environment as:

1. the sterilised activity at the entrance is received through an integrated filtering system (0.22 μm filter on the load line);

2. the connection/disconnection of infusers from the main distribution kit is automatic, and performed in a ventilated area (HEPA H14 filter) with

[1]The term "dose" in this chapter refers to pharmaceutical dose

controlled atmosphere, achieving class A air cleaning in the critical areas.

$KARl_{100}$ is a device capable of dividing a certain dose required by the operator and injecting it directly into a patient's venous circulation. It comes in the form of a very compact, shielded, easy to move trolley containing an autonomous injection unit in which a special syringe is placed and a dose calibrator responsible for radiopharmaceutical's activity evaluation. The operator is asked to insert the vial containing the radiopharmaceutical into the system and to choose between the "direct" infusion mode (connecting the device directly to the patient's infusion circuit) or "remote" (the dose is first divided into a syringe and then administration takes place by connecting the injection unit to the patient). The automatic Rad-inject infuser is equipped with 8.5 mm tungsten shielding, set to deliver the radiopharmaceutical in 1 min, while the stand for infusion is equipped with a further shielding of 21 mm tungsten.

In order to prepare an individual activity of ^{18}F-FDG, the technician links a new syringe to the Rad-inject and to the $KARl_{100}$ dispensing kit, then the automatic procedures can start. The patient administration takes place according to the following procedure:

1. The nurse connects a drip of saline solution, using a butterfly needle into the patient's vein and lets the solution flow for several minutes;

2. The technician prepares the ^{18}F-FDG activity in the Radinject infuser and inserts it in the shielded stand;

3. The infuser is connected to the three-way valve system by the physician, who starts the automatic infusion and moves away (at least of one meter);

4. The infuser performs two washing cycles with 3 ml of saline solution by the end of the administration.

$KARl_{100}$ efficiently shields medical personnel operating the equipment from dangerous ionizing radiation while administering dosages to individual patients from the initial bulk activity. This system is depicted in the Figure 3.1. On the top working area of the machine there are two shielded

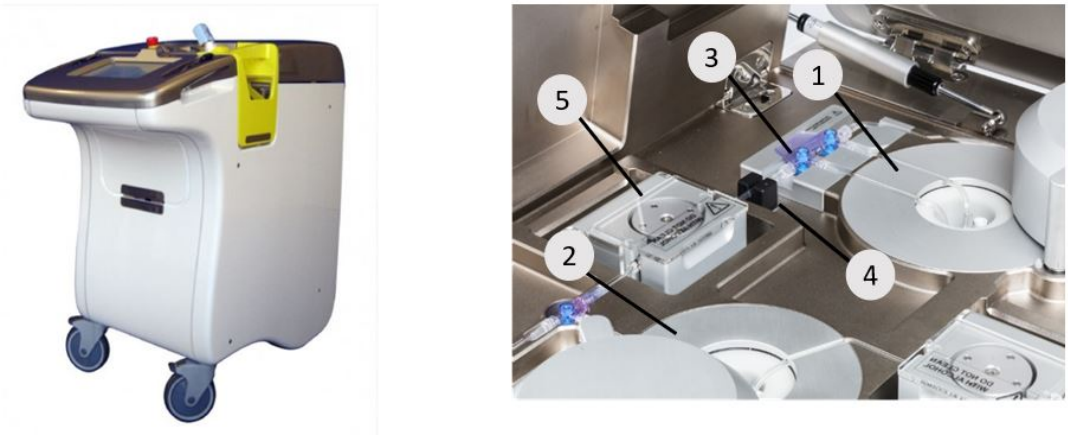

Figure 3.1: KARL100 dispenser system

containers for housing the Mother Vial(MV) (1) where the radiopharmaceutical(RP) to be processed for the day is stored and where the dilution takes place and for housing the dose calibrator (2) where the single dose is measured inside the main kit before transferring it to the syringe. Moreover, there are the components associated to the dispensing operations comprising directional valves (3), bubble sensor (4) and peristaltic pump (5). This part of the machine actuates the loading of radiopharmaceutical into the Mother Vial and manages the preparation of the requested dose inside the dose calibrator. There are also other components associated to the syringe filling as a bubble sensor, pressure sensor and a peristaltic pump.

The logic of dosage preparation for transfer into syringes is based on monitoring the activity concentration inside the dose calibrator at the very first stage of dispensing. To evaluate total radioactivity, the to-be-measured object must remain inside the ionization chamber for roughly ten to twenty seconds. The following syringes will be supplied in accordance with the measured activity concentration. The purpose of this thesis in this phase was to update the way $KARl_{100}$ measures activity concentration in a way to have the RP activity concentration not only at the end of dispensing cycle but also during it. As a result, dispensing accuracy and speed will improve.

3.2 Project Goals

The purpose of this thesis in this phase was to develop the first prototype of a plastic scintillator (PVT) paired with an array of silicon photomultipliers (SiPMs) to be used in the new version of $KARl_{100}$ called $KARl_{200}$. In this approach the machine measures the activity concentration in a way to have the RP activity concentration not only at the end of dispensing cycle but also during it. As a result, dispensing accuracy and speed will improve. For this objective, a plastic scintillator (PVT) paired with an array of silicon photomultipliers (SiPMs) and a dedicated electronic board have been constructed. The output of the electronic board was connected to a counter developed by Tema Sinergie company called "ENVIRO" to evaluate the entire number of counts per seconds (CPS). Correct calibration of this device can improve the performance of the automatic dispenser and, in certain cases, eliminate the requirement for a dose calibrator. The activities described in this sections are as follows:

1. Plastic detector validity assessment in terms of radioisotope half-life evaluation and linearity test for a wide range of activity concentration.

2. Run a test pattern (in collaboration with the S. Orsola-Malpighi Cyclotron facility in Bologna and Hochschule Mannheim University of Applied Science in Germany) with actual radio-fluids (^{18}F, ^{68}Ga, ^{99m}Tc,...) to characterize the measuring in terms of:

   a. Accuracy

   b. Reliability

   c. Repeatability

   d. Stability

3.3 $KARL_{100}$ Dispensing System

Figure 3.2 depicts the $KARL_{100}$ schematic. Each single component is in turn associated with a series of commands that have been implemented at PLC (Programmable Logic Controller) level. There is a daily disposable Kit as shown in Figure 3.3 and syringes Figure 3.4 that is installed on the dispensing

machine easily. The daily disposable kit consists of different parts as (A) saline spike, (B) Double directional valves group, (C) Mother-Vial, (D) Single directional valve, (E) Measuring chamber vial, (F) 0,22μm filter, (G) Needle, (H) No needle connector, (I) Pressure sensor time. A management software, simple and direct, allows FDG administration inside syringes or to patients by a few touches. The $KARL_{100}$ software has the following features:

1. straightforward touch screen interface;
2. traceability and incorruptibility of data, diversified software accesses, daily report and single dose printing

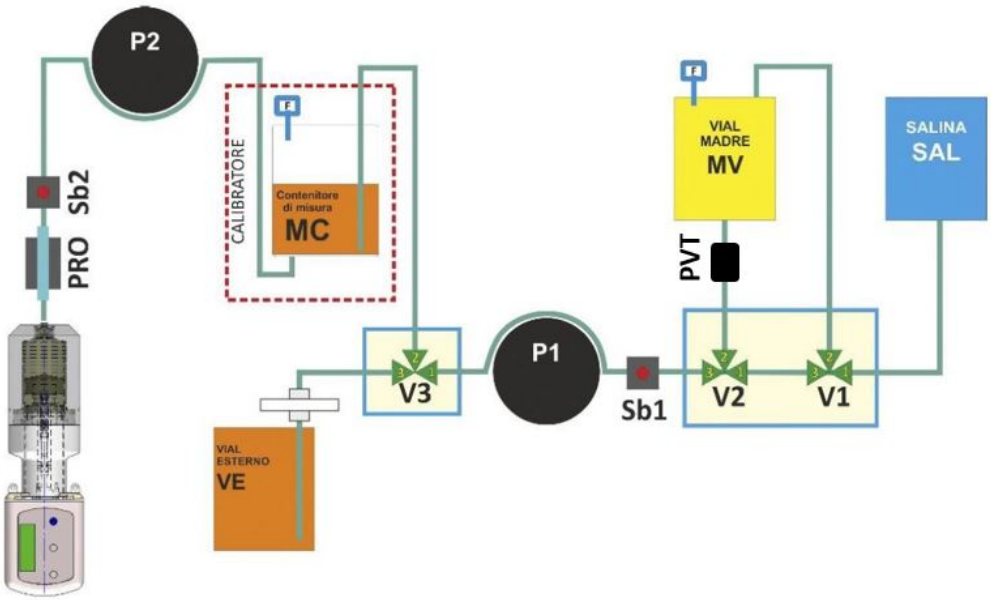

Figure 3.2: KARL100 dispenser system schematic

In this section we will briefly discuss the steps that $KARL_{100}$ follows for dispensing RP from the bulk vial to a syringe.

1. Cold Wizard: When a new cycle is started the operating software checks each dispensing phase using a saline solution in the so-called cold phase to ensure there is no leakage in the kit and each part works properly.

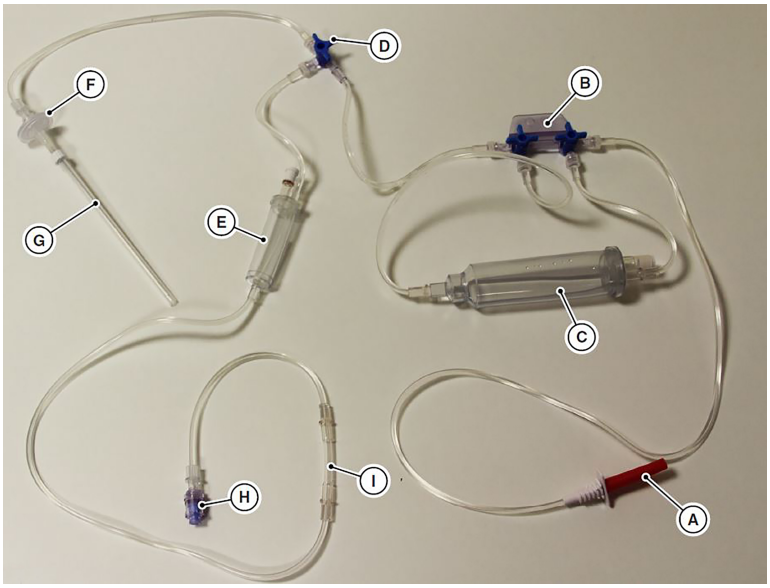

Figure 3.3: Daily Disposable Kit (DDK)

Figure 3.4: Syringe

Moreover, all the preliminary test needed for RP dispensing are performed in this section.

2. Loading and Dilution of the External Vial: The next step is to load the RP from the external vial placed in a lead pot to a container named MV with six cm lead shielding around.

3. Test the Syringe connection: The automatic syringe coupling mechanism on the $KARL_{100}$ is powered by electric actuators designated A.SYR and A.NOA. The effective connection is meticulously scrutinized to prevent radiopharmaceutical leaks in a system with just localized shielding rather than complete shielding.

4. Dispensing: The first stage of dispensing is priming the Kit with RP and saline solution in such a way that the line coming from MV to V2 is filled with RP and the line coming from saline solution to V1 is filled with saline solution. The machine is at rest during this phase, and it returns to this state after each syringe dispensing. After that, the activity concentration is measured and according to that the required dose is dispensed to the syringe.

3.4 $KARL_{200}$ Dispensing System

The purpose of developing the $KARL_{200}$ is to modernize the $KARL_{100}$ while simultaneously reducing the system's size and increasing its precision and speed. Figure 3.5 shows the primary schematic of $KARL_{200}$. The dispensing logic is identical to that of $KARL_{100}$, which means that after priming, the line from the mother vial to V5 is filled with radiopharmaceutical, and the remainder of the line is filled with saline when the system is at rest.

3.5 PVT Based Detector Development

For the purposes of this thesis, a scintillation detector based on polyvinyltoluene (PVT) linked with a series of SiPMs was constructed. In the following we will discuss different parts of this detector.

3.5.1 PVT for scintillation application

Organic scintillators are organic compounds that emit measurable photons in the visible part of the light spectrum once a charged particle or photon passes through them. The mechanism of scintillation in organic materials differs greatly from that of inorganic crystals. The scintillation in inorganic

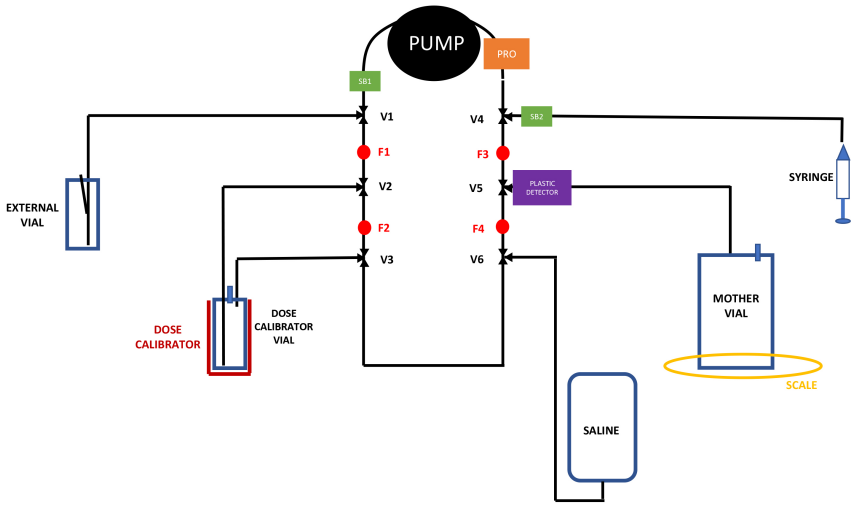

Figure 3.5: Karl200 Dispensing System Schematic

scintillators, such as NaI and CsI, is caused by the structure of the crystal lattice. Transitions in the energy levels of a single molecule cause fluorescence in organic materials. As a result, fluorescence can be observed regardless of the physical state (vapor, liquid, or solid). Organic scintillators in the form of solid, machinable plastics have been a low-cost source of radiation detector material for decades[52]. Around 1950, the first plastic scintillators were manufactured to expand the developing liquid scintillator technology to a solid-phase medium. The constituent molecules of plastic scintillators are distinguished by the presence of a benzene ring structure. Plastic scintillators are solid solutions of organic luminous chemicals dissolved in a polymer matrix that has solidified. The majority of light scintillation plastics are polystyrene and polyvinyltoluene(PVT). PVT is an organic polymer with a molecular formula $C_6H_4 - CH_3 - CH_2 - CH$ that was used for the purpose of this detector development. Figure 3.6 shows the shape of the PVT scintillator and Figure 3.7 depicts its dimension.

3.5.2 SiPM Sensor

Nowadays, PMTs are being replaced with silicone photodiode in scintillator detector technology. This photodiode has the advantage that they can be

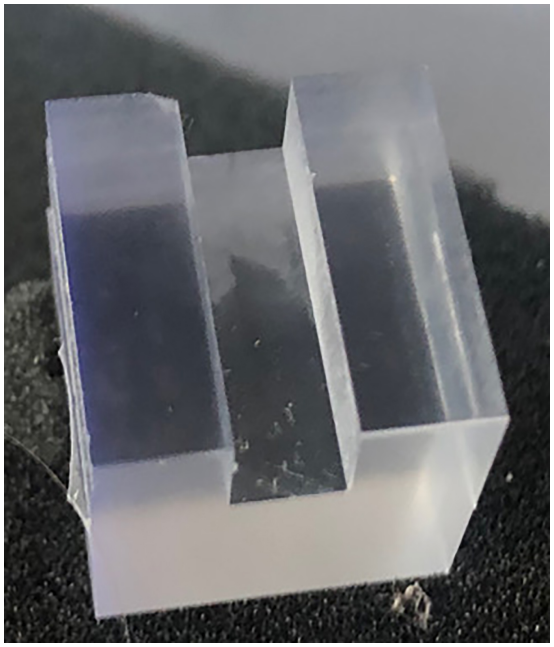

Figure 3.6: PVT detector

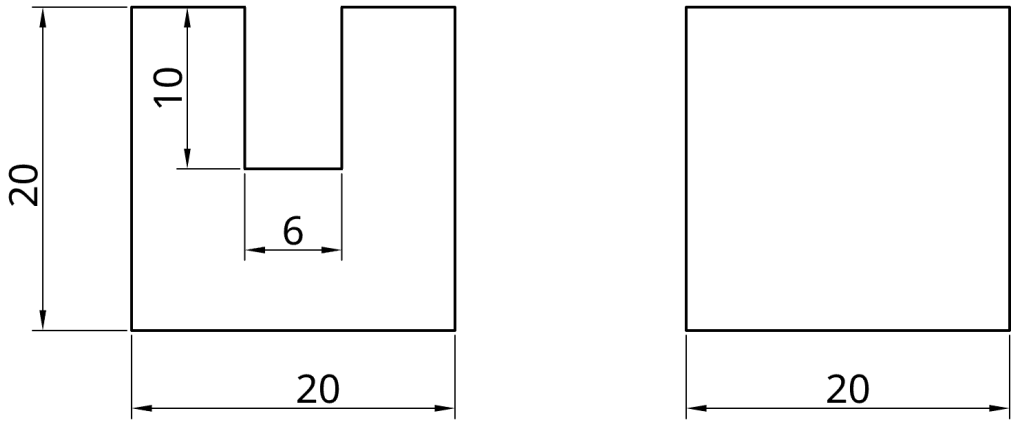

Figure 3.7: PVT detector dimension

made very small and few millimeter thick. Silicone Photomultiplier (SiPM) is a readout device consisting of multiple micro counters, typically 20-30 , in a silicone substrate. Onsemi's J-series low light sensors feature a high PDE (photon detection efficiency) that is achieved using a high volume P-on-N

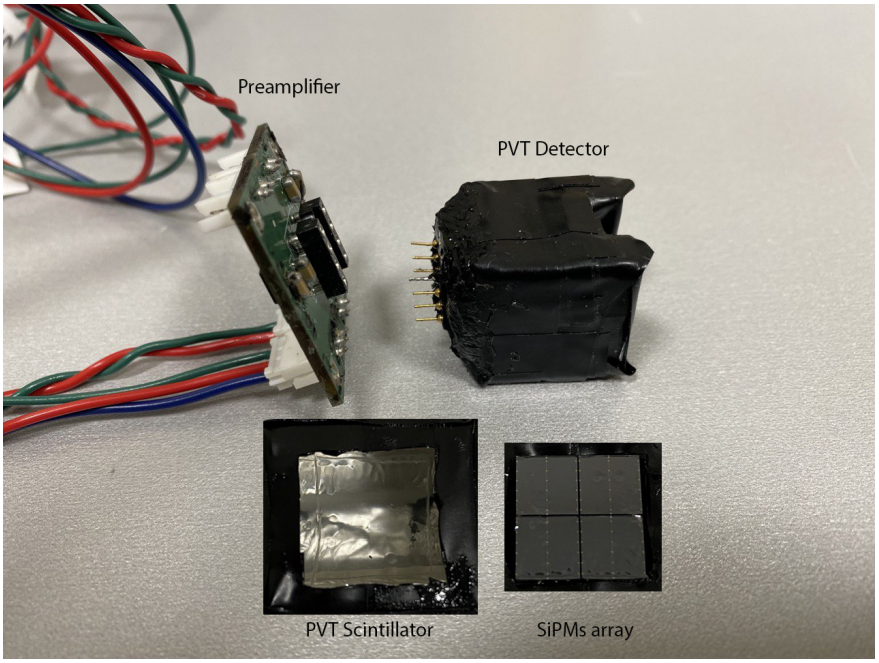

Figure 3.8: PVT detector prototype

silicon foundary process. The J-Series sensors incorporate major improvements in the transit time spread which results in a significant improvement in the timing performance of the sensor. The J-Series Silicon Photomultipliers combine high performance with the practical advantages of solid state technology: low operating voltage, excellent temperature stability, robustness, compactness, output uniformity and low cost. In this thesis the SiPMs array consists of four elements, each with a 6×6 mm active surface with the bias voltage of 30 V were used. Figure 3.8 represents the primary prototype of the PVT detector. In this prototype the SiPMs sensors were attached on the bottom of the plastic scintillator using optical glue to reduce the internal reflection of the light and increase the amount of light reach to SiPM. A layer of silicone rubber was put between the SiPMs and the crystal to improve optical coupling efficiency. To maximize the likelihood that photons produced by scintillation are recorded by the SiPMs sensor, the plastic was covered in reflective aluminum foil. To prevent ambient light from reaching the SiPMs, the entire detector was wrapped in black, opaque tape. The detector is linked to the preamplifier and an electronic board for pulse shaping and counting.

3.5.3 Electronic Board

The SiPM was linked to a preamplifier with symmetrical 5 V power and a pulse-shaping amplifier. The SiPM receives a stable bias voltage from an ultralow noise LDO. An ultralow noise LDO (Low Drop-Out) regulator is a type of electronic voltage regulator that is designed to provide a stable output voltage with minimal noise and ripple. LDO regulators are commonly used to provide a stable voltage for sensitive electronic circuits such as microprocessors, sensors, and communication devices. The term "ultralow noise" refers to the regulator ability to provide a very clean and stable output voltage, with minimal high-frequency noise and ripple. This is achieved through careful design of the regulator internal circuitry, including the use of low-noise components, high-quality voltage references, and advanced filtering techniques. Ultralow noise LDO regulators are particularly useful in applications where low noise is critical to the performance of the circuit, such as high-precision measurement systems, medical devices, and audio equipment. They are also commonly used in low-power, battery-operated devices where efficient power management is important[53]. The bias voltage may be adjusted to provide the desired overvoltage ($\Delta V = V_{bias} - V_{breakdown}$). This allows for the adjustment of the detector gain. The analog signal is filtered in order to eliminate the temperature-dependent offset. In electronic circuits, temperature can cause electrical components to drift from their normal values, which can introduce a signal offset. By filtering the analog signal, the temperature-dependent offset can be removed, and the accuracy of the signal can be improved. This helps us enhance the signal dynamics and stability. Figure 3.9 depicts the amplifier output while utilizing a ^{137}Cs point source. When an analog signal is processed, it can contain unwanted noise, which is a random fluctuation in the signal caused by various sources, such as interference from other electrical devices, thermal noise, or shot noise. Additionally, the signal may contain very low energy or weak signals that are not significant or useful for the intended purpose. To eliminate such unwanted noise and weak signals, the analog signal is compared to a threshold. The threshold is a predetermined lower level that is set to filter out any signal below a certain amplitude. Any signal that is weaker than the threshold is considered noise or irrelevant, and it is discarded or filtered out. By eliminating noise and very low energy signals, the signal-to-noise ratio (SNR) of the signal can be improved. A high SNR means that the signal is stronger than the noise,

and it can enhance the accuracy and reliability of the signal processing. So, the analog signal is compared to a threshold (lower level) to eliminate noise and extremely low energy pulses. When the analog signal is compared to this threshold, any part of the signal that exceeds the threshold is considered significant and is retained, while any part of the signal that is weaker than the threshold is filtered out. So, every time the analog signal passes over the threshold it generates a switch in the output. In the context of converting analog signals into digital pulses, each significant peak in the analog signal that passes over the threshold can be converted into a digital pulse. When the peak passes over the threshold, it generates a switch in the output, which can trigger the generation of a digital pulse. By repeating this process for each significant peak in the signal, the analog signal can be converted into a series of digital pulses. The process of converting analog signals into digital pulses is commonly used in various applications such as signal processing, communication, and data acquisition. The digital pulses can be easily transmitted, stored, and processed by digital circuits, and they can provide a more accurate and reliable representation of the original analog signal. The digital signal is then processed to obtain fixed width pulses of 1μs. Finally a radiation counter from Tema sinergie company called ENVIRO was used for reading the number of counts per seconds. The data collection program is called WinTAM. Figure 3.10 depicts the detector system.

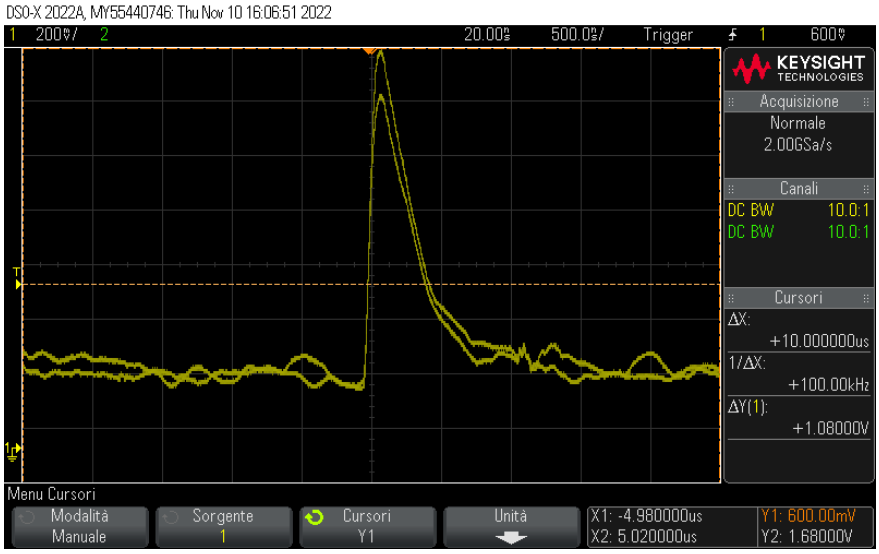

Figure 3.9: Amplifier output signal for a Cs-137 point source

Figure 3.10: PVT detector system

3.6 Effect of Temperature on the PVT Detector

In order to investigate the effect of temperature on the output of the PVT detector, a climate chamber with the capability of adjusting temperature and relative humidity was used. Temperature was varied between 17-32 °C with

three degree steps. A ^{137}Cs point source was placed in contact on top of the detector as shown in Figure 3.11. As a result the number of CPS was acquired for ten minutes. The experiment was repeated for five times and standard deviation was evaluated. Figure 3.12 depicts the effect of temperature on PVT detector. As can be seen the total number of CPS decreases as temperature increase. The reason is that the SiPM gain and photon detection efficiency are overvoltage dependent. The breakdown voltage (V_{br}) of SiPM increases with increasing temperature because a higher temperature generates a larger population of phonons, therefore a larger electric field and bias voltage are required to overcome an enhanced carrier cooling caused by phonon scattering phenomenon. As the bias voltage is a fixed value, by increasing the breakdown voltage the gain decrease and consequently the number of counts decrease.

Figure 3.11: Source detector geometry inside climate chamber

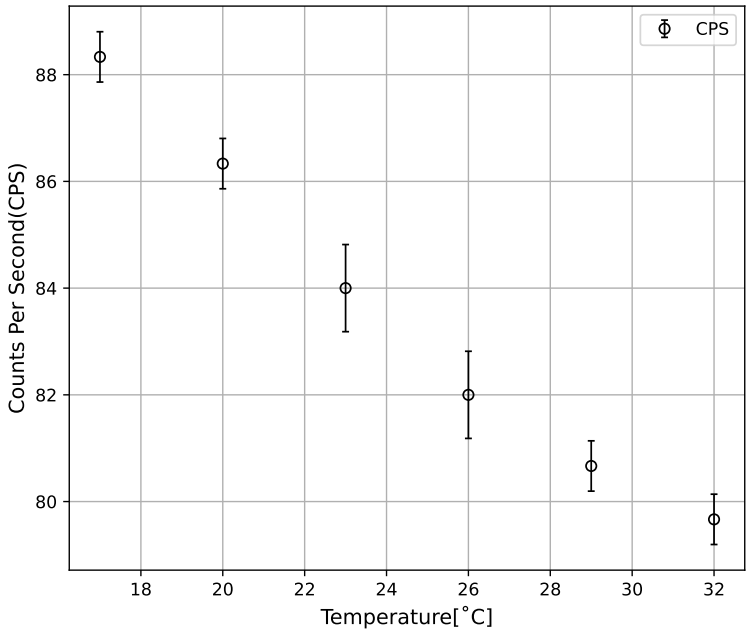

Figure 3.12: Effect of temperature on PVT detector

3.7 PVT Detector Stability

In this study, the PVT detector reliability was tested using a Cs-137 point source. In order to measure the CPS, a ^{137}Cs point source was brought into contact with the PVT detector for 20 hours. The behavior of the detector is illustrated in Figure 3.13. Considering the outcomes, we can say that the detector acts stable because of the flat count rate trend. The low activity source is responsible for the outlier value.

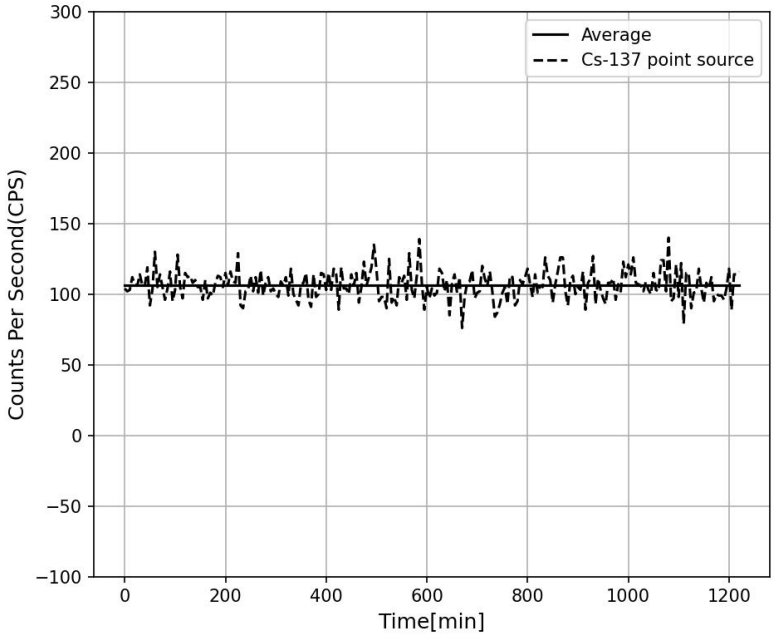

Figure 3.13: PVT detector stability using Cs-137 point source

3.8 PVT Detector Dead Time

Every radiation counting system possesses a dead time or pulse resolving time(τ)that is proportional to the time necessary to process individual observed events. A pulse from a radiation detector has a fixed time period, therefore if a second pulse occurs before the first has faded, the two pulses will overlap to generate a single warped pulse. Counting systems are typically classed as paralyzable or nonparalyzable[6]. A nonparalyzable system is one in which, if an event happens during the dead time of a previous event, the second event is simply ignored, with no effect on subsequent occurrences. A paralyzable system is one in which each event, whether or not it is counted, introduces a dead time. Thus, an event that occurs during the dead time of a preceding event is not counted, but it does establish its own dead period during which subsequent events cannot be recorded. A paralyzable system

is one that has an "extendable" dead period. Nonparalyzable systems are widely observed in digital counters, pulse-height analyzers, and computer interfaces. Due to dead time losses, the true counting rate R_t (cps), which is the counting rate that would be recorded if $\tau = 0$, is lower than the observed counting rate R_o (cps). When considering the connection between R_o, R_t, and τ one must first consider the type of dead time[54]. In case of nonparalyzable systems:

$$R_t = R_o/(1 + R_o\tau) \tag{3.1}$$

where τ is given in seconds. If the system has a paralyzable dead time, then:

$$R_o = R_t e^{-R_t\tau} \tag{3.2}$$

Figure 3.14 shows the detector system behavior for paralyzable and nonparalyzable systems.

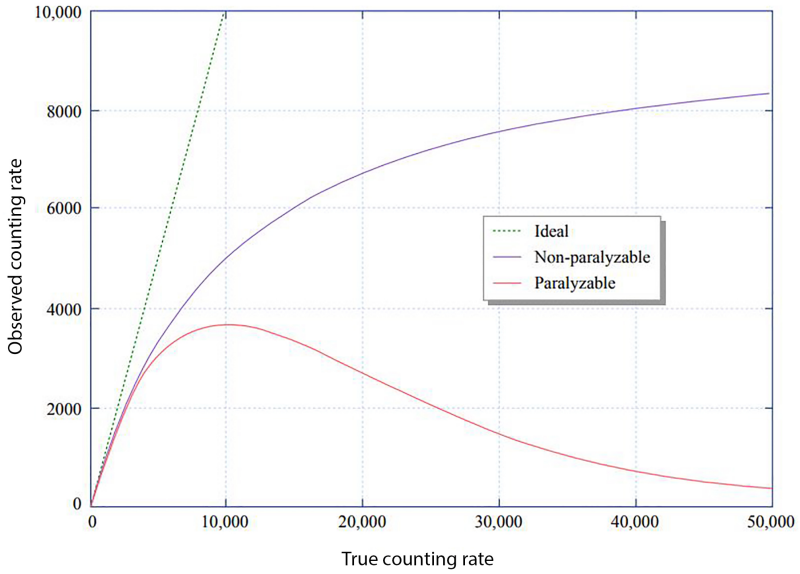

Figure 3.14: Observed (R_o) versus true (R_t) counting rate curves for paralyzable and nonparalyzable systems having the same dead time value, τ,[54]

Measurements made on systems with a standardized measuring configuration can be corrected for dead time losses using the mathematical models

explained above. The PVT detector developed in this study is suited for high activity concentrations between 10 and 1000 MBq/mL. Therefore, it is essential to evaluate the dead time of the detector and adjust the data accordingly. A tube with an inner diameter of 0.6 mm and an outside diameter of 4 mm is the source of activity. For the dead time measurement, ^{18}F radioisotope with 1250 MBq/ml activity concentration was injected into a 20-centimeter-long tube that passed through the detector as illustrated in Figure 3.15. In order to evaluate whether the detector system functions as a paralyzable or nonparalyzable system, a graph of the observed counting rate vs. activity concentration was generated. Figure 3.16 depicts the nonparalyzable behavior of the system. The detector dead time was calculated 2.746 μs and the measured CPS were corrected for the dead time losses, and the results were given in the same graph.

Figure 3.15: Experimental setup for linearity test

3.9 PVT Detector Reliability

In the initial testing, the entire setup was assessed in terms of radioisotope half-lives evaluation. Several commonly used medical radioisotopes, including ^{99m}Tc, ^{18}F, ^{11}C, and ^{68}Ga were used for this purpose.

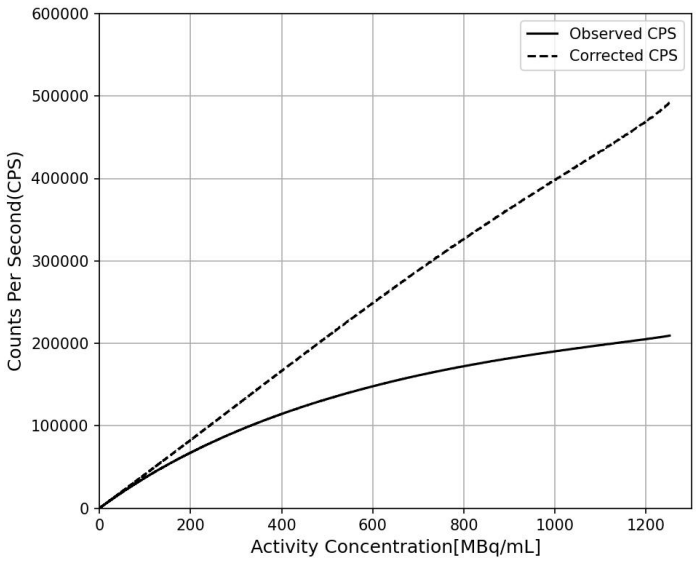

Figure 3.16: CPS versus activity concentration for PVT detector

3.9.1 Radioisotope preparation

The above mentioned radioisotopes were produced at S.Orsola cyclotron facility in Bologna, Italy. ^{18}F, ^{11}C were generated using the PET cyclotron facility as introduced in 2.10.2.1. ^{18}F is in the form of liquid after production and can be used directly in our experiment. ^{11}C is in the form of gas and was used after synthesis. ^{99m}Tc was obtained from S.Orsola hospital. Three Ge-68/Ga-68 generators were connected together in series as shown in Figure 3.17 in order to produce higher activity of ^{68}Ga in this experiment. ^{68}Ga was eluted with a few mL of hydrochloric acid from generators.

To assess the detector performance, a number of tests were run. For these tests, the same setup as in Figure 3.15 was utilized. Radioisotopes were injected within the tubing, and the decay behavior of each radioisotope was recorded. Using ^{18}F, ^{123}I and ^{68}Ga, the identical experiment was carried out at the Mannheim University of Applied Science in Germany. **??** shows the decay behavior of different medical radioisotopes studied using PVT detector. Table 3.1 depicts the evaluated half-lives and their deviation from the

Figure 3.17: Three ^{68}Ga generators were connected in series

expected one. As can be seen from the results, the deviation between the evaluated half-lives and the expected values is low and it means the detector is accurate in terms of half-life measurements.

Table 3.1: Evaluated half-lives for several radioisotopes

Radioisotope	Evaluated Half-Life(min)	Expected Half-Life(min)	Deviation(%)
^{99m}Tc	367.92±0.41	360.6±60	2.0
^{18}F	109.75±0.35	109.77±5	0.0167
^{11}C	20.62±0.34	20.34±2	1.0
^{68}Ga	67.82±0.25	67.629±24	0.29

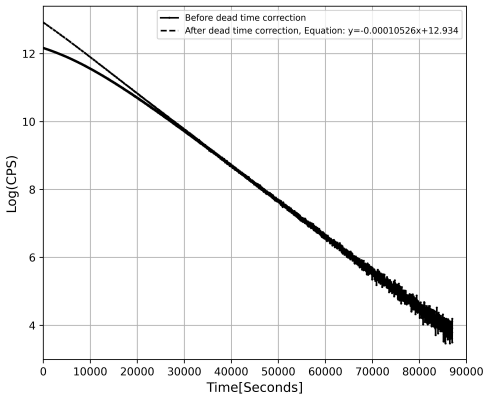

(a) ^{18}F decay behavior

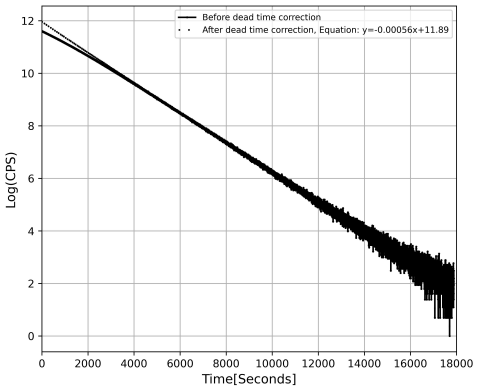

(b) ^{11}C decay behavior

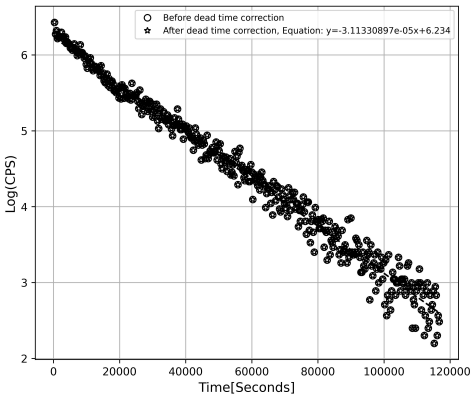

(c) ^{99m}Tc decay behavior

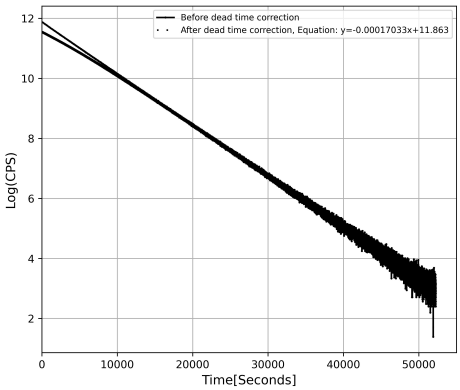

(d) ^{68}Ga decay behavior

Figure 3.18: Half-Life evaluation of several medical radioisotope using PVT detector.

3.10 PVT Detector Linearity

The linearity of the detector was investigated in a wide range of activity concentration using different medical radioisotopes like ^{18}F, ^{11}C, ^{13}N,^{68}Ga with the activity concentration of 934, 291, 1368, 194 MBq/ml respectively. The radioisotopes were injected in the tubing passing through the detector and their decay behavior were registered. The observed CPS for each radioisotope was compared with the expected values in the entire activity concentration. Regarding the results shown in Figure 3.19 the linear response of the detector over the whole range of desired activity concentrations was confirmed after data corrections for the detector dead-time, obtaining a deviation from expected response <5% in high activity concentrations.

3.11 Detector Behavior on Dispenser

To evaluate the behavior of the detector during the automatic dispensing of radioisotope, the PVT detector was positioned on the top working area of the $KARL_{100}$ dispenser system, as shown in Figure 3.2. The tube between the mother vial and V2 of the daily disposable kit was lengthened so that it could pass through the detector. As we discussed before the automatic dispensing logic in $KARL_{200}$ will be the same as $KARL_{100}$. Figure 3.20 represents the PVT detector placed on the $KARL_{100}$ dispenser in the experimental setup. A known activity concentration of ^{18}F was loaded inside the mother vial. Seven syringes with various activities were dispensed automatically using $KARL_{100}$ software. The detector behavior was registered using WinTAM software during the whole dispensing cycle. The first syringe preparation comprises two phases: getting the machine ready for dispensing is the first stage, which results in dilution of the activity inside the mother vial. The second step is to measure the ^{18}F activity concentration using the ionization chamber and accordingly dispense the first syringe for the requested activity. The activity concentration evaluated in this step is the reference value for dispensing the next syringe. When the lines have been primed, we always have the line from the mother vial to V2 that also passes through the detector filled with radioisotopes. Regarding the next syringes, the requested activities were prepared inside the ionization chamber and then transferred to the syringes. Figure 3.22 depicts the number of count rates received by the PVT detector

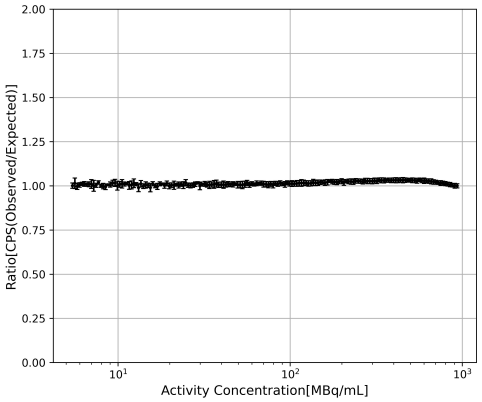

(a) ^{18}F Linearity test

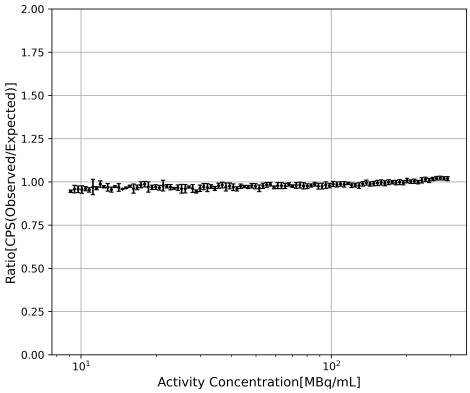

(b) ^{11}C Linearity test

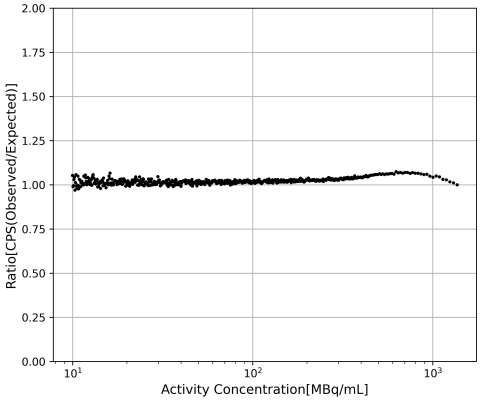

(c) ^{13}N Linearity test

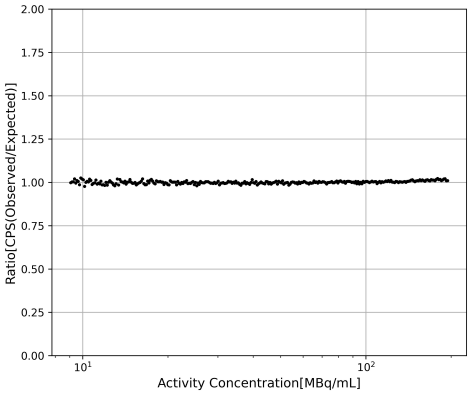

(d) ^{68}Ga Linearity test

Figure 3.19: Linearity test of PVT detector for several medical radioisotope.

during the dispensing process. The black curve shows the detector response for the first syringe preparation. In the priming phase, the machine takes an estimated amount of activity from MV to reach the rising edge of the first bubble sensor (BS1) in order to be sure that the line from MV to V2 is filled with ^{18}F. So in this step, the number of CPS increases to its maximum value. Then V2 will be closed, and the additional amount of ^{18}F from V2 to BS1 will be pushed into the ionization chamber with some saline solution. This is the part where we see the decrease in CPS observed by the detector. Figure 3.21 shows all the steps during priming the lines. At the end of the priming phase, the activity in the ionization chamber will be transferred back to the MV, which leads to a little dilution of the activity in the MV. In the next step, the machine takes the known volume of activity from the MV and transfers it to the ionization chamber to evaluate the activity concentration in the MV and prepare the first syringe based on the requested activity. The reason for the observed decrease in the count rate is the decrease in activity concentration in the MV. The yellow curve was obtained while the second syringe was being produced. As can be seen in this curve, we see a step in the count rates, and this is due to the fact that the long length of tubing from MV to V2 is not still completely full with the new diluted activity concentration after the first syringe was prepared. Regarding the next syringes, a stable behavior with the same count rate was obtained. Because of the layer of shielding, a small spike may be visible, which is caused by the transmission of activity from V2 to the dose calibrator. These findings enable us to calibrate the system in the configuration that the machine has after priming and, as a result, monitor the activity concentration before each syringe dispensing. In this situation, we can speed up the dispensing procedure while increasing dispensing accuracy. This experiment was repeated five times and the same behavior was observed.

3.12 Calibration Factor Evaluation

In this first prototype, calibration factor equals to CPS/MBq was examined for certain PET radioisotopes such as ^{18}F, ^{11}C, ^{68}Ga when the machine is at rest (only the pipe from MV to V2 is filled with activity and the rest of the kit is empty). In this investigation a shielding with 2-cm thickness was placed around the detector to decrease the background as seen in Figure 3.23.

Figure 3.20: PVT detector placed on KARL100 dispenser

Firstly, the radioisotope with known activity concentration was loaded inside the MV. To fill the line from MV to V2, the necessary volume of activity was drawn from MV using the peristaltic pump. The number of CPS was recorded using WinTAM software for three minutes and the calibration factor was evaluated for each radioisotope. The experiment was repeated five times by transferring specific amount of activity from mother vial to the ionization chamber and flushing the transfer line using saline solution. Table 3.2 shows the evaluated calibration factors for several medical radioisotopes like ^{99m}Tc, ^{18}F, ^{11}C, ^{68}Ga. ^{99m}Tc is a gamma emitter radioisotope with the energy of 141 KeV. ^{18}F, ^{11}C, ^{68}Ga emit 511 KeV gamma radiation due to the positron annihilation accompanying with positrons due to the beta decay.

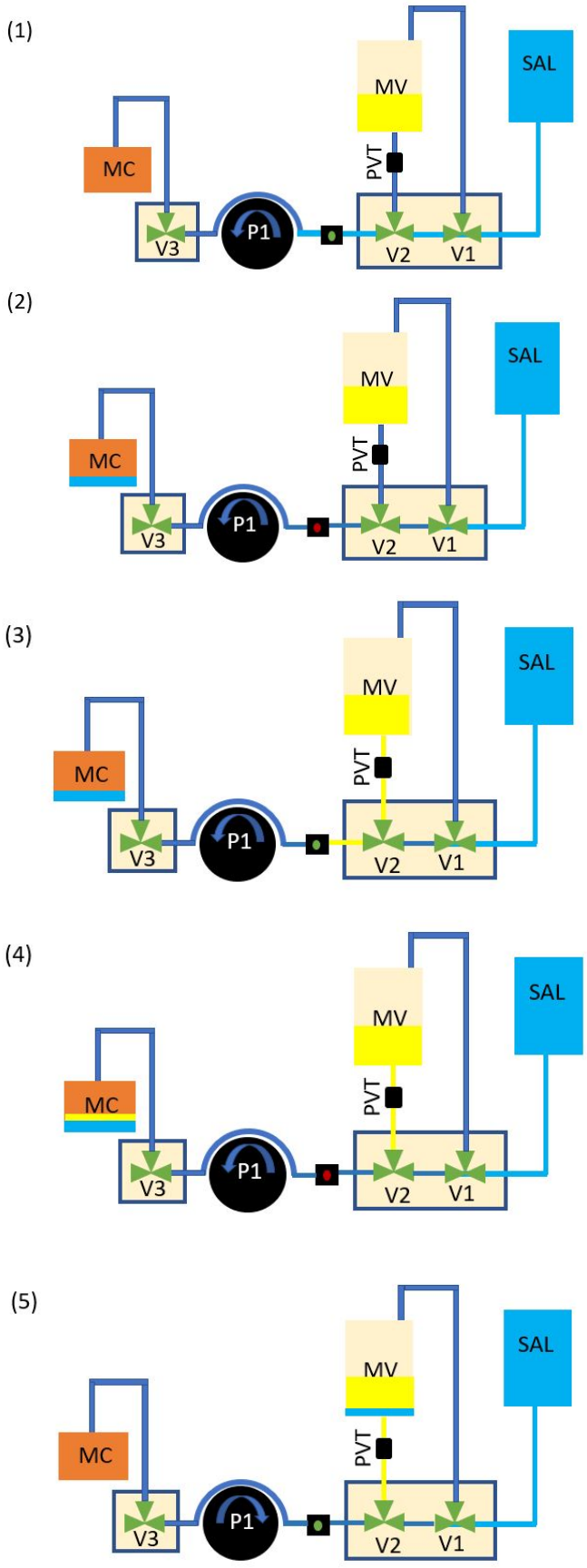

Figure 3.21: priming part schematic: light blue=saline, yellow=radioactivity

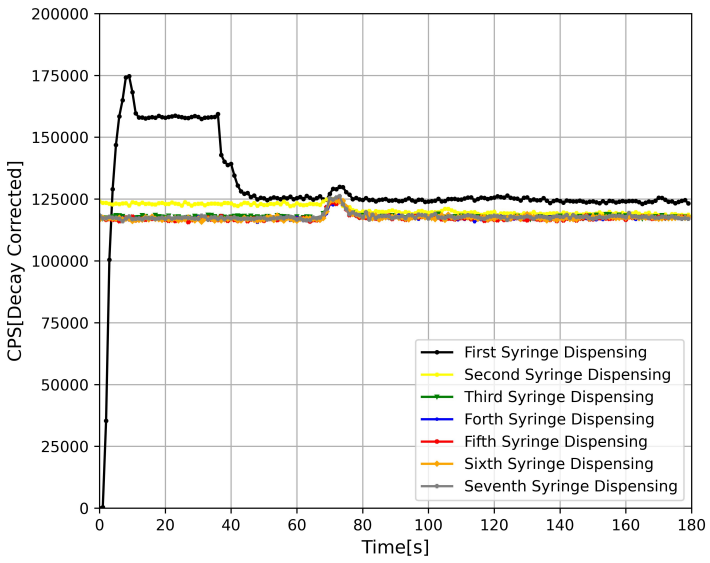

Figure 3.22: PVT detector behavior during automatic syringe dispensing

Table 3.2: Evaluated calibration factor for several radioisotopes

Radioisotope	Gamma or X	Beta	Calibration-Factor [CPS/MBq/ml]
	E/%	E/%	
^{99m}Tc	141/89	-	1.023±0.069
^{18}F	511/194	634/97	192.15±11.00
^{11}C	511/200	960/100	212.21±12.00
^{68}Ga	511/178 1077/3	822/1 1899/88	743.57±41.60

3.13 Monte Carlo Simulation

3.13.1 Effect of Beta Particles

To determine how much beta particles can alter the calibration factor, a Monte Carlo simulation was employed. The PVT detector was simulated using FLUKA with the dimensions described in Figure 3.7. A thin layer of alu-

Figure 3.23: PVT detector placed on KARL100 dispenser inside a 2-cm shieslding

minum and the tape were also simulated, as seen in Figure 3.24. A PVC tube with inner and outer diameters of 0.06 cm and 0.4 cm and a length of 20 cm was simulated and considered as the source of activity. The set of defaults called EM-CASCA was used for the simulation. Radioactive sources were defined as isotropic source in the BEAM card. The simulation was carried out for the radioisotopes ^{18}F, ^{11}C, and ^{68}Ga. Using a USRBIN card, the distribution of positrons flux inside the PVT detector was examined. In addition, the energy spectrum was acquired using the Detect card. Ga-68 decays by emitting a positron with a maximum energy of 1.9 MeV, whereas F-18 decays by emitting a positron with a maximum energy of 0.63 MeV. The higher energy of the positron emitted by Ga-68 means that it travels further in the surrounding material before it interacts with an electron and undergoes annihilation, producing two 511 keV photons that can be detected by the PVT detector. This means that the positron emitted by Ga-68 has a higher probability of interacting with the PVT detector and producing a measurable signal. In addition, Ga-68 has a shorter half-life (68 minutes) than F-18 (110 minutes), which means that it decays more rapidly and produces more positrons per unit time than F-18. This also contributes to the higher CPS detected by the

PVT detector for Ga-68 compared to F-18.

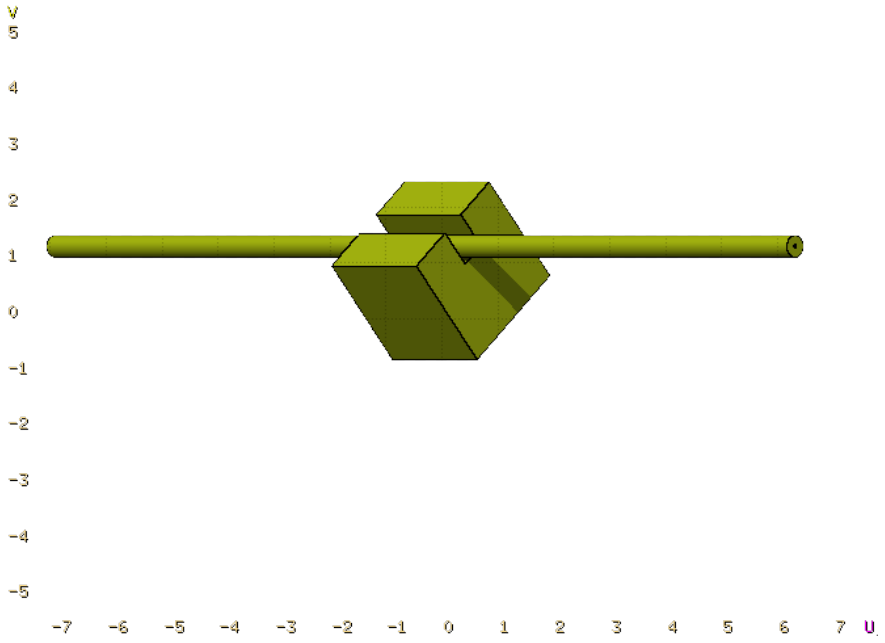

Figure 3.24: Simulated PVT detector prototype using FLUKA

As seen in Figure 3.25, Figure 3.26, Figure 3.27 mostly the compton shoulder is visible due to the low atomic number of PVT plastic.

Additionally, the positron profile was generated by converting the output of the USRBIN card to raw data with a Python script and then analyzing the data with ImageJ software. The results of the positron flux distribution related to ^{18}F, ^{11}C, and ^{68}Ga were shown in Figure 3.28, Figure 3.29, Figure 3.30 respectively. Regarding the positron flux from ^{18}F, it is visible that all of the positrons stop in the tubing before reaching the detector. The positrons from ^{11}C are more energetic and a small percentage of them (around 0.20%) can reach to the detector and consequently can affect on the number of CPS. In case of ^{68}Ga, around 5.7% of emitted positrons can reach the sensitive part of detector.

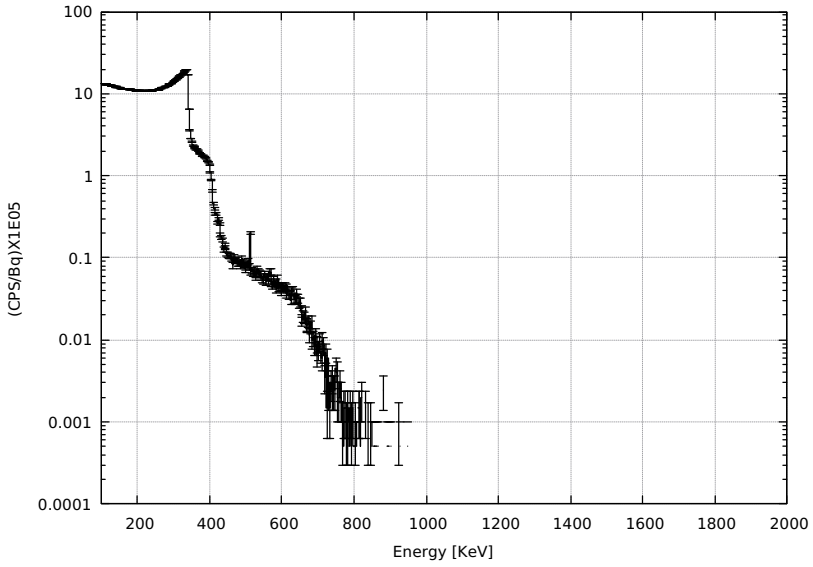

Figure 3.25: Energy spectrum of ^{18}F using PVT detector

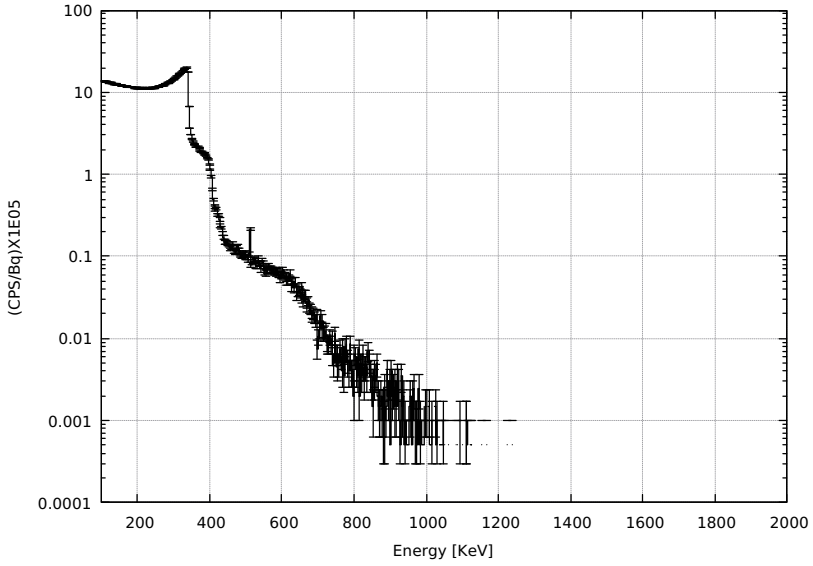

Figure 3.26: Energy spectrum of ^{11}C using PVT detector

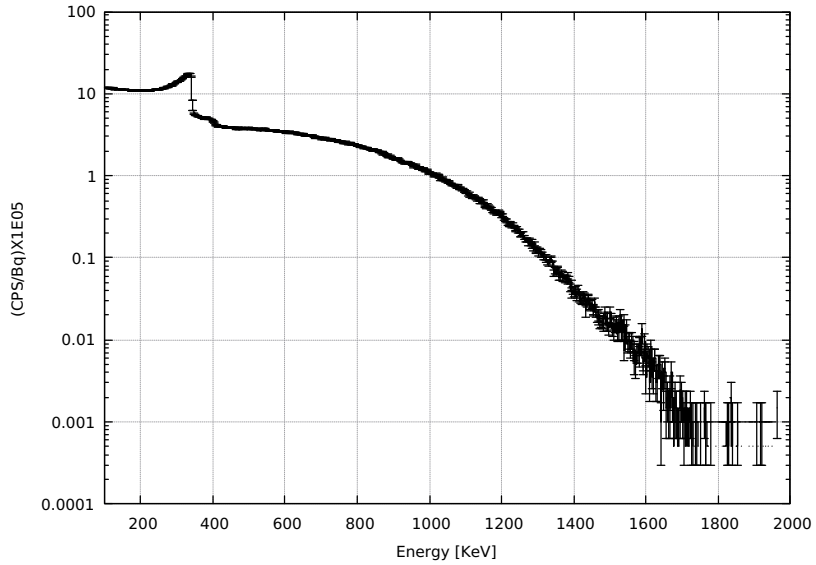

Figure 3.27: Energy spectrum of ^{68}Ga using PVT detector

3.13.2 Shielding Design

Due to the fact that, in the case of ^{68}Ga, positrons contribute to the final calibration factor and can lead to unrepeatable detector behavior as a result of modest geometry changes, it would be advantageous to consider beta particle shielding. To prevent beta particles from entering the sensitive section of the detector, a plexiglass shielding was designed for the PVT detector using FLUKA. Also, further tungsten shielding was proposed for gamma background coming from other sections of the kit. The simulated prototype with the plexiglass shielding dimension in X-Y projection is depicted in Figure 3.31. A radioisotope-filled tubing with inner and outer diameters of 0.06 and 0.4 cm and a length of 13.5 cm was passed through the detector. The simulation was performed for ^{18}F, ^{11}C and ^{68}Ga by defining each isotope in the BEAM card.

The energy spectra of ^{18}F, ^{11}C and ^{68}Ga were plotted in Figure 3.32, Figure 3.33, Figure 3.34. Moreover, the positron flux distribution was depicted in Figure 3.35. According to the USRBIN and DETECT cards we can conclude that the proposed shielding can stop the large majority of high energy beta particles emitted from ^{68}Ga. However, it is important to note that adding a shielding material can also reduce the number of gamma rays that reach

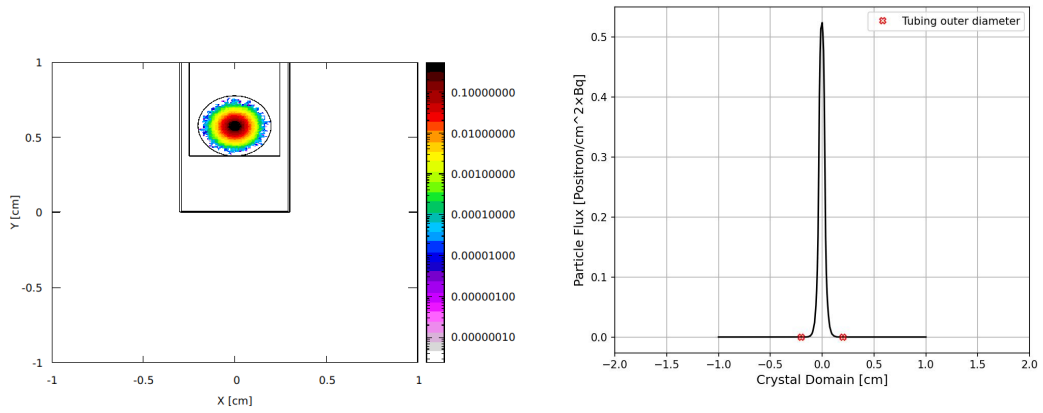

(a) The positron flux distribution emitted from ^{18}F by USRBIN card

(b) The profile of the positron flux distribution emitted from ^{18}F

Figure 3.28: ^{18}F positron distribution

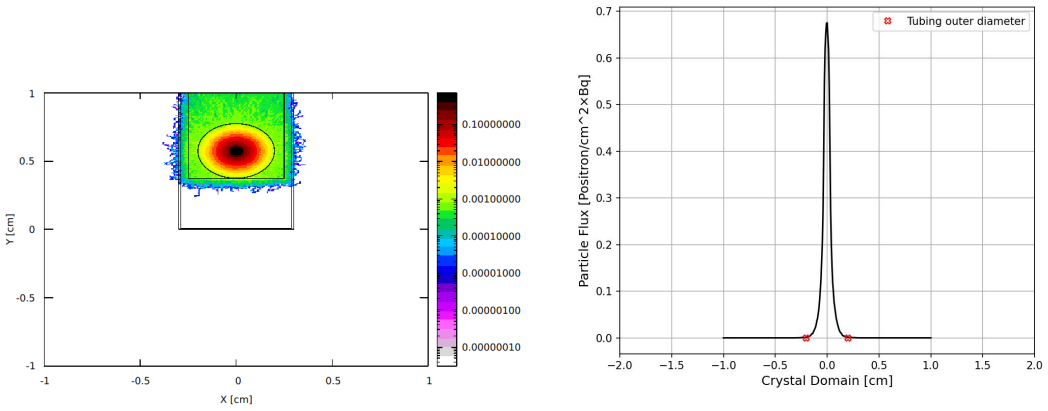

(a) The positron flux distribution emitted from ^{11}C by USRBIN card

(b) The profile of the positron flux distribution emitted from ^{11}C

Figure 3.29: ^{11}C positron distribution

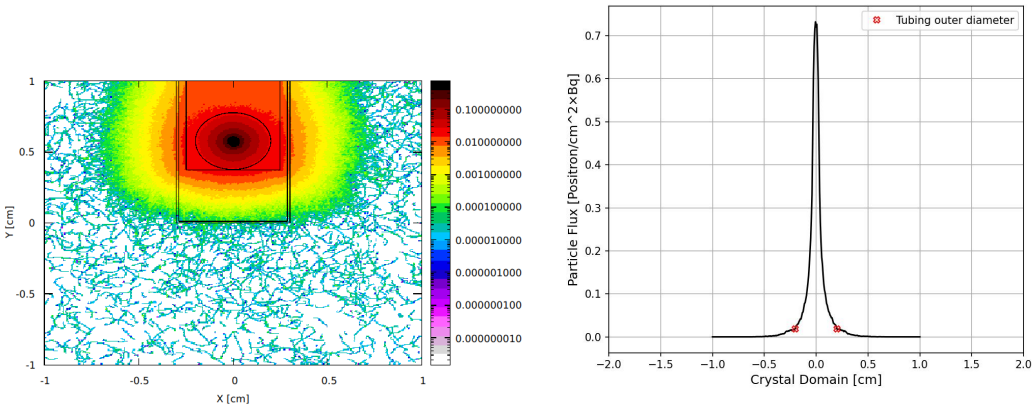

(a) The positron flux distribution emitted from ^{68}Ga by USRBIN card

(b) The profile of the positron flux distribution emitted from ^{68}Ga

Figure 3.30: ^{68}Ga positron distribution

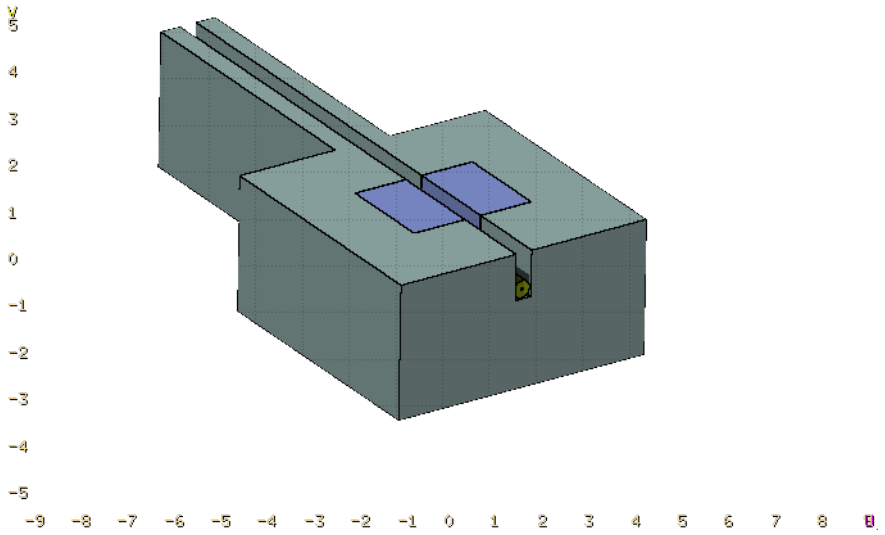

Figure 3.31: 3D simulation of the PVT detector prototype with the shielding using FLUKA

the detector, especially if the shielding is too thick or made up of a material that absorbs gamma rays too strongly. Therefore, the optimal thickness and material of the shielding depend on the specific application and the energy range of the gamma rays of interest. In summary, using a 0.5 cm thick plexiglass shielding can potentially improve the sensitivity of a plastic detector to gamma rays, but it is important to carefully consider the optimal thickness and material of the shielding and ensure that it does not introduce any additional sources of background radiation.

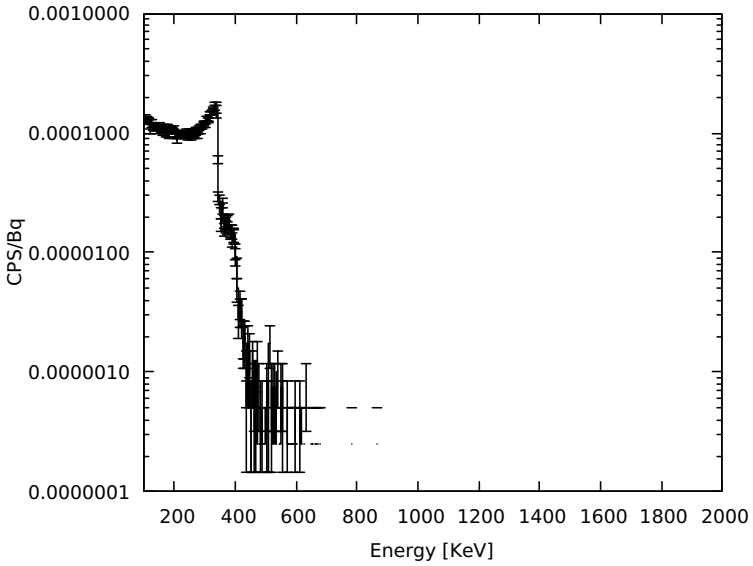

Figure 3.32: Energy spectrum of ^{18}F using PVT detector after beta shielding

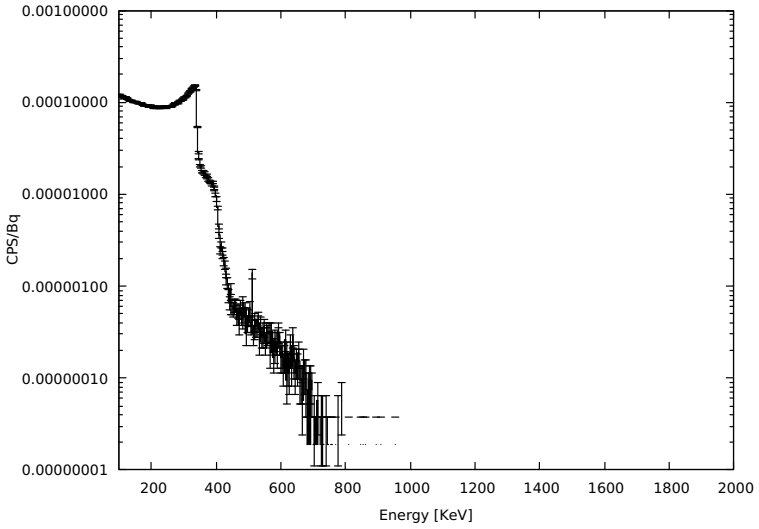

Figure 3.33: Energy spectrum of ^{11}C using PVT detector after beta shielding

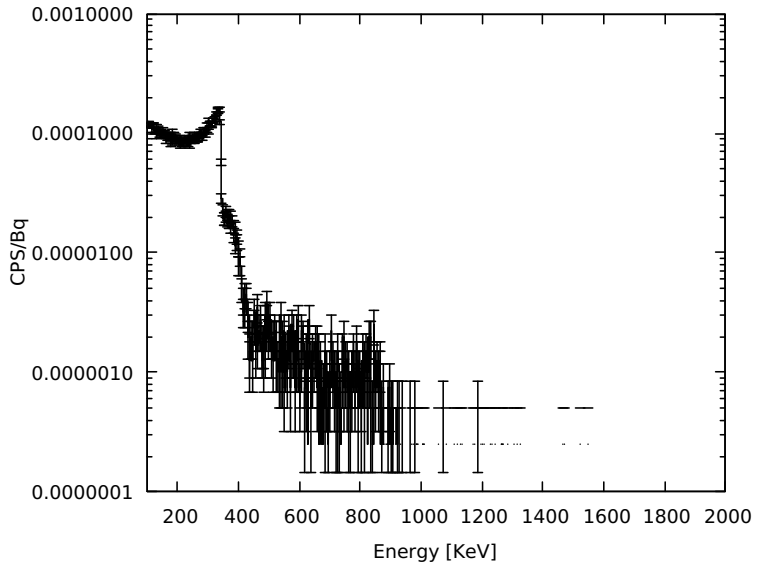

Figure 3.34: Energy spectrum of ^{68}Ga using PVT detector after beta shielding

3.13.3 Shielding Design for Mother Vial

The activity of one entire day is stored in the mother vial. In order for the PVT detector to function reliably, it must be appropriately shielded so that

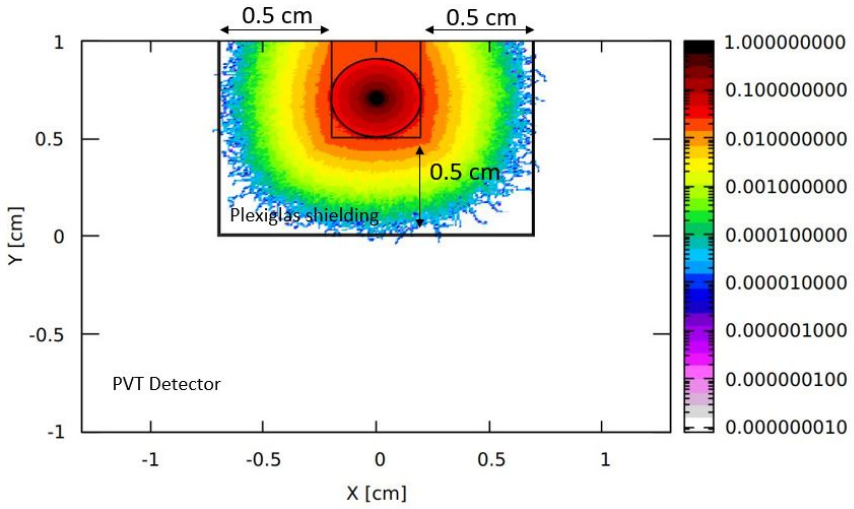

Figure 3.35: ^{68}Ga positron distribution after beta shielding

nothing from the activity within the MV affects the detector counting. For this purpose, a 6 cm cylindrical lead shielding was considered around the MV. Furthermore, another 2 cm of tungsten was considered for the PVT detector. The vial containing the radiopharmaceuticals with 50 cm^3 volume was placed inside the cylindrical shielding. Figure 3.36 depicts the simulated geometry.

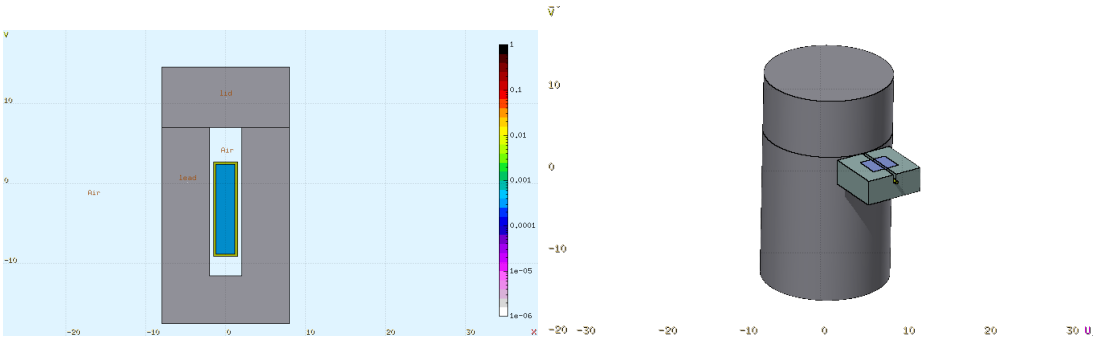

Figure 3.36: Left: X-Y projection of the simulated mother vial and lead shielding around, Right: 3D simulation of the mother vial and PVT detector prototype with the shielding using FLUKA.

USRBIN card was used to register the photon flux distribution and Detect card was used to score the CPS/Bq. Figure 3.37 shows the photon distribution from ^{18}F radioisotope inside the mother vial. As can be seen the 511 keV

photons will be absorbed by the lead shielding. The number of CPS/Bq registered in PVT detector is 9.50E-09. The maximum amount of activity that can be stored in MV is 1 Ci which equals 37000 MBq. So, the number of CPS received by the PVT detector is 3.52E-04. Thus, the designed shielding is enough for protecting the PVT detector from the background comes from the MV.

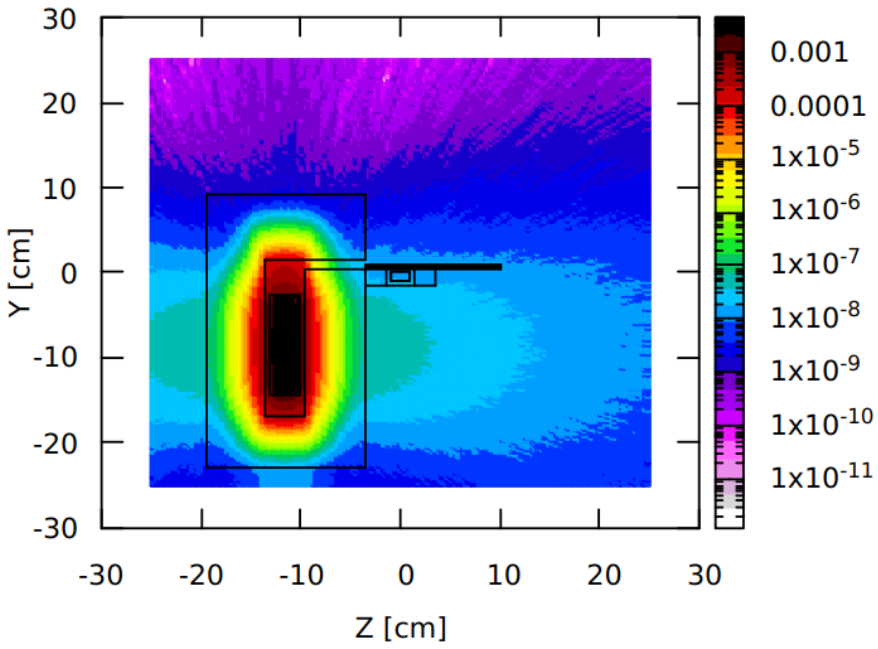

Figure 3.37: ^{18}F photon distribution in the mother vial

3.14 Conclusion

In this chapter, we have presented the development of a novel sensor for continuous measurement of radiopharmaceutical activity during automatic syringe dispensing. The first detector prototype was created in collaboration between Tema sinergie firm and Georadis, a company based in the Czech Republic. The prototype utilized PVT (Polyvinyltoluene) plastic connected with a sequence of SiPMs (Silicon Photomultipliers) as the detecting element.

To assess the reliability, stability, and linearity of the detector, a series of tests were conducted. The results demonstrated that the system exhibited stable and linear behavior when integrated into an automatic PET radiopharmaceuticals dispensing system. This indicates that the detector can be trusted for use in automatic dose dispensers, potentially improving the accuracy and speed of the machine.

Furthermore, calibration factors for several radioisotopes were investigated, specifically CPS/Bq/cm^3. It is worth noting that the actual CPS (Counts Per Second) detected by the PVT detector may vary depending on factors such as the activity of the sample, the geometry of the detector, and the efficiency of the detector. Proper calibration of the detector can help mitigate these variations and may even eliminate the need for an ionization chamber, thereby reducing the size and weight of the dispenser.

In conclusion, the results of this chapter highlight the reliability of the developed PVT detector for continuous measurement of radiopharmaceutical activity during automatic syringe dispensing. The findings suggest that integrating this type of detector into automatic dose dispensers has the potential to improve the accuracy and speed of the dispensing process. Further research and calibration efforts can optimize the performance of the detector and potentially eliminate the need for additional equipment, leading to more compact and efficient radiopharmaceutical dispensers.

Conclusion

This PhD thesis was performed in a concept of an industrial project within a collaboration of universities and industries. Tema Sinergie company in Faenza, Italy was the industrial party and Hochschule Mannheim university of Applied Science in Mannheim, Germany, where I spent six months of my PhD as a visiting student.

In the first section of this dissertation, a stable multi-channel analyzer (MCA) coupled with NaI(Tl) was characterized and calibrated for radioactive waste management systems. Various techniques for calibrating detector efficiency like Monte Carlo simulation in line with novel experimental techniques have been developed for geometries for which the use of a radioactive standard was either impractical or resulted in substantial experimental uncertainty. A part of this work has been published in Nuclear Science and Engineering (NSE) journal[3]. In addition, in the second part of this thesis, a plastic detector coupled with a series of SiPMs has been developed for use in an automatic radiopharmaceutical dose dispenser. This dispenser is utilized for the preparation of radiopharmaceutical doses in syringes for patients who will be undergoing PET imaging. Automatic radioactive dose dispensers are devices used in nuclear medicine to measure and dispense precise amounts of radioactive material for medical imaging and therapy purposes. They are used to ensure that patients receive the correct amount of radiation for their particular diagnostic or therapeutic procedure. The dispenser works by taking a radioactive source and placing it inside a shielding container. The source is then moved into position above a dose chamber where the dose is measured. The dispenser uses a computer-controlled system to determine the exact amount of radiation needed for the specific patient and procedure, and

then releases that amount into a syringe or vial for use in the medical procedure. One of the advantages of automatic radioactive dose dispensers is that they help reducing the risk of radiation exposure to healthcare workers and patients by providing precise, pre-calibrated doses of radiation. Additionally, they help ensuring that the radioactive material is used efficiently, reducing waste and cost. There are different types of automatic radioactive dose dispensers available in the market, including manual and fully automated systems. Some models also come equipped with features such as barcode scanning, automatic syringe filling, and dose verification to ensure accuracy and safety. Automatic radioactive dose dispensers use a variety of radiation detectors to measure the activity of the radioactive source and ensure that the correct dose is dispensed. The type of detector used depends on the nature of the radiation emitted by the source, the range of activities to be measured, and the specific requirements of the dispensing application. Most of automatic radioactive dose dispensers use ionization chambers for the purpose of activity measurements which are gas-filled chambers that measure the ionizing radiation produced by the radioactive source. They are typically used for high-precision activity measurements and have a wide dynamic range. In the same time ionization chambers are big and static. The development of a plastic scintillator coupled with a series of SiPMs can be a good alternative for ionization chambers in the automatic radiopharmaceutical dose dispensers. In this case we can evaluate the activity of radiopharmaceuticals not only in the end of dispensing but also during it: this makes the dispenser work faster with more accurate performance. In this study a series of tests were performed to investigate the stability, reliability and linearity of the developed detector. According to the results, the PVT detector is a good candidate to be used in a new configuration of Karl100 which is called Karl200.

Bibliography

[1] Howard G. Gemmel Peter F. Sharp and Alison D. Murray (Eds), Practical Nuclear Medicine, 2005.

[2] S Vichi, A Infantino, F Zagni, G Cicoria, S Braccini, D Mostacci, and M Marengo, Radiation Physics and Chemistry **174**, 108966 (2020).

[3] Mahsa Farasat, Federico Zagni, Lorenzo Pompignoli, G. A. Pablo Cirrone, Ulrich W. Scherer, Lidia Strigari, and Domiziano Mostacci, Nuclear Science and Engineering 1 (2023).

[4] Azuwuike Owunwanne, Mohan Patel, and Samy Sadek, *The Handbook of Radiopharmaceuticals* (Springer US, ADDRESS, 1994).

[5] in *Nuclear and Radiochemistry: Fundamentals and Applications* (John Wiley & Sons, Ltd, ADDRESS, 1997), Chap. 1, pp. 1–4.

[6] Michael E. Phelps Simon R. Cherry, James A. Sorenson, *PHYSICS in NUCLEAR MEDICINE* (PUBLISHER, ADDRESS, YEAR).

[7] M. Spiro J.-L. Basdevant, J. Rich, Fundamentals in Nuclear Physics, 2005.

[8] Jerrold T. Bushberg, *The essential physics of medical imaging* (Wolters Kluwer Health/Lippincott Williams & Wilkins, ADDRESS, 2012), p. 1030.

[9] Adam, Radioactive Decay Graph : Group Activity: Half-lives, the Basics, `https://maethome.blogspot.com/2021/02/radioactive-decay-graph-group-activity.html`, 2021.

[10] Kenneth S. Krane, *Introductory Nuclear Physics* (John Wiley & Sons Ltd Inc, NewJersey, US, 1987), pp. 160–360.

[11] Glenn F. Knoll, *Radiation Detection and Measurement* (PUBLISHER, ADDRESS, YEAR).

[12] John R Lamarsh, Anthony J Baratta, and Hall Prentice, Introduction to Nuclear Engineering Third Edition Late Professor with the New Yo rk Polytechnic Institute.

[13] *Debertin K., Helmer R. - Gamma - and X-ray spectrometry with semiconductor detector - libgen.lc* (PUBLISHER, ADDRESS, YEAR).

[14] Galen W Ewing and Harry A Ashworth 1974, .

[15] Gerhard Lutz et al., *Semiconductor radiation detectors* (Springer, ADDRESS, 2007).

[16] Gordon Gilmore, *Practical gamma-ray spectroscopy* (John Wiley & Sons, ADDRESS, 2008).

[17] Esther Rani Thuraka, Racha Ganesh, Dudi Bhanu Prakash, P. Sreekanth, P. Rajitha Reddy, and M. Likhita, in *Digital Multi-Channel analyzer for detection and analysis of radiation in nuclear spectroscopy* (Elsevier Ltd, ADDRESS, 2020), Vol. 38, pp. 3160–3167.

[18] G. Dutto and M. K. Craddock, in *Cyclotrons and their Applications* (PUBLISHER, ADDRESS, YEAR), pp. 1–980.

[19] M A Chaudhri, Cyclotrons in nuclear medicine, 1981.

[20] Gopal B Saha, Fundamentals of Nuclear Pharmacy, Sixth Edition, 1958.

[21] Kalevi Kairemo and Homer A. Macapinlac, in *Nuclear Medicine and Molecular Imaging*, edited by Alberto Signore (Elsevier, Oxford, 2022), pp. 408–425.

[22] Timothy R. DeGrado, R. Edward Coleman, Shuyan Wang, Steven W. Baldwin, Matthew D. Orr, Cary N. Robertson, Thomas J. Polascik, and David T. Price, Cancer Research **61**, 110 (2001).

[23] Mohammad Nazififard, Kune Y. Suh, and Simin Mahdizadeh, Radiation Protection Dosimetry **154**, 510 (2013).

[24] Katrine Ahlström Riklund, Radiation Protection Dosimetry **139**, 8 (2010).

[25] Lidia Strigari, Marcello Benassi, Pierino De Felice, Aldo Fazio, Sandro Nocentini, and Alessia Ceccatelli, (2008).

[26] Council Directive 96/29/EURATOM. Official Journal of the European Communities 1996; No L 159. pp. 1–29, (1996). .

[27] Icrp, International Commission on Radiological Protection. ICRP publication 103: recommendations of the ICRP. Radiat. Prot. Dosim. 129(4), 500–507 (2008).

[28] Louis K Wagner and Oscar R Mulhern, Radiation-attenuating Surgical Gloves: Effects of Scatter and Secondary Electron Production' Medical Physics.

[29] Anna Sarnelli, Emilio Mezzenga, Giacomo Feliciani, Alessandro Savini, Domiziano Mostacci, and Matteo Negrini, Radiation Physics and Chemistry **151**, 6 (2018).

[30] Council Directive 2013/59/Euratom of 5 December 2013 laying down basic safety standards for protection against the dangers arising from exposure to ionising radiation, and repealing Directives 89/618/Euratom, 90/641/Euratom, 96/29/Euratom, 97/43/Euratom and 2003/122/Euratom.

[31] Z Papp and I Uray, Nuclear Instruments and Methods in Physics Research Section A: Accelerators, Spectrometers, Detectors and Associated Equipment **480**, 788 (2002).

[32] James H Ely, Edward R Siciliano, and Richard T Kouzes, in *IEEE Symposium Conference Record Nuclear Science 2004.*, IEEE (PUBLISHER, ADDRESS, 2004), Vol. 3, pp. 1584–1587.

[33] Mona M Gouda, Nuclear Technology and Radiation Protection **34**, 353 (2019).

[34] Vuong Thu Bac, Truong Hoang Tuan, Duong Duc Thang, Bui Dac Dung, Cao Duc Viet, Nguyen Van Khanh, Nguyen Thi Thu Ha, Doan Thuy Hau, and Nguyen Hai Ninh, Nuclear Science and Technology **11**, 16 (2021).

[35] Iskender Akkurt, Faez Waheed, Hakan Akyildirim, and Kadir Gunoglu, Indian Journal of Physics **96**, 2941 (2022).

[36] E-STACK M MONITORING SYSTEM ENGLISH.

[37] Mohamed Abd-Elzaher, Mohamed Salem Badawi, Ahmed El-Khatib, and Abouzeid Ahmed Thabet, (2012).

[38] Ahmed M El-Khatib, Mohamed S Badawi, Mona M Gouda, Sherif S Nafee, and Ekram A El-Mallah, (2013).

[39] Gustavo Haquin, Hovav Zafrir, Danielle Ilzycer, and Noam Weisbrod, Journal of Environmental Radioactivity **237**, 106693 (2021).

[40] digiBASE 14-Pin PMT Tube Base with Integrated Bias Supply, Preamplifier, and MCA (with Digital Signal Processing) for NaI Spectroscopy USB Interface.. . All In One.. . Digital Signal Processing GO DIGITAL.. . Power Up With digiBASE!

[41] N Metropolis, Los Alamos Science **15**, 125 (1987).

[42] Nicholas Metropolis and Stanislaw Ulam, Journal of the American statistical association **44**, 335 (1949).

[43] Herbert A Meyer et al., (1956).

[44] Alfredo Ferrari, Paola R Sala, Alberto Fassò, and Johannes Ranft, ORGANISATION EUROPÉENNE POUR LA RECHERCHE NUCLÉAIRE CERN EUROPEAN ORGANIZATION FOR NUCLEAR RESEARCH Fluka: a multi-particle transport code (Program version 2005), 2005.

[45] A. Sarnelli, M. Negrini, V. D'Errico, D. Bianchini, L. Strigari, E. Mezzenga, E. Menghi, F. Marcocci, and M. Benassi, Applied Radiation and Isotopes **105**, 273 (2015).

[46] Evaluated Nuclear Data File (ENDF) Database.

[47] Gianfranco Cicoria, Francesco Cesarini, Angelo Infantino, Sara Vichi, Federico Zagni, and Mario Marengo, Modern Physics Letters A **32**, 1740014 (2017).

[48] Angelo Infantino, Lorenzo Valtieri, Gianfranco Cicoria, Davide Pancaldi, Domiziano Mostacci, and Mario Marengo, Physica Medica **31**, 991 (2015).

[49] V Fischer, L Pagani, L Pickard, A Couture, S Gardiner, C Grant, J He, T Johnson, E Pantic, C Prokop, et al., Physical Review D **99**, 103021 (2019).

[50] N42. American National Standards Institute. Accredited Standards Committee on Radiation Instrumentation, Institute of Electrical, and Electronics Engineers., *American national standard for calibration and use of germanium spectrometers for the measurement of gamma-ray emission rates of radionuclides : ANSI N42.14-1999 (revision of ANSI N42.14-1991)* (Institute of Electrical and Electronics Engineers, ADDRESS, 1999), p. 76.

[51] Weihao Zhai, wanjun Yu, jiadong xi, and Wei He, Journal of Nuclear Medicine **56**, 1169 (2015).

[52] Dean Broga, Medical Physics **35**, 4766 (2008).

[53] Hamed Abbasizadeh, Behnam Samadpoor Rikan, Truong Thi Kim Nga, Kwan-Tae Kim, SungJin Kim, Dong-Soo Lee, and Kang-Yoon Lee, in *2017 International SoC Design Conference (ISOCC)* (PUBLISHER, ADDRESS, 2017), pp. 198–199.

[54] Shoaib Usman and Amol Patil, Nuclear Engineering and Technology **50**, 1006 (2018).

La borsa di dottorato è stata cofinanziata con risorse del
Programma Operativo Nazionale Ricerca e Innovazione 2014-2020 (CCI 2014IT16M2OP005),
Fondo Sociale Europeo, Azione I.1 "Dottorati Innovativi con caratterizzazione Industriale"